T2R2 東京科学大学 リサーチリポジトリ
Science Tokyo Research Repository

論文 / 著書情報
Article / Book Information

題目(和文)	微衛星の形成における困難とガ　リレオ衛星の起源についての新しいシナリオ
Title(English)	Difficulties in Formation of Satellitesimals and a New Scenario for the Origin of the Galilean Satellites
著者(和文)	芝池諭人
Author(English)	Yuhito Shibaike
出典(和文)	学位:博士(理学), 学位授与機関:東京工業大学, 報告番号:甲第11055号, 授与年月日:2019年3月26日, 学位の種別:課程博士, 審査員:井田 茂,綱川 秀夫,関根 康人,奥住 聡,玄田 英典
Citation(English)	Degree:Doctor (Science), Conferring organization: Tokyo Institute of Technology, Report number:甲第11055号, Conferred date:2019/3/26, Degree Type:Course doctor, Examiner:,,,,
学位種別(和文)	博士論文
Type(English)	Doctoral Thesis

Powered by T2R2 (Science Tokyo Research Repository)

Dissertation

Difficulties in Formation of Satellitesimals and a New Scenario for the Origin of the Galilean Satellites

Yuhito Shibaike

Ida Laboratory

Department of Earth and Planetary Sciences,

Tokyo Institute of Technology

February 22, 2019

Acknowledgments

The author would like to thank Prof. Shigeru Ida for his every thoughtful comments, discussions, and teaching in my research life at Tokyo-Tech. Prof. Satoshi Okuzumi always provides me exact direction of our work. I would also like to thank Prof. Chris W. Ormel for so many times discussion to polish up our research. Prof. Yann Alibert generously supported my research in Switzerland. I received a lot of insightful comments about satellite formation from Prof. Takanori Sasaki. I also thank Prof. Hideo Tsunakawa, Prof. Yasuhito Sekine, Prof. Hidenori Genda, and Prof. Shigeru Wakita for the very useful comments on the revision of this thesis. Talks with my friends, Takahiro Ueda and Shoji Mori, are always funny and delightful moments. I feel grateful to all the members of EPS and ELSI. Finally, without my family, Narito, Noriko, and Madoka, this thesis would not have materialized.

This work was supported by JSPS KAKENHI JP16J09590, and was done as a fellow in the"Young Researchers Exchange Programme between Japan and Switzerland" under the "Japanese-Swiss Science and Technology Programme".

Abstract

It is generally accepted that the large satellites around gas planets formed out of the gas disks, the circumplanetary disks (CPDs), which accompanied the planets' formation. Previous works showed that if enough satellitesimals (km-sized bodies) exist in the disk, satellites with the current satellites' mass can form by two-body collisions. A problem with this scenario, however, is the formation of satellitesimals. Unless CPDs features pressure reversals, the progenitor dust grains will not have had the time to conglomerate, because of the strong radial drift. Moreover, gas gap structures formed by the planets must prevent the dust from flowing into CPDs. An alternative idea to get the material of satellites is planetesimal-capture. However, the growing planets and the gas gaps push out the planetesimals from the feeding-zones and the capture rates decrease. Therefore, how to get the material is a big issue in satellite formation research. Another problem is difficulty in reproducing the characteristics of the satellites simultaneously and consistently. In the case of the Galilean (Jovian) satellites, there are a lot of studies about the characteristics but they can only explain a part of them and contradict each other in part.

First, we investigated the possibility that satellitesimals form in-situ in CPDs. We calculated the radial distribution of the surface density and representative size of dust particles. They grow by mutual collisions and drift toward the planet in with a continuous supply of gas and dust from the parent PPD. In order for the particles to form satellitesimals, the growth must take place faster than they fall onto the planet. We found that this radial drift barrier is overcome if the particles can grow larger than the size which their Stokes number (stooping time normalized by the Kepler-time) is greater than unity. This condition is the same with that of planetesimal formation in PPDs. We also found that the satellitesimals can form (i.e. the above condition is achieved) if the ratio of the dust to gas accretion rates into CPDs is larger than unity. The dust-to-gas ratio must be lower than unity in general, our results suggest that the in-situ satellitesimal formation via particle sticking is

viable only under an extreme condition. However, satellitesimals may form episodically or locally in special conditions, for example, the dust vertical diffusion is weak and the gas surface density is low, predicted in some recent hydrodynamical simulations.

We then constructed a new alternative scenario for the origin of the Galilean satellites which can form the satellites even in the material scarcity. In our new scenario, two kinds of small amount of solid material are supplied to the CPD; mm-sized dust particles and km-sized planetesimals. The captured planetesimals accrete the particles drifting toward Jupiter (i.e. pebbles) so effectively that the planetesimals can grow to satellites before the disk disappears thanks to strong gravitational focusing and aerodynamic drag. However, the growth timescale is longer than that of classical formation scenarios, we invoked an inner disk truncation radius to halt their migration. Other parameters were tuned for the model to match physical, dynamical, compositional, and structural constraints of the Galilean satellites. In contrast to the previous scenarios, our new "slow-pebble-accretion" scenario then reproduced most of the important characteristics simultaneously and consistently; (1) the mass of all the Galilean satellites, (2) the orbits of Io, Europa, and Ganymede captured in mutual 2:1 mean motion resonances, (3) the ice mass fractions of all the Galilean satellites, and (4) the unique ice-rock undifferentiated Callisto and the other three differentiated satellites. However, only Callisto's orbit could not be reproduced but it was also captured in resonance with Ganymede's one.

We found that the in-situ satellitesimal formation in CPDs is very difficult. Therefore, we built a new formation scenario especially for the Galilean satellites, using drifting pebbles instead of satellitesimals. However, our simulations are simplified and, in reality, satellitesimals originated from special conditions may contribute to satellite formation. Therefore, we should investigate satellite formation processes including both satellitesimals and pebbles as a next step. Future measurements of the D/H ratio in H_2O ice of the Galilean satellites by JUICE mission may be able to find out which accretion mechanism was actually dominant. We are now also working on 2-D orbital simulations of the satellites to investigate the resonance capture to solve the problem of Callisto's orbit because we have only carried out simple 1-D simulations. The origin of the large Saturnian satellites

should also be investigated. Our discussion about satellitesimal formation can be applied to the Saturnian system. However, more explanations for the long orbital periods of the satellites will be needed for applying the new Galilean satellite formation scenario to the Saturnian system. General satellite formation will be an attractive research area in future. In particular, satellite formation associated with the evolution of the planets' envelope will be important. Finally, observations of exomoons will open the way to statistical general satellite formation studies.

Contents

1 Introduction **1**

1.1 Satellites 1

1.1.1 Satellites in the Solar System 1

1.1.2 Exomoons 5

1.2 Circumplanetary Disks 5

1.3 Classical Satellite Formation Scenarios 6

1.3.1 Minimum Mass Disk Model 8

1.3.2 Gas-starved Disk Model 8

1.4 Purpose of This Work 11

1.4.1 Scarcity of Material 11

1.4.2 Reproduction of the Galilean Satellites 13

1.5 Differences Between Satellite and Planet Formation 16

2 Satellitesimal Formation by Collisional Dust Growth **19**

2.1 Short Introduction 19

2.2 Methods 19

2.2.1 Circumplanetary Disk Model 19

2.2.2 Dust Growth and Radial Drift 21

2.2.3 Parameter Choice 25

2.3 Results 26

2.3.1 Fiducial Calculations 26

2.3.2 Effects of the Dust and Gas Inflow Mass Fluxes 28

2.3.3 Effects of the Strength of Turbulence . . . 31
2.3.4 Conditions for Satellitesimal Formation . . . 31
2.4 Discussions . . . 33
2.4.1 Feasibility of the High Dust-to-Gas Inflow Mass Flux Ratio . . . 33
2.4.2 Effects of the Internal Density . . . 35
2.4.3 Streaming Instability . . . 36
2.4.4 Validity of the Single-size Approach in Circumplanetary Disks . . . 37
2.4.5 Separation of α coefficient: Turbulent Viscosity and Dust Diffusion 38
2.5 Appendix . . . 40
2.5.1 Approximation of the Stokes Number for Low Gas Density Cases . 40

3 The Galilean Satellites Formation by Pebble Accretion 43
3.1 Short Introduction . . . 43
3.2 Methods . . . 43
3.2.1 Summary of Methods . . . 43
3.2.2 Circum-Jovian Disk model . . . 46
3.2.3 Pebble Growth and Radial Drift . . . 50
3.2.4 Pebble Accretion Efficiency . . . 53
3.2.5 Satellite Internal Temperature . . . 55
3.2.6 Satellite Migration . . . 56
3.2.7 Capture into Mean Motion Resonances . . . 57
3.2.8 Parameters and Constants in Chapter 3 . . . 57
3.3 Results . . . 59
3.4 Assessment . . . 61
3.5 Discussions . . . 65
3.5.1 Formation of Undifferentiated Callisto . . . 65
3.5.2 Inner Cavity and Position of Io . . . 66
3.5.3 Effects of the Thermal Condition of the Disk . . . 70
3.5.4 Effects of the Initial Mass of the Seeds . . . 71

3.5.5 Subsequent Evolution of Ganymede's Internal Structure 71
3.6 Appendix 75
3.6.1 Variables in Chapter 3 75

4 Conclusions **77**
4.1 Difficulties in Formation of Satellitesimals 77
4.2 A New Scenario for the Origin of the Galilean Satellites 78
4.3 Satellitesimals or Pebbles? 79
4.4 Suggestions for Exploration Missions 80
4.5 Future Work 82
4.5.1 Orbital Calculations of Satellites 82
4.5.2 Saturnian Satellites Formation 83
4.5.3 Formation of General Satellites and Gas Planets 85

Chapter 1 Introduction

1.1 Satellites

Over 400 years ago, Galileo Galilei discovered four heavenly bodies nearby Jupiter and realized the possibility that planets other than Earth also have satellites. Since then, scientists have found a lot of satellites around Mars, Jupiter, Saturn, Uranus, Neptune, and other smaller bodies. Nowadays, their eyes are watching outside of the solar system to find "exomoons", satellites rotating around exoplanets. Here, we briefly summarize the findings of the satellites.

1.1.1 Satellites in the Solar System

In this thesis, we focus on the satellites around gas planets. Jupiter, Saturn, and Uranus have large prograde satellites. The satellite-to-planet mass ratios are about 10^{-4} for all the three systems. Neptune also has a large satellites, Triton, but it is retrograde. Saturn has some mid-sized icy satellites and all the gas planets have many small satellites. Figure 1.1 roughly shows the size and orbits of the satellites. The basic data of the satellites is shown in Table 1.1.

We mainly focus on the four large Jovian satellites called "Galilean satellites" in this thesis. The properties of the satellites are well known because of the observation by the *Galileo* mission (NASA, 1989-2003). The inner three satellites, Io, Europa, and Ganymede, are captured in mutual 2:1 mean motion resonances. The satellites' ice mass fractions increase with their distance from Jupiter: Io is dry, Europa consist of 8% ice, while Ganymede and Callisto have ice mass fractions of about 50%. These values were estimated from the gravity measurements by the mission (Sohl et al., 2002). Io is the most active body and considered to be completely differentiated to metallic core and rocky mantle by the strong

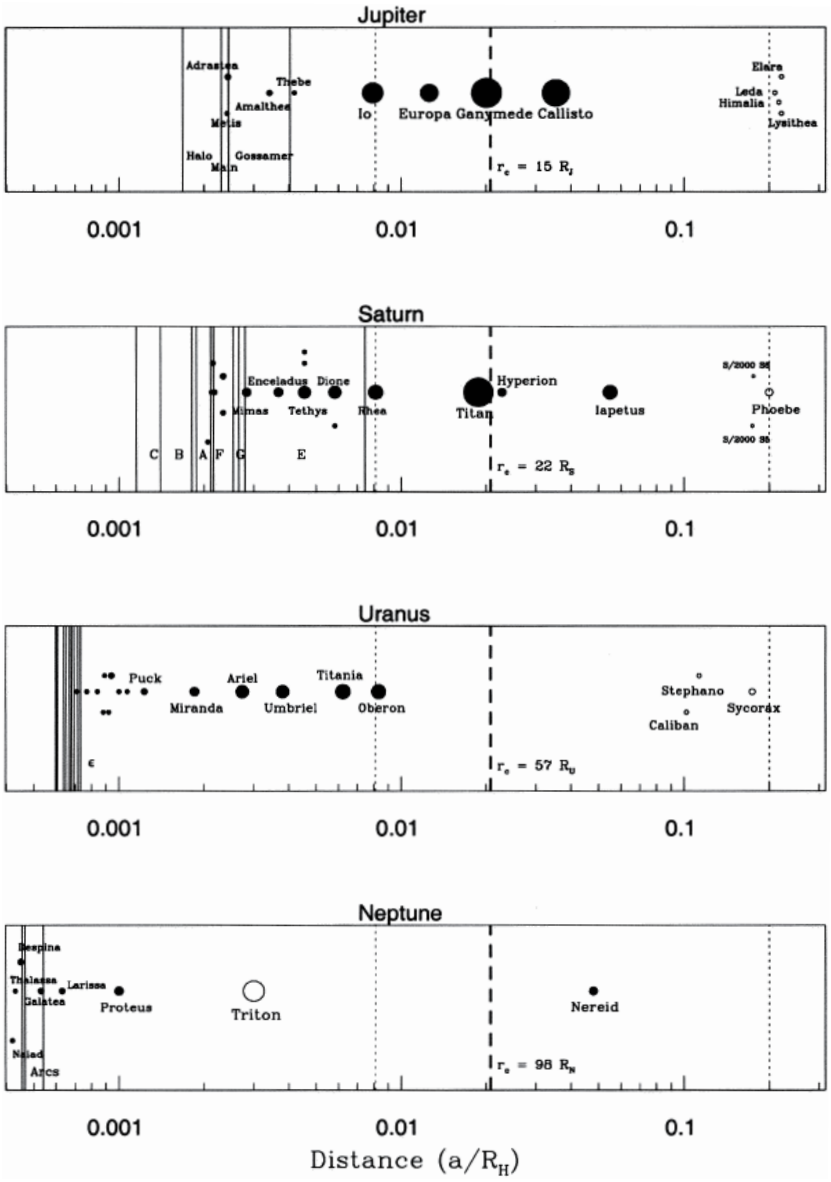

Figure 1.1: **Satellites around the gas planets in the solar system.** The distance scale is in terms of the respective planet's Hill radius ($R_{H,J} \approx 750\,R_J$, $R_{H,S} \approx 1100\,R_S$, $R_{H,U} \approx 2740\,R_U$, and $R_{H,N} \approx 4900\,R_N$). Planetary rings are denoted by solid lines and are labeled when possible. The centrifugal radius is denoted by a bold dashed line. Dotted lines correspond to positions of interest in Mosqueira & Estrada (2003a). This picture is cited from Fig.1 in (Mosqueira & Estrada, 2003a).

Table 1.1: Satellites around the Gas Planets (Mosqueira & Estrada, 2003a)

	Distance [R_P]	Radius [km]	Density [g cm^{-3}]	Mass [10^{26} g]	μ_d [10^{-4}]
Jupiter		71492	1.326	18980	9.5
Io	5.905	1,821	3.53	0.894	0.47
Europa	9.937	1,565	2.97	0.48	0.25
Ganymede	14.99	2,634	1.94	1.4823	0.78
Callisto	26.37	2,403	1.85	1.0776	0.57
Leda*	155.2	5	?	?	?
Himalia*	160.6	85	?	?	?
Lysithea*	163.9	12	?	?	?
Elara*	164.2	40	?	?	?
Saturn		60330	0.687	5684.6	2.9
Mimas	3.075	199	1.12	3.7×10^{-4}	6.5×10^{-4}
Enceladus	3.945	249	1.00	6.5×10^{-4}	1.1×10^{-3}
Tethys	4.884	529	0.98	6.1×10^{-3}	0.01
Dione	6.256	560	1.49	0.011	0.019
Rhea	8.736	764	1.24	0.023	0.04
Titan	20.25	2,575	1.88	1.3457	2.4
Hyperion	24.55	185×113	?	?	?
Iapetus	59.03	720	1.0	0.016	0.028
S/2000 S5*	187.3	10	?	?	?
S/2000 S6*	189	16	?	?	?
Phoebe*	214.5	115×105	?	?	?
Uranus		25559	1.318	868.32	0.44
Puck	3.36	77	?	?	?
Miranda	5.08	240×233	1.2	6.59×10^{-4}	7.6×10^{-3}
Ariel	7.48	581×578	1.67	0.0135	0.16
Umbriel	10.4	585	1.4	0.0117	0.13
Titania	17.05	790	1.71	0.0353	0.41
Oberon	22.8	760	1.63	0.0301	0.35
Caliban*	280.5	30	?	?	?
Stephano*	309	10	?	?	?
Sycorax*	477.9	60	?	?	?
Neptune		24766	1.638	1024.3	0.51
Proteus	4.75	218×201	?	?	?
Triton*	14.32	1,353	2.05	0.215	2.1
Nereid	222.6	170	?	?	?

* Retrograde satellite

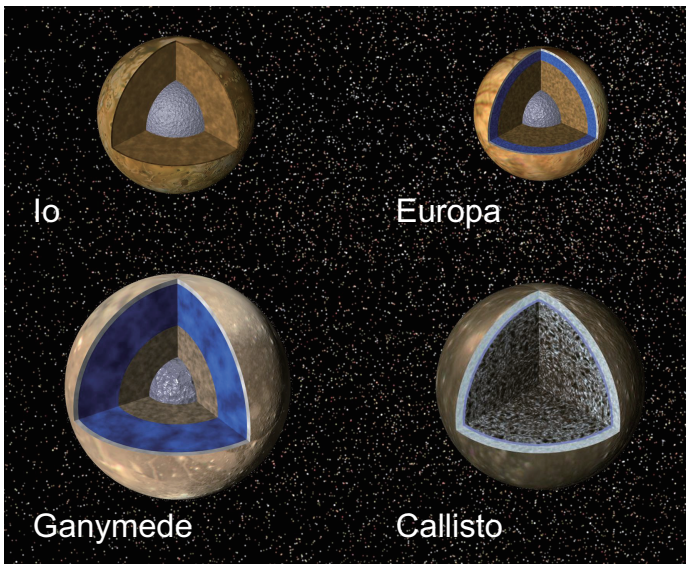

Figure 1.2: **Estimated interiors of the Galilean satellites.** Io has a metallic core and a rocky mantle. Europa has a rocky core and icy mantle. In this picture, it is assumed that a metallic core is also differentiated from the rocky core. A liquid water layer also exists under Europa's icy crust. Ganymede is completely differentiated to a metallic core, rocky core, and Icy mantle. Moreover, this satellite is also estimated to have a liquid water layer under its icy crust. On the other hand, Callisto should be only partially melted. This picture is modified from "JPL release PIA01082 (NASA/JPL, https://photojournal.jpl.nasa.gov/catalog/pia01082)".

tidal heating from Jupiter (Peale et al., 1979). Europa is also considered to be differentiated to rocky core and icy mantle and has liquid ocean under its icy crust because water plumes from the satellite's surface were directly observed by Hubble Space Telescope in 2012 (Roth et al., 2014). However, no evidence of the metal-rock differentiation of the core has discovered. On the other hand, Ganymede has a magnetic field of internal origin suggesting a magnetic dynamo by the convective motion of at least partially molten core (Kivelson et al., 1996). Uniquely, Callisto features an only partially differentiated internal structure in the observations of the interior moment (e.g. Schubert et al., 2004). Figure 1.2 shows the estimated internal structures of the Galilean satellites and Table 1.1 represents the summary of the characteristics of the Galilean system.

Table 1.2: Detailed Properties of the Galilean Satellites (e.g. Schubert et al., 2004)

	Io	Europa	Ganymede	Callisto
Moment-of-interior factor	0.37685	0.346	0.3105	0.3549
Orbital period [days]	1.769	3.551	7.155	16.689
Eccentricity	0.0041	0.0101	0.0006	0.007
Resonance w/ inner one	-	2:1	2:1	no
Ice mass fraction (estimate)	0.00	0.08	0.45	0.56
Differentiation (estimate)	melted (metal/rock)	melted (rock*/ice)	melted (metal/rock/ice)	partially melted

* The state of the core is still unknown.

1.1.2 Exomoons

Recently, observations of exomoons have been tried to succeed. For example, a transit survey of 284 Kepler planetary candidates range from Earth- to Jupiter-sized and from about 0.1 to 1.0 au in separation was carried out but it detected no moons (Teachey et al., 2017). This is consistent with the predictions that moons should be lost during the migration of the planets due to shrinking Hill sphere (Namouni, 2010) or capture into a so-called evection resonance (Spalding et al., 2016). On the other hand, a new observation of a candidate exomoon associated with Kepler-1625b was presented (Teachey & Kipping, 2018). The planet is about three Jupiter mass and the moon is about one Neptune mass. The mass ratio between the planet and moon is 10^{-2}, 100 times larger than Jovian, Saturnian, and Uranian systems. Micro-lensing should be another effective way to observe exomoons but no candidates have been observed (Liebig & Wambsganss, 2010; Hwang et al., 2018).

1.2 Circumplanetary Disks

It is considered that a gas accretion disk forms around a planet in its rapid gas accretion phase as a by-products of the accretion from the parent protoplanetary disk. This disk is called a “circumplanetary disk (CPD)” or e.g. the “circum-Jovian disk (CJD)” for the disk around Jupiter. One of the strong ways to investigate the disk is numerical hydrodynamic simulations. Historically, 2-D isothermal simulations were calculated first (Lubow et al., 1999; D’Angelo et al., 2002), and then 3-D simulations (e.g. Machida et al., 2008). Figure 3.3 shows the schematic gas flow structure around the planet calculated by a 3-D isothermal hydrodynamic simulation in Tanigawa et al. (2012). Accreted gas flows into the planet’s

Hill sphere not from its mid-plane but from high altitude. On the mid-plane, the gas flows outward and goes out from the Hill sphere through the Lagrangian points, L_1 and L_2. Such an outflow structure on the mid-plane has been also shown in the results of the numerical simulations by Machida et al. (2008); Szulágyi et al. (2014); Fung & Chiang (2016); Szulágyi et al. (2016, 2017); Szulágyi (2017). Gressel et al. (2013) has calculated global 3-D magnetohydrodynamic (MHD) simulations of accreting planets embedded in protoplanetary disks (PPDs) and has shown that the flow structure is almost the same with the results of the previous simulations; the inflow is from high altitude and the outflow is on the mid-plane.

The condition for formation of CPDs has not been cleared well. Circumplanetary material has an envelope structure if the central planet mass is small and the envelope becomes a disk when the planet grows heavy. However, Szulágyi et al. (2016) has shown that the envelope structure keeps its form as long as the gas temperature is high. On the other hand, if the envelope becomes cold, a CPD may form even if the planet mass is not large ($\lessapprox 20\ M_\oplus$). A radiative 3-D hydrodynamical simulation has shown that if the surface temperature of the planet is cold (150K), a CPD forms Szulágyi et al. (2018). Wang et al. (2014) also showed that the disk can form in the case of isothermal simulations. On the other hand, (Ayliffe & Bate, 2009) showed that the disk can not form even in the case of isothermal simulations.

1.3 Classical Satellite Formation Scenarios

The formation scenarios for the large satellites around Jupiter and Saturn have been investigated a lot. It has been generally believed that the satellites formed in CPDs during the planets' gas accretion phases (e.g. Canup & Ward, 2006). On the other hand, Crida & Charnoz (2012) argues that the Saturnian mid-sized satellites have formed from ancient massive ring material spreading beyond the Roche radius. The origin of the satellites around Uranus and Neptune is still controversial; in-situ formation in the CPDs, spreading ancient rings' material, giant impacts, and dynamically captures of some bodies after the planets' formation (e.g. Stevenson, 1984; Agnor & Hamilton, 2006; Canup & Ward, 2006;

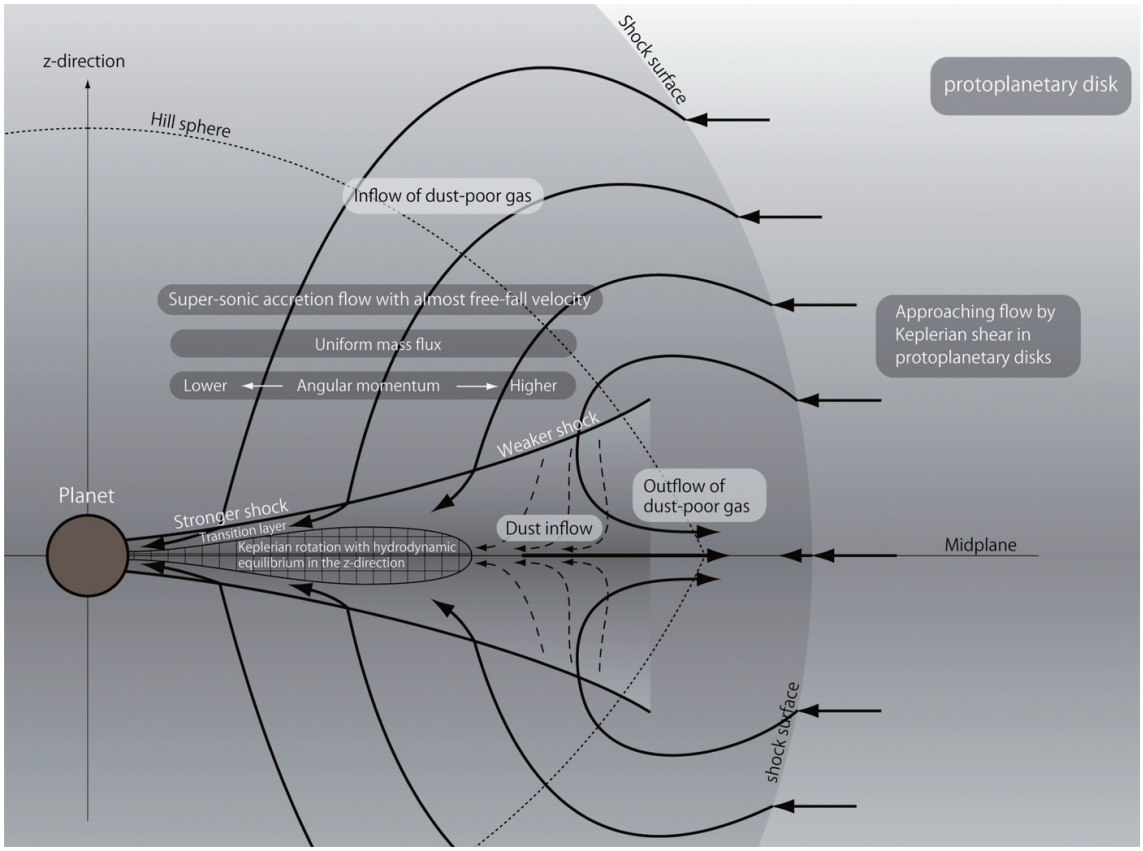

Figure 1.3: **Schematic picture of the flow structure of circumplanetary disks.** This flow structure is based on the results of 3-D numerical simulations in Tanigawa et al. (2012). The black solid curves represent the gas flow direction. The gas penetrating into the shock surface changes their direction to the high altitude because only the tangential velocity component remains.The gas then falls onto the surface of the CPD through its Hill sphere with almost free-fall velocity. However, the angular momentum of the gas is not enough for rotating the falling point, it flows inward on the surface of the CPD. On the other hand, the gas falling onto the outer region of the disk flows out from the disk through the mid-plane. This picture is cited from Figure 1.3 in Tanigawa et al. (2012).

Crida & Charnoz, 2012; Szulágyi et al., 2018). It is considered that the candidate huge exomoon around Kepler-1625b was captured by the planet after its formation phase (Teachey & Kipping, 2018). In this work, we focus on the formation of large satellites around gas planets, in particular, the four large Jovian satellites. Here, we show the two main classical scenarios (models) for satellite formation.

1.3.1 Minimum Mass Disk Model

Lunine & Stevenson (1982) proposed the "minimum mass disk" model where CPDs are static and their solid mass is equal to the total mass of the satellites. The concept of this model is the same with the "minimum mass solar nebular" model in planet formation (Hayashi, 1981). Mosqueira & Estrada (2003a), Mosqueira & Estrada (2003b), Estrada et al. (2009), and Mosqueira et al. (2010) showed that the Jovian and Saturnian satellites can form in the minimum mass disks. One of the key points of this model is that they assume a low-density portion outer than the centrifugal radius. This low-density region is suitable for formation of Callisto with avoiding its internal differentiation by slow satellitesimal accretion. However, such a region has not been reproduced in the previous numerical simulations, and the satellites would have to overcome rapid inward migration induced by the interaction with the massive disk (Miguel & Ida, 2016). Moreover, recent hydrodynamical simulations suggest that the gas accretion onto the planet through the CPD continues even if the gap structure open around the disk (Tanigawa & Ikoma, 2007; Tanigawa & Tanaka, 2016) because the gap is shallower than the traditional prediction (e.g. Kanagawa et al., 2015). In the next subsection, we introduce a formation scenario with the case of continuous gas accretion.

1.3.2 Gas-starved Disk Model

Canup & Ward (2002) and Ward & Canup (2010) proposed the "gas-starved disk" whose mass is regulated by viscous accretion onto the central planet and by gradual supply of the gas from the parent protoplanetary disk. Alibert et al. (2005) also developed a similar accretion disk model consistent with a formation model for Jupiter. Canup & Ward (2006)

performed N-body simulations of satellite formation in the gas-starved disks, showing that the total mass of the satellites formed in the disk is $\sim 10^{-4}$ of the central planet's mass as observed for the Jovian, Saturnian, and Uranian satellite systems. In this scenario, satellites repeated their formation and falls onto the planet by Type I migration over and over, and the total satellite mass becomes quasi-steady. Figure 1.4 represents the total satellite mass in CPDs normalized by the planet mass, calculated in Canup & Ward (2006). It shows that the total mass actually becomes a quasi-steady state with the mass ratio of $\sim 10^{-4}$. The current satellites are then considered as the final generation of the satellites repeating formation and migration. Sasaki et al. (2010) and Ogihara & Ida (2012) also studied this model by using Monte Carlo and N-body simulations respectively, and successfully reproduced the number, masses, and orbits of the Galilean satellites. Sasaki et al. (2010) also reproduced the Saturnian system which one satellite rotates with a long period. In these studies, they assumed the inner cavity of the circum-Jovian disk due to the strong magnetic field of ancient Jupiter. We discussed the validity of this assumption in Sections 3.2.2 and 3.5.2 in detail.

The key parameters of this scenario are (1) the efficiency of transport of gas angular momentum, (2) the gas accretion rate onto the planet through CPDs, and (3) the mass flux of the supply of solid material into CPDs. First, we generally consider the disk as a (quasi-)steady gas accretion disk because the timescale of the growth, drift, migration of solid bodies is much shorter than the evolution timescale of the disk. In this case, the gas surface density of CPDs are determined by the transport efficiencies of angular momentum (i.e. the magnitude of α in the case of α disk model (Shakura & Sunyaev, 1973)) and the mass fluxes of gas inflow from the parental PPDs to the CPDs. However, these key parameters have not been constrained enough. First, hydrodynamical simulations have not succeeded to reproduce the gas accretion of planets in detail, the predicted final mass of Jupiter in one of the simulations is 10 times larger than that of the current Jupiter although the effect of the gap formation is included (Tanigawa & Tanaka, 2016). Second, the mechanism to transport the orbital angular momentum in the gas disk is still controversial. Some previous woks argued that the magneto-rotational instability (MRI, Balbus & Hawley (1991, 1998))

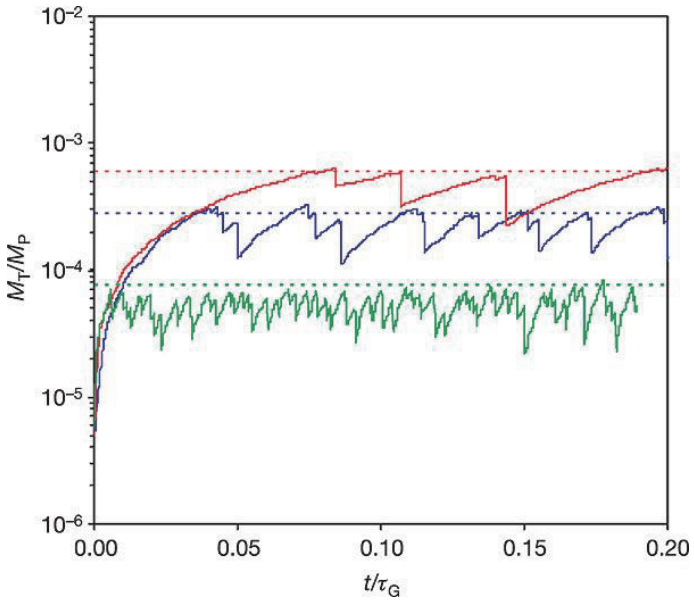

Figure 1.4: **Evolution of the total satellite mass scaled to the planet's mass.** The horizontal and vertical axes are time scaled to $\tau_G = 5$ Myr and the mass ratio between M_T (total satellite mass in the CPDs) and M_p (planet mass), respectively. The red, blue, and green solid curves represent the results of the N-body simulations with $\alpha/f = 5 \times 10^{-4}$, 5×10^{-5}, and 10^{-6}, respectively, where the coefficient α is the strength of viscous turbulence and f is the gas-to-solid inflow mass fluxes ratio. The dashed lines are the estimates from Eqs. (3) in Canup & Ward (2006). The "cracks" in the curves indicate satellites' inward migration and falls into the planet. This figure is cited from Figure 2 in Canup & Ward (2006).

is not maintained in CPDs because of the quick magnetic diffusion due to the small size-scale of CPDs (Fujii et al., 2014; Keith & Wardle, 2014; Turner et al., 2014; Fujii et al., 2017). If $\alpha = 10^{-4}$ (i.e. no MRI) and the gas inflow mass flux is $\dot{M}_{\rm g} = 0.02\ M_{\rm J}\ {\rm Myr}^{-1}$ (the fiducial case of Canup & Ward (2002)), the gas surface density around the Galilean satellites' orbits exceeds 10^3 g cm^{-2} (see Section 2.2.1). As α becomes small, the properties of the disk approach those of the minimum disk model. On the other hand, Zhu et al. (2016) has shown that dissipation of spiral shocks can transport the angular momentum. They carried out 2-D hydrodynamical simulations with radiative cooling in CPDs and the coefficient α could be $\sim 10^{-3}$ in the simulations. However, this simulation is 2-D, and so 3-D calculations are necessary for more correct discussion. Finally, the rate of solid supply to CPDs is an important factor of satellite formation because if there is a large amount of solid material in the disk, the growth timescale of satellites becomes short regardless of formation models (e.g. Mosqueira & Estrada, 2003a; Canup & Ward, 2006). In the next subsection, we explain that the supply of solid material to CPDs should be insufficient to form satellites.

1.4 Purpose of This Work

In this section, we show some problems of previous satellite formation scenarios and explain how we overcome them in this work.

1.4.1 Scarcity of Material

One significant problem of the classical satellite formation scenarios is that the question how satellitesimals form from dust particles is not addressed. Canup & Ward (2006), Sasaki et al. (2010), and Ogihara & Ida (2012) assumed that the dust particles grow to satellitesimals as soon as they deliver from the protoplanetary to circumplanetary disks. However, it is already known from planetesimal formation studies that dust growth to kilometer-sized bodies in PPDs can be hindered by phenomena such as the radial drift and the collisional fragmentation of intermediate-sized particles (Whipple, 1972; Adachi et al., 1976; Weidenschilling, 1977). Therefore, it is easy to imagine that satellitesimal formation in CPDs could

suffer from similar difficulties. In Chapter 2, we investigate this issue in detail and actually show that satellitesimal formation is difficult unless a large amount of dust is supplied into the disk (Shibaike et al., 2017). We find that the one of the conditions for satellitesimal formation is the ratio of dust-to-gas accretion rate into CPDs, $\dot{M}_{\rm d}/\dot{M}_{\rm g}$, is larger than unity. However, this condition must be difficult to achieve because the small dust particles must be trapped at the positive gas pressure gradient at the outer edge of the gap structure (Adachi et al., 1976; Zhu et al., 2012; Kanagawa et al., 2018). Very small particles coupled with gas (smaller than 0.1 mm, by Zhu et al. (2012)) can penetrate into the gap but the amount must be small. As a result, the dust particles supplied from PPDs through the gap structure and the high altitude gas inflow can only grow to pebbles (cm-m size) but then drift toward the planet before they grow to satellitesimals.

It has also been discussed that planetesimals can be captured by gas drag from CPDs (Fujita et al., 2013; Tanigawa et al., 2014; D'Angelo & Podolak, 2015; Suetsugu et al., 2016; Suetsugu & Ohtsuki, 2017). Suetsugu et al. (2016) and Suetsugu & Ohtsuki (2017) examined the captures and subsequent orbital evolutions of planetesimals. They showed that the capture hypothesis could roughly reproduce the initial radial distribution of planetesimals (i.e. satellitesimals) assumed in the satellite formation model by Canup & Ward (2006), Sasaki et al. (2010), and Ogihara & Ida (2012). However, the growing planets and the gap curved by the planets push the planetesimals out from the feeding zones of the planets, rendering the planetesimal capture rates very low (Hayashi et al., 1977; Fujita et al., 2013).

Therefore, in Chapter 3, we construct a new hybrid satellite formation scenario, in particular, for the Galilean satellites (Shibaike et al., submitted). In this scenario, only a small number of planetesimals are captured by CPDs and they grow to satellites by accreting the drifting pebbles. In this case, we can assume a very low dust-to-gas mass accretion ratio because satellitesimals do not have to form. Instead, the growth timescale becomes longer than previous scenarios (~ 10 Myr) and it requires a mechanism to avoid the loss of satellites by their inward migration. Therefore, we invoke an inner cavity of the gas disk around Jupiter opened by a strong magnetic field of the planet to stop the migration at the edge of

the cavity. In Figure 1.5, we summarize the transport of material from the circum-stellar disk (CSD) to CJD, which is implicitly assumed in our scenario.

We note that very recent work argue that these difficulties can be overcome in special situations. Drażkowska & Szulágyi (2018) shows that small dust particles can gather at the point where the effects of the inward drift and outward advection by a gas outflow predicted in their hydrodynamical calculations is balanced. At the gathering point ($\approx 85\ R_{\rm J}$), satellitesimals can form by streaming instability (Youdin & Goodman, 2005) in their calculations. However, the results significantly depend on the gas flow structure. Cilibrasi et al. (2018) carries out population synthesis calculations based on the results of this satellitesimal formation scenario. Ronnet et al. (2018) calculates the orbital evolution of the planetesimals in the CSD and shows that the growth of Saturn excites the eccentricities of their orbits and make them be captured into the CJD even if the gap opens around Jupiter. Suetsugu et al. (2016) also shows that some of the planetesimals with a high and narrow range of the eccentricity in the CSD can be captured into CJD by multiple approaches to Jupiter and become circularized around $\approx 50\ R_{\rm J}$ ("long-lived prograde captured orbit"), outside the current orbits of the Galilean system.

1.4.2 Reproduction of the Galilean Satellites

Any model describing the formation of the Galilean satellites, must obey the observational constraints. However, previous models have only explained parts of these characteristics and the models are inconsistent with each other. Therefore, we aim to create a new scenario which can reproduce most of the important properties simultaneously and consistently. The features of the Galilean satellites to be reproduced and the explanations by the classical scenarios are as follows.

The resonance chain of the inner three satellites' orbits is actually consistent with a scenario where the cavity of the CJD halted the migration of Io and then Europa and Ganymede were captured into the resonances one by one (Sasaki et al., 2010; Ogihara & Ida, 2012). Fujii et al. (2017) argued that opacity transitions change the radial temperature structure

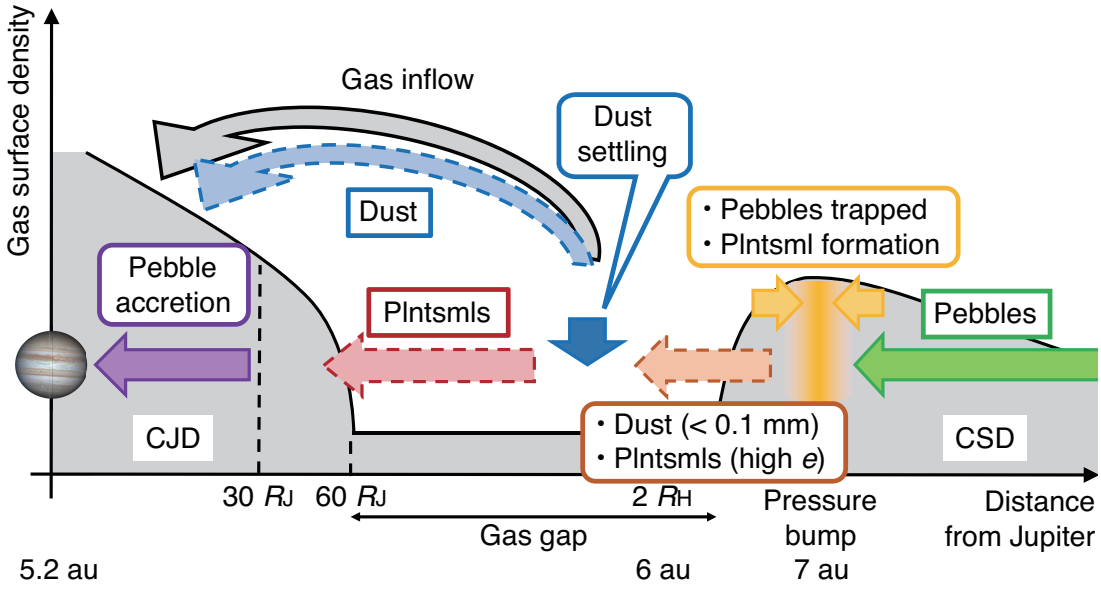

Figure 1.5: **Schematic picture of transport of material.** The horizontal axis roughly shows the distance from Jupiter (or Sun) in the case that Jupiter is at the current position (5.2 R_J). The background black solid curve and the gray shaded region represent the gas surface density. The solid material of satellites originates at the outer region of the CSD as pebbles and they drift inward (green solid arrow) (e.g. Sato et al., 2016). The drifting pebbles are then trapped at the gas pressure bump (pressure maximum) because of the positive gas pressure gradient at the outer edge of the gap (yellow solid region). Because of the high pebble density there, planetesimals (plntsmls) must form from the pebbles and dust particles should be also created from the fragmentation (Kobayashi et al., 2012; Taki et al., 2016). Planetesimals excited by large bodies (such as Saturn) can have high eccentricity and penetrate into the gap (brown dashed arrow) (Kobayashi et al., 2012; Ronnet et al., 2018). The CJD can captures them by the "long-lived prograde captured orbit" around $\approx$ 50 R_J (red dashed arrow) (Suetsugu et al., 2016). Small particles coupled with gas can also penetrate into the gap with gas (brown dashed arrow) but the settling of them makes the inflow gas depleted (blue solid arrow) (Tanigawa et al., 2012; Zhu et al., 2012). The small particles are supplied inside the $\approx$ 30 R_J radius of the CJD with the gas inflow from the high altitude (blue dashed and black solid arrow) (Shibaike et al., 2017). The amounts of the supply of the planetesimals and dust are both small. Finally, the captured planetesimals grow by accreting the drifting pebbles made from the supplied dust which has grown by mutual colliding in the CJD (purple solid arrow).

and it can also stop the migration of the satellites. Classical alternative ways to stop the migration are (1) the largest satellite, Ganymede, migrates fastest and catches up Europa and Io as the gas disk quickly disappears before they fall into the planet (Peale & Lee, 2002), or (2) the differential tidal expansion of the orbits by Jupiter after the gas disappears (e.g. Yoder, 1979). Peale & Lee (2002) has shown that the former way is better to explain the Laplace relation of the three satellites than the latter. In our scenario, we invoke an inner cavity structure like the scenarios in Sasaki et al. (2010); Ogihara & Ida (2012) (see also Section 3.5.2 for detailed discussion).

The outer three satellites have icy material and that constrains the temperature where the satellites formed. One of the historical open questions of satellite formation has been how to reduce the temperature of CPDs. The disk temperature mainly depends on the gas inflow mass flux (see Eq. (2.3) in the next chapter) if the dominant heat source is viscous heating. Hydrodynamical simulations argue that the mass flux is $\dot{M}_{\rm g} \approx 2\ M{\rm J\ Myr}^{-1}$ even if the gap structure is assumed and the disk temperature then becomes about 400 K at the current Ganymede's orbit, higher than the sublimation temperature of H_2O ice, about 160 K. In this case, satellitesimals forming in-situ should be dry because the icy parts of the material must be evaporated. Moreover, if the dust opacity is large, the temperature can be much higher. Therefore, we assume the inflow gas mass flux as 10 to 1000 times smaller than the estimated value in Chapter 2 and 3. An alternative idea is that the satellites formed in the outer cold region of the disk but a poor amount of material would be a severe problem. On the other hand, some recent MHD simulations predict that the mid-plane temperature could be lower than previous estimates thanks to the accretion energy dissipations at the high altitude of the disk (Hirose et al., 2009; Mori et al., in prep.). We discuss these temperature problems and their effects on our simulations also in Sections 2.2.1 and 3.5.3.

The variation in the ice fraction of the satellites also constitutes a formidable modeling challenge. In particular, the ice mass fraction of Europa ($\approx 8\%$)—very small compared to Ganymede and Callisto—is hard to explain by the classical satellitesimal-accretion scenarios because the rocky and icy satellitesimals must be radially mixed beyond the snowline

(Dwyer et al., 2013). The strong tidal heating by Jupiter can remove water components from Io, the closest satellite to the planet, but can not from Europa (Peale et al., 1979). On the other hand, (Ronnet et al., 2017) argues that a scenario where Europa accretes small icy particles, which dehydrated interior to the snowline, can explain the small ice fraction. Another idea is to reproduce the fraction by accreting small particles by invoking the inward movement of the snowline in the final growth phases of the satellites (Canup & Ward, 2009). In Chapter 3, we show that this idea works well in our scenario to reproduce the Europa's small ice mass fraction.

Finally, the dichotomy between the differentiated Ganymede and the undifferentiated Callisto requires tuned conditions. Given that Ganymede and Callisto have similar mass and compositions, it is natural to likewise expect a similar thermal history for these neighboring satellites (Barr & Canup, 2008). In our scenario, we consider a slow growth case, in other words, the case that the accretion heating does not dominate the internal temperature of the satellites. Our "slow-pebble-accretion" scenario explains the dichotomy by the difference of the radiogenic heating of ^{26} Al decay, which is from the different capture time (i.e. starting time of pebble accretion) of the two planetesimals, the seeds of the satellites (see Chapter 3). We also note that subsequent effects, for example, the Late Heavy Bombardment, may be able to make the difference (Barr & Canup, 2010).

1.5 Differences Between Satellite and Planet Formation

Satellites around gas planets are believed to have formed in CPDs, like planets form in PPDs. In this work, we apply the physics and technical methods for planet formation to satellite formation. Before getting into the main part of the thesis, we summarize the main differences between satellite and planet formation for ease of comprehension.

- **Scale** The most important difference is the scale. The semi-major axis of Ganymede is about 10^6 km, more than 100 times smaller than that of Earth (1 au $\approx 1.5\times10^8$ km). The orbital period of the satellite is only 7 days, 50 times shorter, suggesting that the discussion in satellite formation should be based on roughly 10 to 100 times shorter

timescale than planet formation. The typical gas scale height of CPDs is also 10 times larger than that of PPDs (~ 0.1). The compactness of CPDs also makes the magnetic diffusion much faster and it prevents MRI (i.e. the magnetic Reynolds number is small) in CPDs (e.g. Fujii et al., 2014).

- **Open System** Satellite formation regions, in other words, CPDs are open systems unlike planet formation in PPDs. Through the satellite formation, gas and solid material is continuously supplied to CPDs from the parental PPDs and discharged from the disks to the central planets (Figure 1.5). Therefore, the evolution of CPDs and satellites are dominated by the continuous gas and dust inflows and their radial flux es in CPDs. Considering that the timescale of CPDs' evolution must be the same with that of PPDs ($\sim$ 1 Myr), satellite formation must be a quasi-steady state phenomenon that repeats over and over (see Figure 1.4 as an example). This is because the timescale of satellite growth and migration are much shorter than PPDs'. This fact also suggests that (2-D) orbital calculations through the whole satellite formation era or those from the satellite formation to the present are more tough than the orbital calculations of planet formation. On the other hand, if there are special structures like the inner cavity, the system loses the balance between the inflow and outflow and the mass in the system increases (or decreases). In Chapter 2, we discuss the case with a quasi-steady state. On the other hand, in Chapter 3, we assume the inner cavity to stop the loss of satellites, and discuss a non-steady state. Moreover, satellite systems are gravitationally affected by the central star. The Hill spheres are distorted into lemon-like shapes and two (and more) spiral shocks are excited by the stars in CPDs. However, it is generally considered that the large regular satellites formed inside $\sim$ 0.1 Hill radius (see Figure 1.1), the effects from the central stars could be negligible. We actually neglect the effects and only consider azimuthally symmetric cases in this thesis.

- **Absence of Generality** Unfortunately, only one candidate of exomoon has been found and there are few satellite systems in our solar system. Therefore, the discussion of satellite formation is not general yet but limited to unique and historical one like that of planet formation before 1995, the first exoplanet was discovered. There have not actually been a lot of work about general satellite formation but, for example, Heller et al. (2014) has reviewed formation, habitability, and detection of exomoons. In this thesis, we focus on the unique history of the Galilean satellites in Chapter 3. On the other hand, in Chapter 2, we investigate satellitesimal formation which will be able to apply to other than Jovian satellites systems in future. Moreover, we discuss our future work including Saturnian satellites formation and general satellite formation associated with gas planet formation and observation of exomoons in Chapter 4.

Chapter 2 Satellitesimal Formation by Collisional Dust Growth

Except for Section 2.4.5, this chapter is from

Shibaike, Y., Okuzumi, S., Sasaki, T., and Ida, S., *The Astrophysical Journal*, 2017.

2.1 Short Introduction

In this chapter, we aim to answer the question of whether dust particles can grow to satellitesimals by their direct collisional growth in circumplanetary disks. We employ a simple one-dimensional model in which we calculate the radial distribution of the surface density and typical size of dust particles in a steadily accreting circumplanetary disk. We also consider only icy dust particles and do not consider rocky particles. Although we assume perfect sticking upon collision, fragmentation occurs if the collision velocity is higher than a few m s^{-1} when the aggregates are mainly composed of silicate particles (e.g. Blum & Wurm, 2008; Wada et al., 2009). The majority of the Galilean satellites are indeed icy satellites: Europa is $\approx$ 10% and Ganymede and Callisto are $\approx$ 50% ice by mass (Sohl et al., 2002). Our simple treatment allows us to explore a large parameter space. The goal of this chapter is to derive the conditions under which satellitesimal formation via direct coagulation of dust particles is viable.

2.2 Methods

2.2.1 Circumplanetary Disk Model

We model the structure of the circumplanetary disk following Fujii et al. (2014). Although some numerical simulations suggested the possibility that gas near the midplane spiral outward (Tanigawa et al., 2012; Fung & Chiang, 2016; Szulágyi et al., 2016), here we assume that the circumplanetary disk is a viscous accretion disk with a continuous supply

of material from the protoplanetary disk. The diffusion equation for the gas surface density Σ_g of the circumplanetary disk is then given by

$$\frac{\partial \Sigma_g}{\partial t} = \frac{1}{r}\frac{\partial}{\partial r}\left[3r^{1/2}\frac{\partial}{\partial r}\left(r^{1/2}\nu\Sigma_g\right)\right] + f, \tag{2.1}$$

where r is the distance from the central planet, f is the mass flux of the gas inflow from the protoplanetary to circumplanetary disks, and ν is the kinematic viscosity. We employ the standard α prescription (Shakura & Sunyaev, 1973) and express the viscosity as $\nu = \alpha c_s H_g$, where c_s is the isothermal sound speed and H_g is the gas scale height. The sound speed is related to the temperature as $c_s = \sqrt{k_B T/m_g}$ with k_B the Boltzmann constant and $m_g = 3.9 \times 10^{-24}$ g the mean molecular mass. The gas scale height is given by $H_g = c_s/\Omega_K$, where $\Omega_K = \sqrt{GM_{cp}/r^3}$ is the Kepler frequency, and G and M_{cp} are the gravitational constant and the central planet mass, respectively. Unless otherwise noted, we assume M_{cp} to be the Jupiter mass $M_J = 1.89 \times 10^{30}$ g. Based on the results of the three-dimensional hydrodynamical simulation by Tanigawa et al. (2012), Fujii et al. (2014) modeled f as $f \propto r^{-1}$ for $r < r_b$ and $f = 0$ for $r > r_b$, where r_b is the radius of the region where the gas falls in. With this scaling for f, the steady-state solution of Eq. (2.1) can be analytically obtained as (see Eqs. (23) and (25) of Fujii et al., 2014)

$$\Sigma_g = \frac{\dot{M}_g}{2\pi r_b}\frac{r^{3/2}}{\nu}\left(-\frac{2}{9}r^{-1/2} + \frac{2}{3}r_b r^{-3/2}\right), \tag{2.2}$$

where $\dot{M}_g$ is the mass accretion rate of the infall gas. The simulation by Tanigawa et al. (2012) shows that $r_b \approx 20R_J$ for the planet of $M_{cp} = 0.4M_J$ (see also Fujii et al., 2014). Assuming that r_b scales with the Hill radius of the central planet, we use $r_b = 27R_J$ for our $1M_J$-mass planet.

We assume that the circumplanetary disk is viscously heated. Then, the gas temperature at the midplane is given by Nakamoto & Nakagawa (1994),

$$T = \left(\frac{9}{8\sigma_{SB}}\nu\Sigma_g\Omega_K^2\right)^{1/4} g(\tau), \tag{2.3}$$

where σ_{SB} is the Stefan-Boltzmann constant and

$$g(\tau) = \left(\frac{3}{8}\tau + \frac{1}{4.8\tau}\right)^{1/4} \tag{2.4}$$

is a function of the Rosseland mean optical depth τ. In principle, τ depends on the size distribution of the smallest dust particles, which cannot be predicted with simple dust evolution models as employed in this study. Lacking good knowledge about τ, we opt to set $g \approx 1$. Since $g \gtrapprox 1$ in general, the assumption $g \approx 1$ yields a minimum estimate for the disk temperature. The temperature can be up to three times higher than assumed here if the optical depth ranges between $10^{-2} \lesssim \tau \lesssim 10^{2}$. However, this uncertainty has little effects on the main results of this work because the dependence of our results on T is weak (see Section 2.3.2).

According to the simulation by Tanigawa et al. (2012), the mass flux $\dot{M}_{\rm g}$ scales as $\dot{M}_{\rm g} \approx 0.2\Sigma_{\rm PPD} r_{\rm H}^2 \Omega_{\rm PPD}$, where $\Sigma_{\rm PPD}$ and $\Omega_{\rm PPD}$ are the gas surface density and orbital period of the parent protoplanetary disk in the vicinity of the planet, respectively, and $r_{\rm H}$ is the planet' Hill radius (see Figure 14 of Tanigawa et al., 2012). At Jupiter's orbit, the gas surface density is 143 g cm^{-2} according to the minimum-mass solar nebula model of Hayashi (1981). For this value of $\Sigma_{\rm PPD}$, the accretion rate onto Jupiter-sized planet would be $\dot{M}_{\rm g} \approx 200\ M_{\rm J}\ {\rm Myr}^{-1}$.

However, a strong constraint on $\dot{M}_{\rm g}$ can be obtained from the temperature of the circumplanetary disk. In the left panel of Figure 2.1, we plot the midplane temperature of our modeled circumplanetary disk as a function of the distance from the central planets for three cases $\dot{M}_{\rm g} = 2, 0.2, 0, 02$, and 0.002 $M_{\rm J}$ Myr^{-1}. For $\dot{M}_{\rm g} = 2$ and 0.2 $M_{\rm J}$ Myr^{-1}, the temperatures are higher than the sublimation temperature of ice, which is about 160 K. Such hot environments are unsuitable for the formation of icy regular satellites around Jupiter and Saturn. Therefore, we only consider $\dot{M}_{\rm g} \leq 0.02\ M_{\rm J}\ {\rm Myr}^{-1}$ in this work. We plot the gas surface density of the disk for the two cases in the right panel of Figure 2.1.

2.2.2 Dust Growth and Radial Drift

We treat the coagulation and radial drift of dust particles in circumplanetary disks. In particular, we focus on steady state where the radial distribution of the size and surface density of the particles is constant over time. We approximate the size distribution of the particles at each distance from the central planet by a narrow distribution peaked at mass

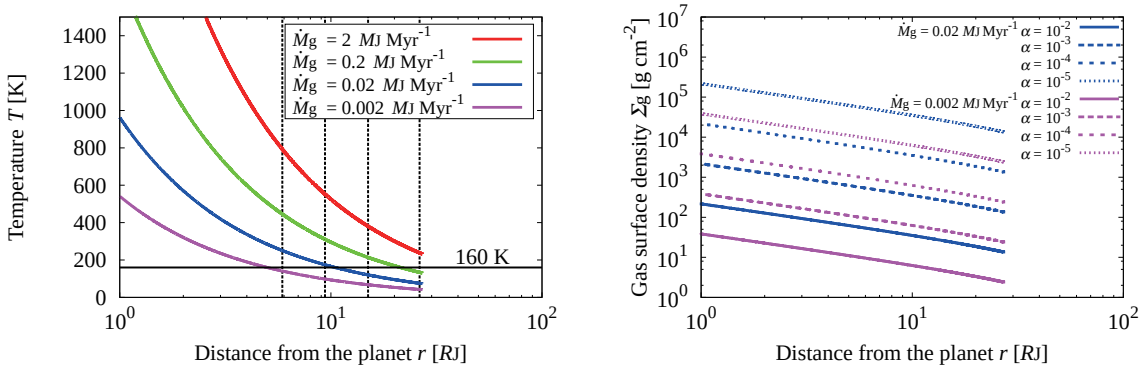

Figure 2.1: **Gas surface density and midplane temperature of CPDs.** The red, blue, green, and purple curves in the left panel represent the temperatures, where $\dot{M}_g = 2, 0.2, 0.02$, and $0.002\ M_J\ \mathrm{Myr}^{-1}$, respectively. The horizontal black line is the sublimation temperature of icy aggregates. The vertical black dashed lines represent the current orbits of the Galilean satellites. The blue and purple curves in the left panel represent the gas surface density, where $\dot{M}_g = 0.02$ and $0.002\ M_J\ \mathrm{Myr}^{-1}$, respectively. The strength of the turbulence is $\alpha = 10^{-5}, 10^{-4}, 10^{-3}$, and 10^{-2}.

m_d. With this approximation, the integro-differential equation governing the evolution of particles in a disk can be rewritten into a simple differential equation for m_d. We also approximate the radial distribution of dust inflow to the circumplanetary disk by a narrow peak lying at $r = r_b$, the outer edge of the infall region. With this approximation, the problem of obtaining the radial distribution of Σ_d and m_d in steady state reduces to a simple boundary-value problem. We discuss the validity of these assumptions in Section 2.4.4.

In addition to the above approximations, we for the moment assume that the collision velocity between the particles is so low that their fragmentation is negligible. The issue of the fragmentation barrier will be separately treated in Section 2.3.3. We also assume that the initial particle radius (i.e., the particle radius at $r = r_b$) is 0.1 mm. This is the maximum size of the particles which can diffuse into the gas gap against the outward drift motion caused by the positive gas pressure gradient at the gap's outer edge (Zhu et al., 2012). We focus on steady state where the radial distribution of the mass and surface density of the particles is independent of time.

In steady state, and in the absence of fragmentation, the mass m_d of the radially drifting

particles is determined as a function of r by (Equation (5) of Sato et al., 2016)

$$v_{\rm r}\frac{dm_{\rm d}}{dr} = \frac{2\sqrt{\pi}R_{\rm d}^2\Delta v_{\rm dd}}{H_{\rm d}}\Sigma_{\rm d}, \tag{2.5}$$

where $R_{\rm d}$, $\Delta v_{\rm dd}$, $v_{\rm r}$, $H_{\rm d}$ and $\Sigma_{\rm d}$ are the radius, collision velocity, drift speed, scale height, and surface mass density of the particles, respectively. The particle mass is related to the particle radius by $m_{\rm d} = (4\pi/3)R_{\rm d}^3\rho_{\rm int}$, where $\rho_{\rm int}$ is the internal density of the particles. We fix $\rho_{\rm int} = 1.4$ g cm^{-3} but we discuss the effects of changing it in Section 2.4.2. The inward accretion rate of the particles is

$$\dot{M}_{\rm d} = -2\pi r v_r \Sigma_{\rm d}, \tag{2.6}$$

which is, in steady state, constant over r and is equal to the infall rate set at $r = r_{\rm d}$ as a boundary condition. We numerically integrate Equation (2.5) with Equation (2.6) from $r = r_{\rm b}$ toward smaller r.

The radial drift velocity of a dust particle is determined by its stopping time, $t_{\rm stop}$. In this study, we express the stopping time in terms of the Stokes number defined by ${\rm St} = \Omega_{\rm K} t_{\rm stop}$ In dense circumplanetary disks, one can safely assume that particles of $R_{\rm d} > 0.1$ mm are much larger than the mean free path of gas molecules so that the flow around the particles can be regarded as continuous fluid. Then, the Stokes number can be expressed as

$${\rm St} = \frac{8}{3C_{\rm D}}\frac{\rho_{\rm int}R_{\rm d}}{\rho_{\rm g}\Delta v_{\rm dg}}\Omega_{\rm K}, \tag{2.7}$$

where $\Delta v_{\rm dg}$ is the relative velocity between the dust particles and the gas, and $C_{\rm D}$ is a dimensionless coefficient that depends on the particle Reynolds number, ${\rm Re_p}$. According to Perets & Murray-Clay (2011), the coefficient can be written as

$$C_{\rm D} = \frac{24}{{\rm Re_p}}(1 + 0.27{\rm Re_p})^{0.43} + 0.47(1 - \exp(-0.04{\rm Re_p}^{0.38})). \tag{2.8}$$

The particle Reynolds number is given by

$${\rm Re_p} = \frac{4R_{\rm d}\Delta v_{\rm dg}}{v_{\rm th}\lambda_{\rm mfp}}, \tag{2.9}$$

where $v_{\rm th} = \sqrt{8/\pi}c_{\rm s}$ is the thermal velocity and $\lambda_{\rm mfp} = m_{\rm g}/(\sigma_{\rm mol}\rho_{\rm g})$ is the mean free pass of the gas with $\sigma_{\rm mol} = 2\times10^{-15}{\rm cm}^2$ the collisional cross section of the gas molecules and $\rho_{\rm g} = \Sigma_{\rm g}/(\sqrt{2\pi}H_{\rm g})$ the gas density at the midplane.

The scale height of the particles can be derived analytically from the balance of their vertical sedimentation and diffusion (Youdin & Lithwick, 2007),

$$H_{\rm d} = H_{\rm g}\left(1 + \frac{\rm St}{\alpha}\frac{1+2{\rm St}}{1+{\rm St}}\right)^{-1/2}. \tag{2.10}$$

The radial drift velocity of the dust particles is (Whipple, 1972; Adachi et al., 1976; Weidenschilling, 1977)

$$v_{\rm r} = -2\frac{\rm St}{{\rm St}^2+1}\eta v_{\rm k}, \tag{2.11}$$

where $v_{\rm k} = r\Omega_{\rm k}$ is the Kepler velocity and

$$\eta = -\frac{1}{2}\left(\frac{H_{\rm g}}{r}\right)^2\frac{\partial \ln \rho_{\rm g} c_{\rm s}^2}{\partial \ln r} \tag{2.12}$$

is the ratio of the pressure gradient force to the gravity of the central planet.

The relative velocity between the dust particles (i.e. collision velocity) is the root sum square

$$\Delta v_{\rm dd} = \sqrt{\Delta v_{\rm B}^2 + \Delta v_{\rm r}^2 + \Delta v_{\phi}^2 + \Delta v_{\rm z}^2 + \Delta v_{\rm t}^2}, \tag{2.13}$$

where $\Delta v_{\rm B}$, $\Delta v_{\rm r}$, Δv_{ϕ}, $\Delta v_{\rm z}$, and $\Delta v_{\rm t}$ are the relative velocities induced by Brownian motion, the radial drift, azimuthal drift, vertical sedimentation, and turbulence (Okuzumi et al., 2012). For collisions between equal-sized particles, the Brownian-motion-induced velocity can be written as $\Delta v_{\rm B} = \sqrt{16 k_{\rm B} T/(\pi m_{\rm d})}$. The relative velocity induced by the radial drift is $\Delta v_{\rm r} = |v_{\rm r}({\rm St}_1) - v_{\rm r}({\rm St}_2)|$, where ${\rm St}_1$ and ${\rm St}_2$ are the Stokes numbers of the two particles. We assume ${\rm St}_2 = 0.5{\rm St}_1$ (see Section 2.4 in Sato et al., 2016) and $v_{\rm r}$ is given by Equation (2.11). The relative velocity induced by the azimuthal drift is $\Delta v_{\phi} = |v_{\phi}({\rm St}_1) - v_{\phi}({\rm St}_2)|$, where $v_{\phi} = -\eta v_{\rm K}/(1+{\rm St}^2)$. The relative velocity induced by the vertical motion is $\Delta v_{\rm z} = |v_{\rm z}({\rm St}_1) - v_{\rm z}({\rm St}_2)|$, where $v_{\rm z} = -\Omega_{\rm K}{\rm St} H_{\rm d}/(1+{\rm St})$. For the relative velocity induced by the turbulence, we use the analytic formula derived from Ormel & Cuzzi (2007). The formula has three limiting expressions:

$$\Delta v_{\rm t} = \begin{cases} \sqrt{\alpha} c_{\rm s} {\rm Re}_{\rm t}^{1/4} |{\rm St}_1 - {\rm St}_2|, & {\rm St}_1 \ll {\rm Re}_{\rm t}^{-1/2}, \\ \sqrt{3\alpha} c_{\rm s} {\rm St}_1^{1/2}, & {\rm Re}_{\rm t}^{-1/2} \ll {\rm St}_1 \ll 1, \\ \sqrt{\alpha} c_{\rm s}\left(\dfrac{1}{1+{\rm St}_1} + \dfrac{1}{1+{\rm St}_2}\right)^{1/2}, & 1 \ll {\rm St}_1. \end{cases} \tag{2.14}$$

Table 2.1: Parameter choice

Quantity	Description	Value
$\dot{M}_{\rm g}$	Gas infall rate	0.02, 0.002 $M_{\rm J}$ Myr^{-1}
$\dot{M}_{\rm d}/\dot{M}_{\rm g}$	Dust-to-gas infall rate ratio	1, 0.1, 0.01, 0.001
α	Turbulence parameter	10^{-5}, 10^{-4}, 10^{-3}, 10^{-2}

Here, $\mathrm{Re_t} = \nu/\nu_{\rm mol}$ is the turbulence Reynolds number, where $\nu_{\rm mol} = v_{\rm th}\lambda_{\rm mfp}/2$ is the molecular viscosity. We obtain the relative velocity between the solid materials and the gas, $\Delta v_{\rm dg}$, by setting $\mathrm{St}_1 = \mathrm{St}$ and $\mathrm{St}_2 \to 0$ in the above expressions for the relative velocities.

2.2.3 Parameter Choice

Table 2.1 summarizes the parameter range explored in this study. The gas infall rate $\dot{M}_{\rm g}$ onto the circumplanetary disk is taken to be either 0.02 $M_{\rm J}$ Myr^{-1} or 0.002 $M_{\rm J}$ Myr^{-1}. As mentioned in Section 2.2.1, we do not consider a higher value of $\dot{M}_{\rm g}$ since the disk would become too hot for icy satellites to form. In reality, a giant planet carves a gap around its orbit. For example, the hydrodynamical simulations by Kanagawa et al. (2015) show that the gas surface density inside the gap is depleted by a factor of more than 100 compared to outside the gap. This means that realistic values of $\dot{M}_{\rm g}$ should be less than 2 $M_{\rm J}$ Myr^{-1}, i.e., less than 1% of the accretion rate without a gap. The infall rate that adopted in the gas-starved disk model of Canup & Ward (2002) is about 0.2 $M_{\rm J}$ Myr^{-1}. The value of $\dot{M}_{\rm g}$ whose temperature is suitable for icy satellite formation is lower than these estimated values. Although we do not consider the decrease of the gas inflow in detail, the final phase of planetary formation should be suitable for satellite formation (see also Section 2.4.1).

The ratio $\dot{M}_{\rm d}/\dot{M}_{\rm g}$ of the dust inflow rate to the gas inflow rate is chosen between 0.001–1. If we assume that the inflow has the solar composition and the dust particles are strongly coupled with the gas, the ratio should be 0.01. However, the gap structure of the gas around Jupiter dams the dust particles drifted from the outer region of the protoplanetary disk toward the Sun and makes their similar gap structure. On the other hand, the strong gas gradient may trigger a hydrodynamic instability and disturb the gas inflow. This disturbance should enhance the radial diffusion of small dust particles and make them nearer to

the central planet (Zhu et al., 2012; Tanigawa et al., 2014).

The strength α of turbulence is varied from 10^{-5} to 10^{-2}. We note that mechanisms that could drive turbulence in the circumplanetary disk is highly uncertain. The magneto-rotational instability, a viable mechanism driving turbulence in ionized accretion disks, could operate on the surface of circumplanetary disks (Turner et al., 2014), but might not produce fully developed turbulence (Fujii et al., 2014). Therefore, we cannot rule out that α of circumplanetary disks falls below α. However, as we discuss in the following section, too weak turbulence would make it difficult for satellitesimals to form within a realistic range of $\dot{M}_{\rm d}/\dot{M}_{\rm g}$.

2.3 Results

In this section, we present the results of our dust growth calculations and explore the conditions under which satellitesimals can form through dust coagulation in circumplanetary disks.

2.3.1 Fiducial Calculations

Figure 2.2 shows the results of our fiducial calculations that assume $\dot{M}_{\rm g} = 0.02\ M_{\rm J}\ {\rm Myr}^{-1}$ and $\alpha = 10^{-4}$. We assume that the snow line is where the midplane temperature is 160 K and it is at $r = 10R_{\rm J}$ (see Figure (2.1)). The top, middle, and bottom panels represent the surface density, radius, and Stokes number of the mass-dominating dust particles in the disk as a function of the distance r from the central planet. Because the particles grow and move inward at the same time, the particle size increases with decreasing r. As already mentioned in the previous section, we assume that the dust particles are 0.1 mm in size when they are initially delivered from the protoplanetary disk to $r = r_{\rm b}(= 27R_{\rm J})$. However, the middle panel of 2.2 suggests that the assumption about the initial size of the dust particles is not crucial because the particles immediately grow at $r \approx r_{\rm b}$. The change of $r_{\rm b}$ will not affect the steady-state profiles either because the profiles should gradually approach the approximated lines (see the dashed lines in the bottom panel of Figure 2.2 and Equation (2.15)).

As the particles grow, their Stokes number St and inward drift velocity $|v_{\rm r}|$ increases in

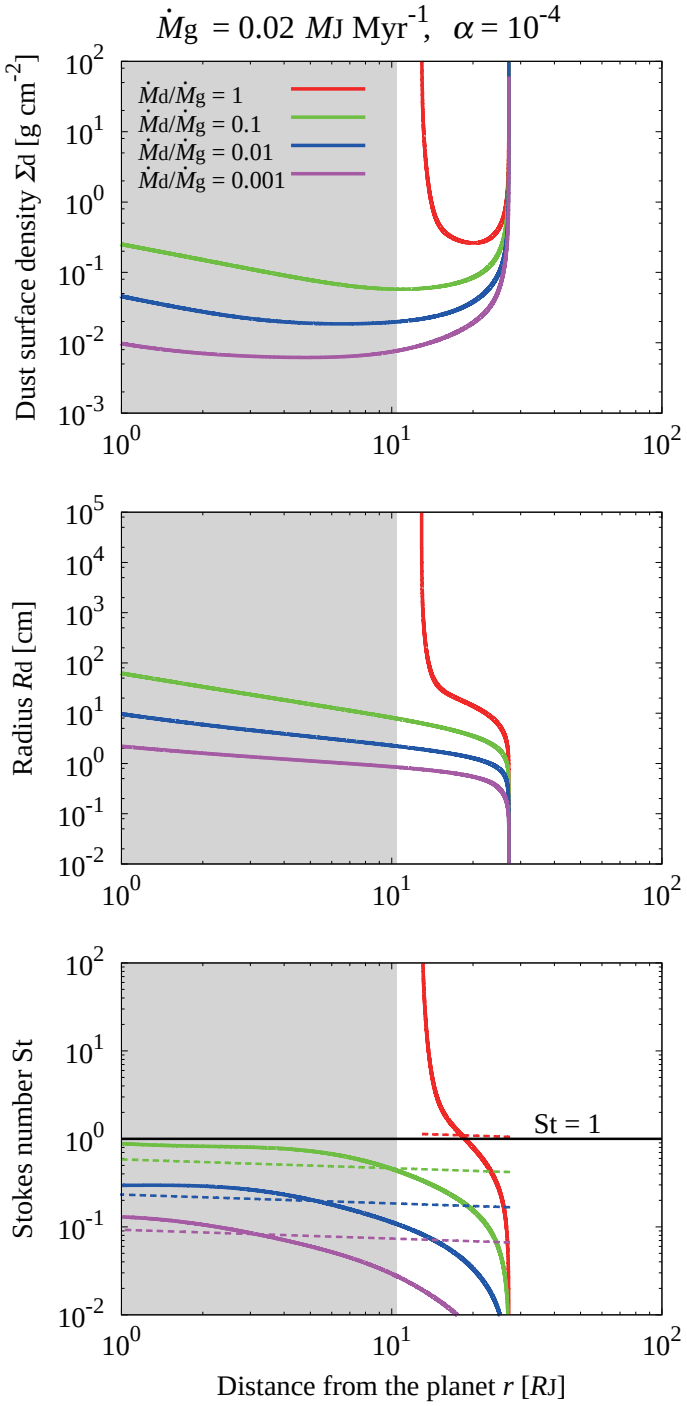

Figure 2.2: **Steady-state profiles of dust in the fiducial case.** The surface density $\Sigma_{\rm d}$ (top panel) and radius $R_{\rm d}$ (middle panel) of dust that grow and drift in the circumplanetary disk of $\dot{M}_{\rm g} = 0.02\ M_{\rm J}\ {\rm Myr}^{-1}$ and $\alpha = 10^{-4}$. The bottom panel shows the Stokes number St of the particles. The red, green, blue, and purple curves correspond to $\dot{M}_{\rm d}/\dot{M}_{\rm g} = 1, 0.1, 0.01,$ and 0.001, respectively. The dashed lines in the bottom panel show the prediction from the analytic estimate given by Equation (2.15). Shaded in gray is the region interior to the snow line, which lies at $r = 10R_{\rm J}$.

accordance with Equations (2.7) and (2.11). We find that the radial drift becomes appreciable when their drift timescale $t_{\rm drift} = r/|v_{\rm r}|$ becomes shorter than 30 times the growth timescale $t_{\rm grow} = m_{\rm d}/({\rm d}m_{\rm d}/{\rm d}t)$, in agreement with the situation for dust evolution in protoplanetary disks (Okuzumi et al., 2012; Tsukamoto et al., 2017). For $\dot{M}_{\rm d}/\dot{M}_{\rm g} = 1$, we find that the particles stop drifting and grow to kilometer-sized satellitesimals at $r \approx 10\,R_{\rm J}$. The drift stalls because the drift speed (normalized by $\eta v_{\rm K}$) decreases with increasing size as long as ${\rm St} > 1$. Therefore, they have to overcome this barrier of the ${\rm St} = 1$ for growing to the satellitesimals. After they achieve ${\rm St} = 1$, the drift speed becomes slower and they get jammed. The jam makes the collisional rate higher, so that the collisional growth speeds up. We also found that this condition ${\rm St} > 1$ is consistent with $t_{\rm grow} < t_{\rm drift}$ when ${\rm St} \sim 1$. Note that we did not consider the possibility that the dust surface density near the snow-line increases because of sublimation or recondensation (e.g. Saito & Sirono, 2011; Ros & Johansen, 2013; Ida et al., 2016; Ida & Guillot, 2016; Schoonenberg & Ormel, 2017).

2.3.2 Effects of the Dust and Gas Inflow Mass Fluxes

The amount of the gas and dust that flow to the circumplanetary disk can be changed by the conditions of the central planet, the protoplanetary disk, and the circumplanetary disk. We investigate the effects of changing the gas and dust inflow mass fluxes. Figure 2.2 shows that the the dust surface density increases with the dust-to-gas inflow mass flux ratio $\dot{M}_{\rm d}/\dot{M}_{\rm g}$. The radius and Stokes number of the dust particles also have the same features. The particles can grow to satellitesimals only when $\dot{M}_{\rm d}/\dot{M}_{\rm g} = 1$. This can be understood by using the approximate analytical expression for the Stokes number (dotted lines in the figure). When $\alpha = 10^{-4}$ and $\dot{M}_{\rm g} = 0.02\ M_{\rm J}\ {\rm Myr}^{-1}$, the gas surface density is so large that ${\rm Re}_{\rm p} \ll 1$. For example, we found that the particle Reynolds number ${\rm Re}_{\rm p}$ is about 10^3 when $\dot{M}_{\rm d}/\dot{M}_{\rm g} = 0.1 - 1$ at $r \sim 10\,R_{\rm J}$. In this case, the dimensionless coefficient $C_{\rm D}$ can be approximated as a constant, $C_{\rm D} \approx 0.5$ (Newton's friction law, see Equation (2.8)). The dust–dust and dust–gas relative velocities can also be approximated as $\Delta v_{\rm dd} \approx (1/2)v_{\rm r}$ and $\Delta v_{\rm dg} \approx v_{\rm r}$ because the turbulence is so week that $\Delta v_{\rm t}$ is much smaller than $\Delta v_{\rm r}$ (see Figure

2.5). The approximated Stokes number can then be described as,

$$\mathrm{St} \approx 1.2 \left(\frac{\dot{M}_\mathrm{d}/\dot{M}_\mathrm{g}}{1} \right)^{2/5} \left(\frac{\alpha}{10^{-4}} \right)^{1/5} \left(\frac{T}{160\ \mathrm{K}} \right)^{-2/5} \left(\frac{M_\mathrm{cp}}{1\ M_\mathrm{J}} \right)^{2/5} \left(\frac{r}{10\ R_\mathrm{J}} \right)^{-2/5}, \tag{2.15}$$

for small r. Equation (2.15) is derived by substituting Equation (2.6) into Equation (2.5) and integrating it. Here, the gas surface density and the midplane temperature have been approximated as $\Sigma_\mathrm{g} \approx \dot{M}_\mathrm{g}\Omega_\mathrm{K}/(3\pi\alpha c_\mathrm{s}^2)$ and $T \approx (3GM_\mathrm{cp}\dot{M}_\mathrm{g}/(8\pi\sigma_\mathrm{SB}r^3))^{1/4}$. The scale height and radial drift velocity of the dust particles have also been approximated as $H_\mathrm{d} \approx H_\mathrm{g}(\alpha/\mathrm{St})^{1/2}$ and $v_\mathrm{r} \approx -2\mathrm{St}\eta v_\mathrm{K}$. Equation (2.15) shows that the Stokes number is proportional to $(\dot{M}_\mathrm{d}/\dot{M}_\mathrm{g})^{2/5}$ and reaches unity when $\dot{M}_\mathrm{d}/\dot{M}_\mathrm{g} = 1$ and $r = 10\ R_\mathrm{J}$. Once St exceeds unity, the radial drift velocity starts to decrease with increasing particle size, and hence the particles grow to satellitesimals. Neglecting the weak $\dot{M}_\mathrm{g}$ dependence of T ($T \propto \dot{M}_\mathrm{g}^{1/4}$), Σ_g is proportional to $\dot{M}_\mathrm{g}$. When Σ_g is high, the gas drag force that the dust particles receive is strong and St is small. The collision rate of the dust particles becomes high when $\dot{M}_\mathrm{d}$ (i.e. Σ_d) is large. The high collision rate promotes satellitesimal formation. Even if the Newton's friction law does not apply, the Stokes number is proportional to $(\dot{M}_\mathrm{d}/\dot{M}_\mathrm{g})^{2/3}$ or $(\dot{M}_\mathrm{d}/\dot{M}_\mathrm{g})^{6/11}$ and the trend that the Stokes number is an increasing function does not change (see Equations (2.17) and (2.18) in Section 2.5.1).

The key parameter of the dust evolution is not the pure gas inflow mass flux but the ratio of the dust and gas inflow mass fluxes. Figure 2.3 represents the distributions of the dust surface density, the dust radius, and the Stokes number of the representative dust particles for $\dot{M}_\mathrm{g} = 0.002\ M_\mathrm{J}\ \mathrm{Myr}^{-1}$ and $\alpha = 10^{-4}$. In this case, the snow line lies at $r = 5R_\mathrm{J}$ (see Figure (2.1)). The profiles of the surface density and radius of dust particles are lower than those for $\dot{M}_\mathrm{g} = 0.02\ M_\mathrm{J}\ \mathrm{Myr}^{-1}$ and $\alpha = 10^{-4}$ (Figure 2.2). The radial profiles of St are steeper than those in the fiducial case (we derive Equation (2.17), an analytic equation of St for $\dot{M}_\mathrm{g} = 0.002\ M_\mathrm{J}\ \mathrm{Myr}^{-1}$, in Section 2.5.1). Nevertheless, we find that dust particles grow beyond St = 1 only when $\dot{M}_\mathrm{d}/\dot{M}_\mathrm{g} = 1$. For fixed $\dot{M}_\mathrm{d}/\dot{M}_\mathrm{g}$, $\dot{M}_\mathrm{g}$ dependence of St is indeed weak. When $\dot{M}_\mathrm{g} = 0.02\ M_\mathrm{J}\ \mathrm{Myr}^{-1}$, only T depends on $\dot{M}_\mathrm{g}$ ($T \propto \dot{M}_\mathrm{g}^{1/4}$) so that $\mathrm{St} \propto T^{-2/5} \propto \dot{M}_\mathrm{g}^{-1/10}$ (Equation (2.15)). When $\dot{M}_\mathrm{g} = 0.002\ M_\mathrm{J}\ \mathrm{Myr}^{-1}$ or $\alpha = 10^{-2}$, $\mathrm{St} \propto T^{-1} \times \dot{M}_\mathrm{g}^{4/9} \propto \dot{M}_\mathrm{g}^{7/36}$ or $\mathrm{St} \propto T^{-1} \times \dot{M}_\mathrm{g}^{4/11} \propto \dot{M}_\mathrm{g}^{5/44}$ (Equations (2.17) and (2.18)).

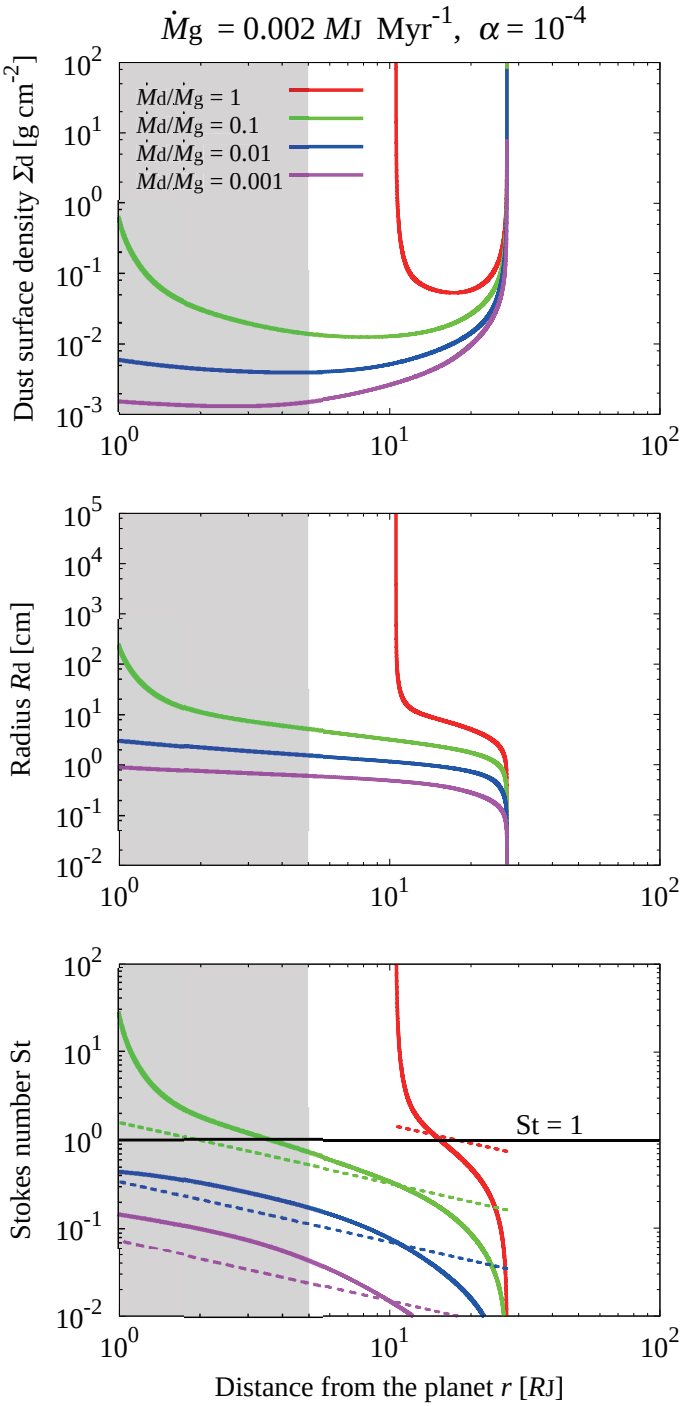

Figure 2.3: **Steady-state profiles of dust with a lower gas inflow flux.** Same as Figure 2.2, but for $\dot{M}_{\rm g} = 0.002\ M_{\rm J}\ {\rm Myr}^{-1}$ and $\alpha = 10^{-4}$. The dashed lines in the bottom panel show the prediction from the analytic estimate given by Equation (2.17). Shaded in gray is the region interior to the snow line, which lies at $r = 5R_{\rm J}$.

2.3.3 Effects of the Strength of Turbulence

The strength of turbulence in the circumplanetary disk is also a key parameter of the dust evolution. Figure 2.4 represents the profiles of the dust particles in the case with $\dot{M}_{\rm g} = 0.02\ M_{\rm J}\ {\rm Myr}^{-1}$, and $\alpha = 10^{-5}$ (upper panel) and $\alpha = 10^{-2}$ (lower panel). In the case of $\alpha = 10^{-5}$, the Stokes number of drifting particles is on average lower than those in the fiducial case with $\alpha = 10^{-4}$. Even if $\dot{M}_{\rm d}/\dot{M}_{\rm g} = 1$, the dust particles cannot grow to satellitesimals outside of the snow line at $r = 10\ R_{\rm J}$. In the case of $\alpha = 10^{-2}$, the Stokes number is slightly higher than in the fiducial case. Equations (2.15) and (2.18) show that the Stokes number is actually proportional to $\alpha^{1/5}$ or $\alpha^{1/11}$ when $\dot{M}_{\rm g} = 0.02\ M_{\rm J}\ {\rm Myr}^{-1}$ (see also Equation (2.17) for $\dot{M}_{\rm g} = 0.002\ M_{\rm J}\ {\rm Myr}^{-1}$). However, the stokes number is not high enough for the particles to overcome the radial drift outside the snow line unless $\dot{M}_{\rm d}/\dot{M}_{\rm g} \geq 1$.

Even if $\dot{M}_{\rm d}/\dot{M}_{\rm g} = 1$, satellitesimals would not form via direct dust growth because the relative velocity between the dust particles would be too high to avoid collisional fragmentation. Collision simulations by Wada et al. (2009) argued that icy dust aggregates with monomers of 0.1 μm fragment upon collision if the collision velocity is higher than 50 m s^{-1}. Figure 2.5 represents the dust–dust relative velocities for different values of α. When $\alpha = 10^{-4}$, the relative velocity is determined by the radial drift speed and that induced by the turbulence is low. When $\alpha = 10^{-2}$, the dust–dust relative velocity is determined by the turbulence because the relative velocity induced by the turbulence is proportional to $\sqrt{\alpha}$ (Equation(2.14)) and it becomes 10 times higher than that for $\alpha = 10^{-4}$. Figure 2.5 shows that the relative velocity exceeds 50 m s^{-1}, indicating that collisional fragmentation would happen. Therefore, satellitesimal formation via direct dust coagulation is unlikely to occur in such strong turbulence. Note that experiments by Gundlach & Blum (2015) showed that the fragmentation occurs with the collision speed of $\sim$ 10 m s^{-1} for icy aggregates with monomers of 1 μm.

2.3.4 Conditions for Satellitesimal Formation

The results presented in the previous subsections can be summarized in Figure 2.6. This figure represents the condition for satellitesimal formation when $\dot{M}_{\rm g} = 0.02\ M_{\rm J}\ {\rm Myr}^{-1}$.

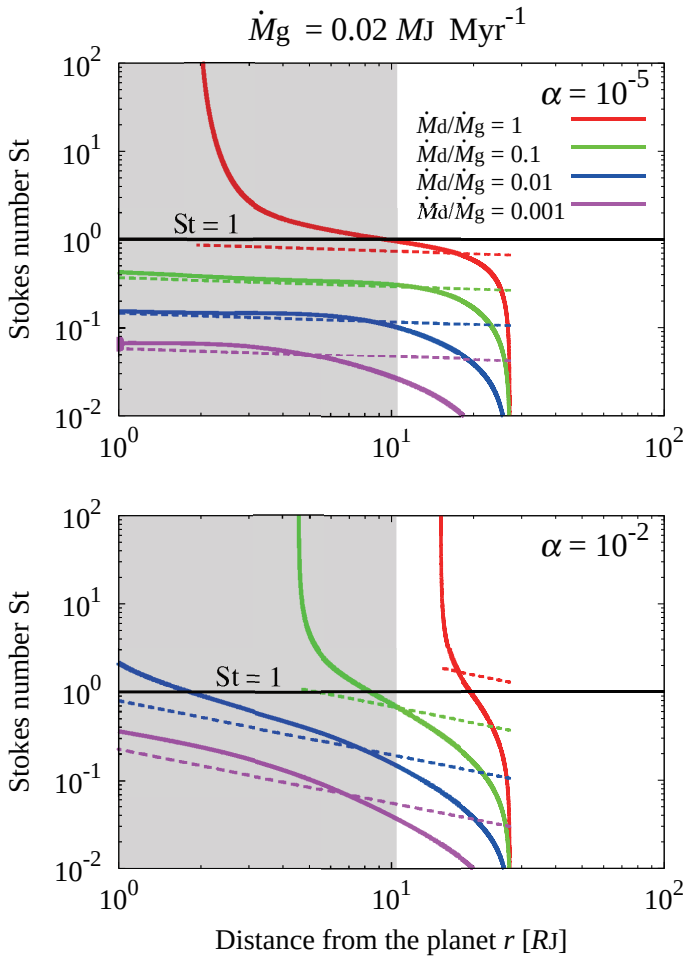

Figure 2.4: **Steady-state profiles of dust with different turbulent strength.** Steady-state profiles of the Stokes number St of the particles when $\dot{M}_{\rm g} = 0.02\ M_{\rm J}\ {\rm Myr}^{-1}$, and $\alpha = 10^{-5}$ (upper panel) and $\alpha = 10^{-2}$ (lower panel). The dashed lines in the lower panel show the prediction from the analytic estimate given by Equation (2.18).

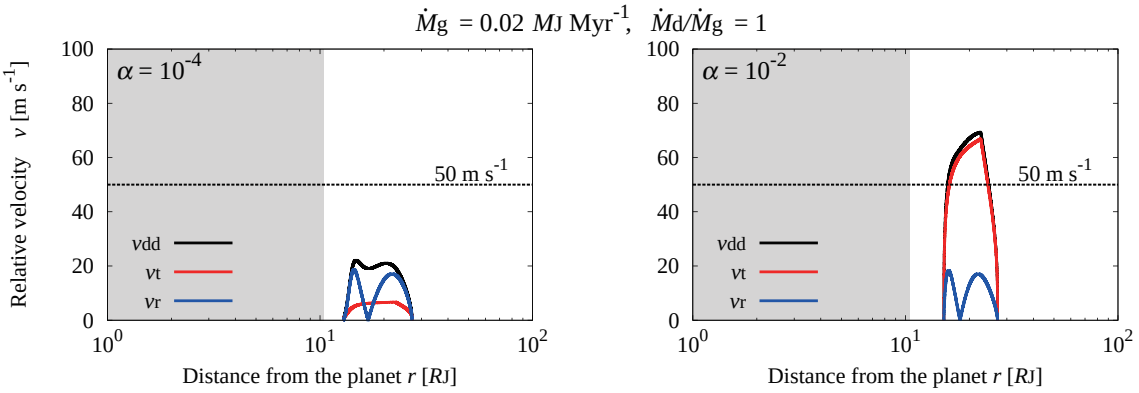

Figure 2.5: **Dust–dust relative velocities with different turbulent strength.** The left and right panels are $\alpha = 10^{-4}$ and $\alpha = 10^{-2}$, respectively. The other conditions are $\dot{M}_\mathrm{d}/\dot{M}_\mathrm{g} = 1$ and $\dot{M}_\mathrm{g} = 0.02\ M_\mathrm{J}\ \mathrm{Myr}^{-1}$ in both the panels. The black curves represent the dust–dust relative velocities (collision velocities). The red and blue curves represent the velocities induced by only the turbulence and their radial drift, respectively. The black dashed lines are the critical velocity of fragmentation.

The conditions are $\dot{M}_\mathrm{d}/\dot{M}_\mathrm{g} \geq 1$ and $10^{-4} \leq \alpha < 10^{-2}$. The condition for breaking through the radial drift barrier is approximately given by $\dot{M}_\mathrm{d}/\dot{M}_\mathrm{g} > 6 \times 10^{-3} \times \alpha^{-1/2}$ derived from the condition $\mathrm{St} > 1$ at $r = 10\ R_\mathrm{J}$ (see Equation (2.15)). When the turbulence is strong ($\alpha \gtrsim 10^{-3}$), it is about $\dot{M}_\mathrm{d}/\dot{M}_\mathrm{g} > 0.08\ \alpha^{-1/6}$ (see Equation (2.18)). The dashed lines in Figure (2.6) show the boundary of each condition. However, in the case of $\alpha = 10^{-2}$, the aggregate collision velocity is too high to avoid collisional fragmentation. When $\dot{M}_\mathrm{g} = 0.002\ M_\mathrm{J}\ \mathrm{Myr}^{-1}$, the drift barrier is overcome outside the snow line even if $\alpha = 10^{-5}$ because the line is at $r = 5\ R_\mathrm{J}$ (asterisk in Figure (2.6)).

2.4 Discussions

2.4.1 Feasibility of the High Dust-to-Gas Inflow Mass Flux Ratio

We found that the one of the conditions for satellitesimal formation is $\dot{M}_\mathrm{d}/\dot{M}_\mathrm{g} \geq 1$. However, this condition may be difficult to achieve. First, the dust particles tend to settle down toward the midplane, the inflow gas from the high altitude is likely to dust-poor gas (Tanigawa et al., 2012). This effect must depend on the conditions of the turbulence and the gas density of the region around the circumplanetary disk which the accretion gas comes

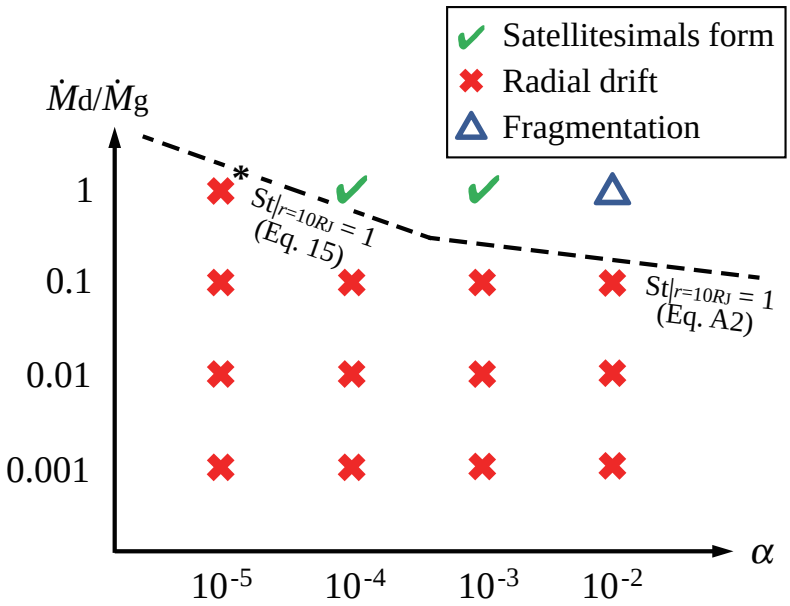

Figure 2.6: **Condition for satellitesimal formation.** The gas accretion rate is $\dot{M}_{\rm g} = 0.02\ M_{\rm J}\ {\rm Myr}^{-1}$. The green ticks indicate that dust particles grow to satellitesimals outside of the snow line at $r = 10\ R_{\rm J}$. The red crosses indicate that the radial drift barrier inhibits dust growth to satellitesimals. The blue triangles indicate that dust particles grow to satellitesimals on the calculations but the collision velocity (dust–dust relative velocity) is faster than the critical velocity of fragmentation, 50 m s^{-1}. The dashed lines show the condition ${\rm St} = 1$ at $r = 10\ R_{\rm J}$ from Equations (2.15) and (2.18). When $\dot{M}_{\rm g} = 0.002\ M_{\rm J}\ {\rm Myr}^{-1}$, the condition is the same except that the drift barrier is overcome outside the snow line if $\dot{M}_{\rm d}/\dot{M}_{\rm g} = 1$ and $\alpha = 10^{-5}$ (asterisk).

from (Equations (2.15) and (2.10)). Second, the dust supply may not be enough to achieve $\dot{M}_{\rm d}/\dot{M}_{\rm g} \geq 1$. Dust particles are drifted from the outer region of the protoplanetary disk. However, these particles have already grown to the pebbles (cm-sized particles) until they reach around the gas planets like Jupiter (e.g. Lambrechts & Johansen, 2012; Okuzumi et al., 2012; Sato et al., 2016), so that most of them should be dammed at the outer edge of the gas gap by the positive gas pressure gradient (e.g. Adachi et al., 1976; Zhu et al., 2012; Kanagawa et al., 2018). In this case, only a small part of the dust particles can penetrate into the gas gap and flow into the circumplanetary disk, so that the dust-to-gas mass inflow flux ratio should be smaller than unity.

One possibility to achieve the high ratio is considering satellitesimal formation in the final phase of planetary formation. Photoevaporation may increase the dust-to-gas mass ratio in protoplanetary disk as time passes (e.g. Alexander et al., 2006a,b). It is also considered that the gas flux decreases in the final phase because the gas gap becomes wider and deeper (e.g. Kanagawa et al., 2015; Tanigawa & Tanaka, 2016). Our results actually suggested that low gas inflow mass flux is suitable for satellitesimal formation. The midplane temperature T is almost proportional to $\dot{M}_{\rm g}^{1/4}$ (Equation (2.3)). When the gas inflow decrease, the disk becomes cooler and the snow line moves inward (see Figure 2.1). This means that the area where icy satellitesimals can form expands. Moreover, the collisional velocity driven by turbulence weakly depends on the gas inflow rate, $\Delta v_{\rm t} \propto c_{\rm s} \propto T^{1/2} \propto \dot{M}_{\rm g}^{1/8}$ (Equation (2.14)). Low gas inflow mass flux may also contribute to overcoming fragmentation barrier.

2.4.2 Effects of the Internal Density

We investigated the impact of changing the internal density of dust particles on satellitesimal formation. Figure 2.7 represents the Stokes number for $\rho_{\rm int} = 1.4 \times 10^{-4}$ g cm^{-3} and $\alpha = 10^{-4}$. We found that the conditions for satellitesimal formation did not change from those with $\rho_{\rm int} = 1.4$ g cm^{-3} (see Figures. 2.2 and 2.4). This is because the Stokes number for small r can also be approximated as Equation (2.15) in this case, (we found that ${\rm Re}_{\rm p} \gtrsim 10^3$ for $r \sim 10\ R_{\rm J}$ and we have been able to assume $C_{\rm D} \approx 0.5$) and this approximated Stokes number dose not depend on $\rho_{\rm int}$. In generally, the growth timescale takes a

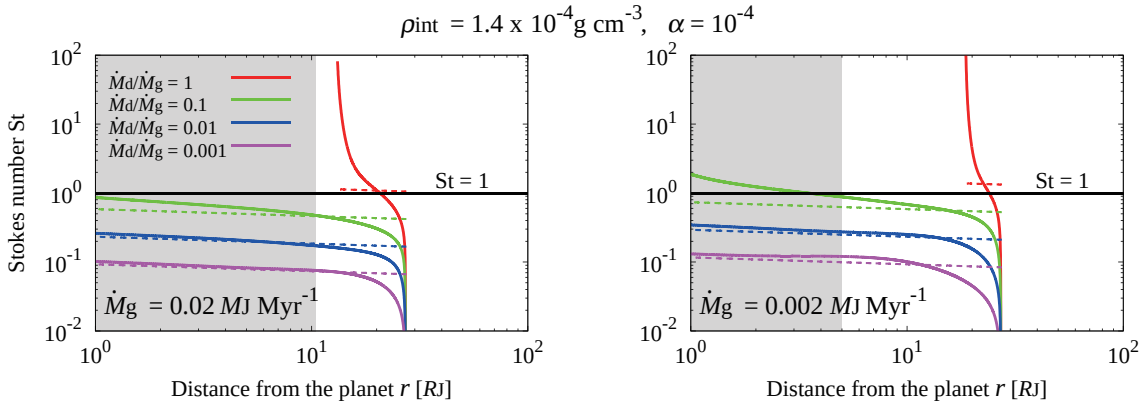

Figure 2.7: **Steady-state profiles of fluffy dust.** The Stokes number St of the highly porous ($\rho_{\rm int} = 1.4 \times 10^{-4}$g cm^{-3}) dust particles with $\alpha = 10^{-4}$, and $\dot{M}_{\rm g} = 0.02$ (left panel) and 0.002 $M_{\rm J}$ Myr^{-1} (right panel). The dashed lines in both the panels show the predictions from the analytic estimates given by Equation (2.15). We stopped the calculation when the particle radius reaches 100 km (the red curve in the left panel).

minimum value within the Newton regime (Okuzumi et al., 2012). Therefore, the Stokes number dose not grow beyond the dashed lines in Figure 2.7 by changing $\rho_{\rm int}$ unless it reaches unity. The impact of changing $\rho_{\rm int}$ is only that the fluffy particles move earlier than the compact particles from the Stokes regime ($\mathrm{Re_p} \lesssim 1$) to the Newton regime.

We note that the growth timescale (i.e. St) depends on the internal density only in the Stokes regime (Okuzumi et al., 2012). Since the gas densities of protoplanetary disks are generally much lower than those of circumplanetary disks, the growth timescale of highly porous dust aggregates in protoplanetary disks can be so small that they overcome the drift barrier within the Stokes regime (Okuzumi et al., 2012).

2.4.3 Streaming Instability

Generating growing particle-density perturbations by streaming instability is another planetesimal formation mechanism not the collisional growth of the dust particles (Youdin & Goodman, 2005). The difference between the velocities of the dust and gas drives the instability. The dust particles are concentrated quickly in localized dense clumps, so that they do not drift to the Sun. This mechanism may also be applicable to satellitesimal formation. Carrera et al. (2015) showed that the condition that streaming instability is active depends

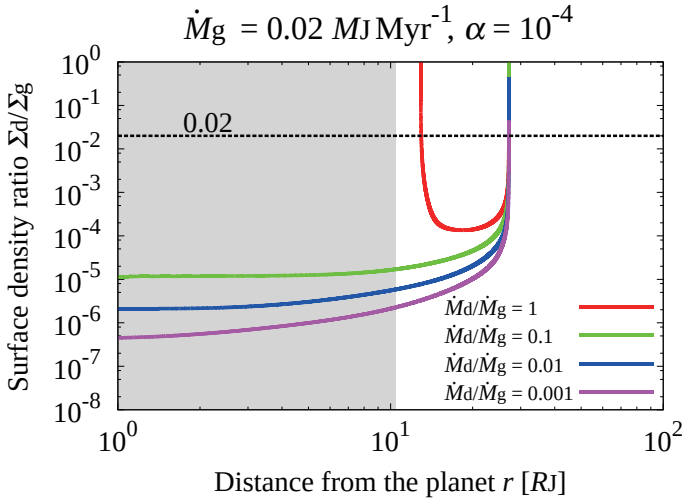

Figure 2.8: **Steady-state profiles of dust-to-gas surface density ratio.** The gas accretion rate is $\dot{M}_{\rm g} = 0.02$ and $\alpha = 10^{-4}$. The dashed line shows the occurrence condition of streaming instability in the most suitable case of St (Carrera et al., 2015).

on the dust-to-gas surface density ratio and the Stokes number of the dust particles. They found that the particle clumps can form if $\Sigma_{\rm d}/\Sigma_{\rm g} > 0.02$ in the most suitable Stokes number condition (see Figure 8 in Carrera et al. (2015)). However, our results showed that the ratio is much lower than the critical value (see Figure 2.8), so that it should be difficult to form satellitesimals via the streaming instability process. Note that water sublimation or recondensation near the snowline can result in an enhancement in the dust surface density and it may be able to trigger streaming instability (Ida et al., 2016; Ida & Guillot, 2016; Schoonenberg & Ormel, 2017).

2.4.4 Validity of the Single-size Approach in Circumplanetary Disks

We used a single-size approach to investigate the growth and drift of dust particles in CPDs. As shown by Sato et al. (2016), this approach is valid for the growth and drift of mass-dominating particles in PPDs, as long as the collisional destruction of the particles is negligible (see also Krijt et al. (2016), Okuzumi et al. (2016), and Tsukamoto et al. (2017) for applications to dust growth in protoplanetary disks).

In principle, the single-size approximation breaks down when there is more than one population of particles that dominates the total dust mass. Unlike our assumption that the

dust inflow onto the CPD is concentrated at the outer edge of the gas inflow region, the dust inflow may be extended over a wide area of the disk. In this case, the size distribution in the inner disk regions may have two peaks of the drifting pebbles that accreted in the outer disk region and the small dust grains directly supplied to the inner disk regions. Actually, when the dust particles strongly couple with the gas, the mass flux of the dust inflow should be proportional to that of the gas $f \propto r^{-1}$. The ratio of the dust mass flux flowing to the inside of r relative to the total dust inflow mass flux is then $\approx r/r_{\rm b}$ which is still about 0.5 even if $r = 15\ R_{\rm J}$ (the orbit of Ganymede). Therefore, the actual size distribution of the dust particles may be wide. We note that our assumption of the concentrated dust inflow may have also caused overestimation of the Stoke number especially in the outer disk regions (St $\propto \dot{M}_{\rm d}^{2/5}$, $\dot{M}_{\rm d}^{2/3}$, or $\dot{M}_{\rm d}^{6/11}$ in our model, see Equations (2.15), (2.17), and (2.18)) and the satellitesimal formation could be harder in reality.

On the other hand, even if the dust particles have a wide size distribution, the smaller particles should grow rapidly and the distribution will narrow. This is because the dust growth timescale $t_{\rm grow}$ must be an increasing function of the dust mass $m_{\rm d}$ in the Newton regime ($t_{\rm grow} \propto m_{\rm d}^{1/4}$ or $m_{\rm d}^{1/3}$ in our model, see Equations (2.5), (2.6), (2.7), and the approximations in Section 2.3.2 and Section 2.5.1) so that the dust particles should grow as orderly growth in most areas within the disk. However, the $m_{\rm d}$ dependence of $t_{\rm grow}$ is weak and we will have to make sure of the validity of the single-size approach by using full-size calculations of dust growth in CPDs in future.

2.4.5 Separation of α coefficient: Turbulent Viscosity and Dust Diffusion

In this thesis, we do not separate the two kinds of α: the turbulent viscosity coefficient $\alpha_{\rm acc}$ and the turbulent diffusion coefficient of dust particles $\alpha_{\rm diff}$. The former determines the evolution of the gas accretion disk and the latter drives the motion of dust particles. Almost all of the previous planet/satellite formation work considered the two values as the same, but actually they are physically different and should be considered separately. Some previous work has carried out MHD simulations of PPDs and showen the relations of the two values. Johansen & Klahr (2005) calculated ideal MHD simulations and directly measures

the turbulent diffusion coefficient of the dust embedded in magneto-rotational turbulence. Johansen et al. (2006) also investigated the effect of an imposed vertical magnetic field on the diffusion. These studies predicted that $\alpha_{\rm acc} \sim 2 - 20\ \alpha_{\rm diff}$. Okuzumi & Hirose (2011) carried out 3D ohmic-resistive MHD simulations and showed that $\alpha_{\rm acc} \sim 5 - 30\ \alpha_{\rm diff}$ on the mid-plane in MRI-inactive "dead-zones". A simple estimate from the outcome value of the rms vertical velocity fluctuation from Bai (2015), which calculated 3D MHD simulations including all three non-ideal MHD effects, suggested that $\alpha_{\rm acc} \gtrsim 10\ \alpha_{\rm diff}$. Given the argument that MRI should be dead in CPDs (Fujii et al., 2014; Keith & Wardle, 2014; Turner et al., 2014; Fujii et al., 2017), it can be deduced that $\alpha_{\rm acc} \gtrsim 10\ \alpha_{\rm diff}$ in CPDs as well.

Therefore, we modify the calculation methods of the gas surface density of the disk, the vertical diffusion of the dust particles, and the dust-dust/dust-gas relative velocities. We substitute $\nu = \alpha_{\rm acc} c_{\rm s} H_{\rm g}$ for Eq. (2.2) in stead of $\nu = \alpha c_{\rm s} H_{\rm g}$ and $\alpha_{\rm diff}$ for Eqs. (2.10) and (2.14) instead of α. Here, isotropic diffusion of dust particles is implicitly assumed. We then calculate the dust evolution as well as previous sections by changing the value of $\alpha_{\rm acc}$ and $\alpha_{\rm diff}$. Figure 2.9 represents the evolution of the Stokes number of fluffy dust particles ($\rho_{\rm int} = 1.4 \times 10^{-4}$g cm^{-3}) with $\alpha_{\rm acc} = 10^{-2}$ and $\alpha_{\rm diff} = 10^{-4}$. This is equivalent to that we change $\alpha_{\rm acc}$ 100 times higher from the case in Figure 2.7 and keep $\alpha_{\rm diff}$ unchanged. As a result, satellitesimal formation becomes easy and even in the case with $\dot{M}_{\rm d}/\dot{M}_{\rm g} = 0.01$, the particles can grow to satellitesimals outside the snowline. This is because the gas surface density of the disk becomes lower and then the drift speed becomes slower, but the vertical diffusion is still weak and so the collision rate does not change. Figure 2.10 shows the result of our parameter study in $\alpha_{\rm acc}$–$\alpha_{\rm diff}$ space. First, the diagonal results are equivalent to those in the previous sections, and actually, they show that the drift, satellitesimal formation, and fragmentation occur when $\alpha_{\rm acc} = \alpha_{\rm diff} = 10^{-5}$, $10^{-4} - 10^{-3}$, and 10^{-2}, respectively. The figure also shows that if $\alpha_{\rm acc}/\alpha_{\rm diff}$ is 10 times larger, satellitesimals can form even if $\dot{M}_{\rm d}/\dot{M}_{\rm g}$ is 10 times smaller. This trend can be understood by the modified version of the Eq. (2.15), the analytical approximation of the Stokes number. The α dependency of the equation can be separated to the $\alpha_{\rm acc}$ and $\alpha_{\rm diff}$ dependencies by reconsidering the analytical deriving

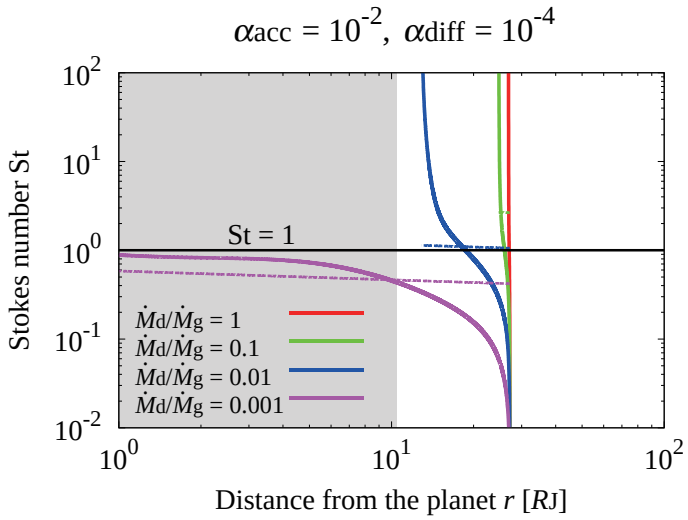

Figure 2.9: **Steady-state profiles of dust with separated α.** The Stokes number St of the highly porous ($\rho_{\rm int} = 1.4 \times 10^{-4}$g cm^{-3}) dust particles with $\alpha_{\rm acc} = 10^{-2}$, $\alpha_{\rm diff} = 10^{-4}$, and $\dot{M}_{\rm g} = 0.02$. The dashed lines are the analytic estimates given by Eqs. (2.15) and (2.16).

process. The dependency of the Stokes number is then, including $\dot{M}_{\rm d}/\dot{M}_{\rm g}$ dependency,

$$\mathrm{St} \propto (\dot{M}_{\rm d}/\dot{M}_{\rm g})^{2/5} \times \alpha^{1/5} \propto (\dot{M}_{\rm d}/\dot{M}_{\rm g})^{2/5} \times \left(\frac{\alpha_{\rm acc}}{\alpha_{\rm diff}}\right)^{2/5} \times \alpha_{\rm diff}^{-1/5}. \tag{2.16}$$

Therefore, a 10 times increase of $\alpha_{\rm acc}/\alpha_{\rm diff}$ is equivalent to a 10 times increase of $\dot{M}_{\rm d}/\dot{M}_{\rm g}$. If our deduction from previous MHD simulations of PPDs is correct, satellitesimal may be able to form even if $\dot{M}_{\rm d}/\dot{M}_{\rm g} \sim 0.01-0.1$. We also note that a 2D hydrodynamical simulation shows that dissipation of spiral shocks transports the angular momentum of CPDs (Zhu et al., 2016), in this case, the horizontal diffusion of the dust particles may become even higher but the vertical diffusion be still low. This effect might make the collision rate higher than considered in this subsection and help the satellitesimal formation even easier.

2.5 Appendix

2.5.1 Approximation of the Stokes Number for Low Gas Density Cases

Although we assume that $C_{\rm D}$ is a constant in Section 2.3.2, this assumption is not correct when the gas density is low by small gas inflow mass flux or strong turbulence. When $\dot{M}_{\rm g} = 0.002\ M_{\rm J}$ Myr^{-1} and $\alpha = 10^{-4}$, or $\dot{M}_{\rm g} = 0.002\ M_{\rm J}$ Myr^{-1} and $\alpha = 10^{-2}$, the particle

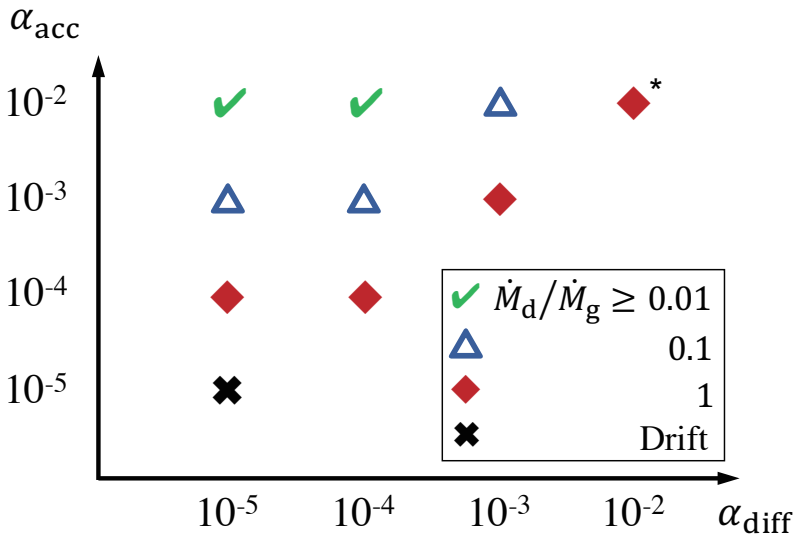

Figure 2.10: **Condition for satellitesimal formation with separated α.** The gas accretion rate is $\dot{M}_{\rm g} = 0.02\ M_{\rm J}\ {\rm Myr}^{-1}$. The particles are highly porous ($\rho_{\rm int} = 1.4 \times 10^{-4}{\rm g\ cm}^{-3}$). The green ticks, blue triangles, red diamonds, and indicate the minimum $\dot{M}_{\rm d}/\dot{M}_{\rm g}$ conditions for satellitesimal formation outside the snowline. The particles drift into the planet at the black cross case. The asterisk indicates the fragmentation must occur.

Reynolds number is with in the range of $10^{-1} \lesssim {\rm Re}_{\rm p} \lesssim 10^2$ for $r \sim 10\ R_{\rm J}$. In this case, $C_{\rm D}$ can be approximated as $C_{\rm D} \approx 12/\sqrt{{\rm Re}_{\rm p}}$ (Equation (2.8)). When $\dot{M}_{\rm g} = 0.002\ M_{\rm J}\ {\rm Myr}^{-1}$ and $\alpha = 10^{-4}$, the dust–dust and dust–gas relative velocities are approximated as $\Delta v_{\rm dd} \approx (1/2)v_{\rm r}$ and $\Delta v_{\rm dg} \approx v_{\rm r}$. The Stokes number St can then be approximated as

$$
\begin{aligned}
{\rm St} \approx 1.6 &\left(\frac{\dot{M}_{\rm d}/\dot{M}_{\rm g}}{1}\right)^{2/3} \left(\frac{\alpha}{10^{-4}}\right)^{-1/9} \\
&\times \left(\frac{\dot{M}_{\rm g}}{0.002\ M_{\rm J}\ {\rm Myr}^{-1}}\right)^{4/9} \left(\frac{T}{90\ {\rm K}}\right)^{-1} \left(\frac{\rho_{\rm int}}{1.4\ {\rm g\ cm}^{-3}}\right)^{-2/9} \left(\frac{M_{\rm cp}}{1\ M_{\rm J}}\right)^{7/9} \left(\frac{r}{10\ R_{\rm J}}\right)^{-13/9},
\end{aligned}
\tag{2.17}
$$

for small r. Unlike in Equations (2.15) and (2.18), St decreases with increasing α, although the dependence is very weak. Strong turbulence diffuses dust particles into the vertical direction and thereby reduces their collision rate (see Equations (2.5) and (2.10)). However, this effect is canceled out by the particle collision velocity induced by turbulence, which increases with increasing α. When $\dot{M}_{\rm g} = 0.02\ M_{\rm J}\ {\rm Myr}^{-1}$ and $\alpha = 10^{-2}$, the two relative velocities are determined by the strength of turbulence (i.e. $\Delta v_{\rm dd} \approx \Delta v_{\rm dg} \approx \Delta v_{\rm t} \approx \sqrt{3\alpha} c_{\rm s} {\rm St}_1^{1/2}$,

see Figure 2.5), for small r,

$$\mathrm{St} \approx 0.73 \left(\frac{\dot{M}_\mathrm{d}/\dot{M}_\mathrm{g}}{0.1} \right)^{6/11} \left(\frac{\alpha}{10^{-2}} \right)^{1/11} \times \left(\frac{\dot{M}_\mathrm{g}}{0.02\ M_\mathrm{J}\ \mathrm{Myr}^{-1}} \right)^{4/11} \left(\frac{T}{160\ \mathrm{K}} \right)^{-1} \left(\frac{\rho_\mathrm{int}}{1.4\ \mathrm{g\ cm}^{-3}} \right)^{-2/11} \left(\frac{M_\mathrm{cp}}{1\ M_\mathrm{J}} \right)^{9/11} \left(\frac{r}{10\ R_\mathrm{J}} \right)^{-15/11} . \tag{2.18}$$

Chapter 3 The Galilean Satellites Formation by Pebble Accretion

This chapter is from

Shibaike, Y., Ormel, C., W., Ida, S., Okuzumi, S., and Sasaki, T., in prep.

3.1 Short Introduction

In Chapter 2, we found that the satellite formation by the classical satellitesimal accretion model with realistic conditions around the planets has severe problems. Therefore, we construct a new alternative scenario for the origin of the Galilean satellites in this chapter. Figure 3.1 represents the outline of our "slow-pebble-accretion" scenario. Only four large planetesimals are captured by the CJD, which slowly accrete the pebbles drifting toward Jupiter as are shown in Chapter 2. We show that this scenario can reproduces the physical, dynamical, compositional, and structural properties of the satellite system.

3.2 Methods

The methods to investigate the scenario include many physics and are complicated. Therefore, we first summarize them and then the details are shown.

3.2.1 Summary of Methods

We model the gas accretion rate as $\dot{M}_{\rm g} = 0.2\exp(-(t - t_{\rm gap})/t_{\rm dep}))\ M_{\rm J}\ {\rm Myr}^{-1}$, where t, $t_{\rm gap}$, $t_{\rm dep}$, and $M_{\rm J}$ are the time after the formation of CAIs, gap opening time, gas depletion timescale of the CSD (we assume $t_{\rm dep} = 3$ Myr), and the current Jupiter mass, respectively. We consider a 1-D viscous accretion CJD. We assume that the gas mass flux is uniform in the CJD and it is equal to both the inflow mass flux to the disk and gas accretion rate to Jupiter, and the mass of Jupiter grows by $\dot{M}_{\rm g}$ from 0.4 $M_{\rm J}$ at $t = t_{\rm gap}$ to 1.0 $M_{\rm J}$ at the end of

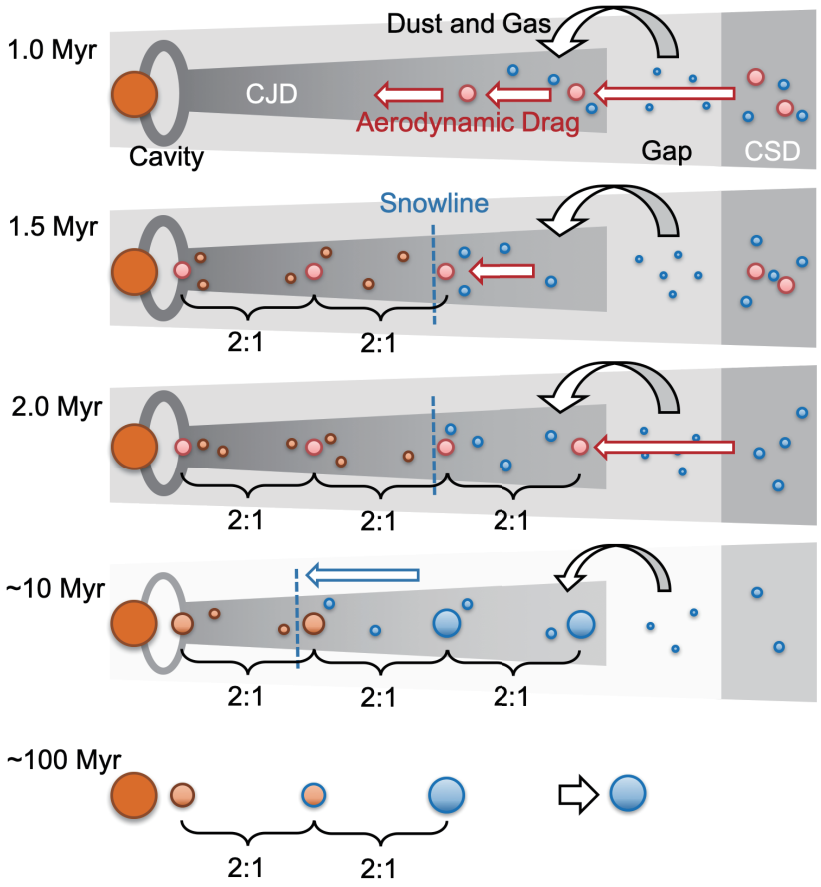

Figure 3.1: **Outline of the new formation scenario for the Galilean satellites.** 1.0 Myr) Jupiter grows to $\approx 0.4\ M_{\rm J}$. The gas accretion rate decreases due to a gap around the CJD and then an inner cavity around Jupiter opens. Pebbles drifting from the outer region of the CSD pile up at the pressure maximum of the gap. Only small dust particles coupled with gas are supplied to the CJD. Some planetesimals form from the pebbles at the pressure maximum. 1.5 Myr) Three planetesimals are captured by the CJD and migrate toward Jupiter by aerodynamic drag. The innermost one stops at the edge of the inner cavity and the two other planetesimals are captured into 2:1 mean motion resonances one by one. The position of the snow line is just inside the third satellite. 2.0 Myr) The fourth planetesimal is captured by the disk. It migrates inward quickly and is captured into a 2:1 resonance with the third one. The difference in capture time between the third and fourth planetesimals creates the dichotomy of their interior ice-rock differentiation. $\sim$ 10 Myr) The four planetesimals grow to almost the same sizes with the current Galilean satellites. The gas accretion rate decreases much because of the depletion of the parent CSD. The snowline then moves to just inside the second satellite (Europa) and small quantities of icy pebbles are accreted onto its outermost shell. $\sim$ 100 Myr) The CJD has disappeared and the fourth satellite (Callisto) escapes from the resonance. The rock-metal differentiation occurs in Io by tidal heating and in Europa and Ganymede by long-lived radiogenic heating.

the calculation. We fix the position of the edge of the cavity $r_{\rm cav}$ at the current position of Io. On the distribution of the disk temperature in our model, the position of the snowline $r_{\rm snow}$ is at Ganymede's orbit when the gap opens and moves to Europa's orbit at the end of the disk evolution.

We first calculate the evolution of dust particles in the CJD using a 1-D single-size analytical formula (Shibaike et al., 2017). They grow to pebbles and then drift to Jupiter because the gas disk rotates with sub-Kepler velocity which is slower than the rotating velocity of the pebbles so that they lose their angular momentum. We assume the dust inflow mass flux as $x\dot{M}_{\rm g}$, where x, the dust-to-gas accretion ratio, is a constant parameter with $x = 0.0026$. The pebble mass flux $M_{\rm p}$ is equal to $x\dot{M}_{\rm g}$ at the outer edge of the disk and is uniform in the disk except for the filtering effects of that outer satellites accrete the pebbles and the evaporation of the pebbles inside the snowline. There are only rocky pebbles inside the snowline and we assume that the pebble mass flux is halved. We also assume that the fragmentation of pebbles occur when their collisional velocity becomes faster than 5 or 50 m s^{-1} for inside or outside the snowline, respectively (Wada et al., 2009). We calculate the disk midplane temperature as $T_{\rm d} = (3GM_{\rm cp}\dot{M}_{\rm g}/(8\pi\sigma_{\rm SB}r^3))^{1/4}g$, where $g = (3/8\tau+1/(4.8\tau))^{1/4}$, $\sigma_{\rm SB}$ and G are the Stefan-Boltzmann constant and the Gravitational constant, respectively (Nakamoto & Nakagawa, 1994). The Rosseland mean opacity is $\tau = \kappa\Sigma_{\rm g}$, where the dust opacity is $\kappa = 450r_{\rm sdg}$ for $T_{\rm d} \geq 160$ K and $\kappa = 450(T_{\rm d}/160\ {\rm K})^2 r_{\rm sdg}$ for $T_{\rm d} < 160$ K. We neglect the effect of the gas opacity ($\sim 10^{-5}$ to 10^{-4} cm^2 g^{-1} (Mizuno, 1980)).

We calculate the mass of the growing seeds as

$$M_{\rm s}(t) = \int_{t_{\rm cap}}^{t} \dot{M}_{\rm p} P_{\rm eff}\, dt, \tag{3.1}$$

where $t_{\rm cap}$ and $P_{\rm eff}$ are the capture time of the seeds and their pebble accretion efficiencies. The pebble accretion efficiency depends on the mass of the seed and the Stokes number of the pebbles around it (Ormel & Liu, 2018).

We also calculate the migration of the seeds by aerodynamic drag and Type I migration which includes both inward and outward migration (Adachi et al., 1976; Weidenschilling,

1977; Paardekooper et al., 2011; Ogihara et al., 2015). We finally consider the capture into 2:1 or 3:2 mean motion resonances (Ogihara & Kobayashi, 2013).

We calculate the surface temperature, $T_s(R_s)$, with the radii of the seeds, R_s, from the equilibrium of the emission and accretion heat of pebbles. We also calculate the cumulative heat of ^{26}Al decay, $\Delta T_{\rm fin}(R)$, from when the pebbles (the ice mass fraction is 0.5) including ^{26}Al have been accreted on the seeds' surface to the end of the formation, where R is the distance from the center of the seeds. We can then estimate the final (i.e. maximum) internal temperature of the seeds at the point R by $T_{\rm fin}(R) = T_s(R) + \Delta T_{\rm fin}(R)$ (Barr & Canup, 2008). We do not include thermal diffusion, solid-state convection, and latent heat inside the seeds.

Here, we show the details of the methods.

3.2.2 Circum-Jovian Disk model

After the gap formation, the gas accretion rate to Jupiter becomes much lower. In this work, we assume that the gas accretion rate is

$$\dot{M}_g = \dot{M}_{g,gap} \exp\left(-\frac{t - t_{gap}}{t_{dep}}\right) \ (t > t_{gap}). \tag{3.2}$$

We also assume that the initial gas accretion rate and the gas depletion timescale are $\dot{M}_{g,gap} = 0.2\ M_J\ {\rm Myr}^{-1}$ and $t_{dep} = 3 \times 10^6$ yr, where M_J is the current Jupiter mass. We set $t = 0$ as the timing of the formation of CAIs. The mass of Jupiter grows by $\dot{M}_g$ from 0.4 M_J at $t = t_{gap}$ to 1.0 M_J at the end of the calculation. The accretion rate is equal to the inflow mass flux from the circum-stellar disk (CSD) to circum-Jovian disk (CJD) because we assume that the flow of gas (and pebbles) in whole region of the disk is semi-steady and all of the gas flow into the disk will be accreted by Jupiter eventually.

A cavity of the gas disk can open around Jupiter by the magnetic field of the planet. The timing that the inner cavity opens depends on the strength of the magnetic field. The position of the disk inner edge can be estimated from the balance of gas accretion and magnetic stress (Lovelace et al., 2011; Liu et al., 2017). If Jupiter has a dipole magnetic

field, it is given by

$$\begin{aligned} r_{\rm cav} =& \left(\frac{B_{\rm cp}^4 R_{\rm cp}^{12}}{4GM_{\rm cp}\dot{M}_{\rm g}^2} \right)^{1/7} \\ =& 1.07 \left(\frac{B_{\rm cp}}{40\ {\rm Gauss}} \right)^{4/7} \left(\frac{R_{\rm cp}}{R_{\rm J}} \right)^{12/7} \left(\frac{M_{\rm cp}}{0.4\ M_{\rm J}} \right)^{-1/7} \left(\frac{\dot{M}_{\rm g}^2}{0.2\ M_{\rm J}\ {\rm Myr}^{-1}} \right)^{-2/7} [R_{\rm J}], \end{aligned} \tag{3.3}$$

valid for $r_{\rm cav} < r_{\rm co}$ where $r_{\rm co}$ is the corotation radius (see Section 3.5.2). In the equation, $B_{\rm cp}$, $R_{\rm cp}$, G, and $M_{\rm cp}$ are the strength of the magnetic field of the central planet, radius of the central planet, gravitational constant, and mass of the central planet, respectively. Current Jupiter has a magnetic field and its strength on the surface of the equational region of the planet is 4.2 Gauss (Connerney, 1993). Previous work, however, argued that the magnetic field was once stronger than the current one (Stevenson et al., 1983; Sánchez-Lavega, 2004; Christensen et al., 2009). Therefore, we consider that the magnetic field is $\approx$ 40 Gauss. In this case, the disk inner cavity and gap open at almost same time (substituting the Jupiter radius $R_{\rm J}$ at $r_{\rm cav}$ for Eq. (3.3)). On the other hand, if the strength of the magnetic field is the same with the current one, the cavity only opens 14 Myr later than the gap opening. In this case, any satellite would be consumed by proto-Jupiter ($t < 14$Myr) and too little material would remain to form form the Galilean satellites after gap opening. We summarize the evolution of $\dot{M}_{\rm g}$ in Figure 3.2. In our model, we assume that $r_{\rm cav}$ is fixed at Io's orbit for simplicity.

Based on the above gas accretion model, we calculate the evolution of the 1-D CJD. The gas surface density of the viscous accretion disk is[1]

$$\Sigma_{\rm g} = \frac{\dot{M}_{\rm g}\Omega_{\rm K}}{3\pi\alpha c_{\rm s}^2}. \tag{3.4}$$

We assumed that the strength of turbulence is $\alpha = 10^{-4}$ because the MRI should not have occurred in the CJD (Fujii et al., 2014). The upper left panel of Figure 3.3 represents the evolution of the gas surface density. The gas surface density becomes small as the gas accretion rate decreases.

[1]The equation can be derived from Eq. (2.2) by neglecting the first term on the right-hand.

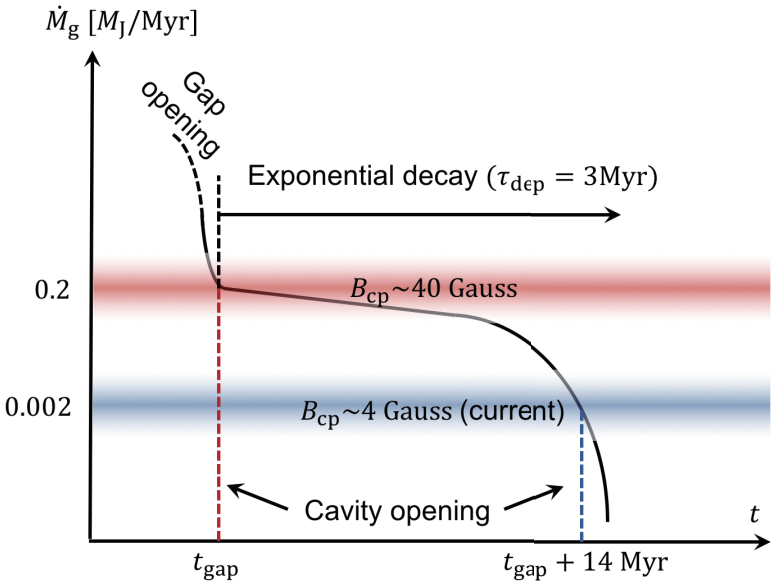

Figure 3.2: **Model of the gas accretion rate.** The black solid curve represents the evolution of the gas accretion rate in our model. After the gap opens at $t = t_{\rm gap}$, the accretion rate decreases exponentially. The red and blue regions represent the gas accretion rates required for the gap opening if the strength of Jupiter's magnetic field is $B_{\rm cp} \approx 40$, or 4 Gauss (i.e. the current strength), respectively. The red and blue dashed lines represent the time (after the formation of CAIs) that the inner cavity opens if $B_{\rm cp} \approx 40$ or 4 Gauss, respectively.

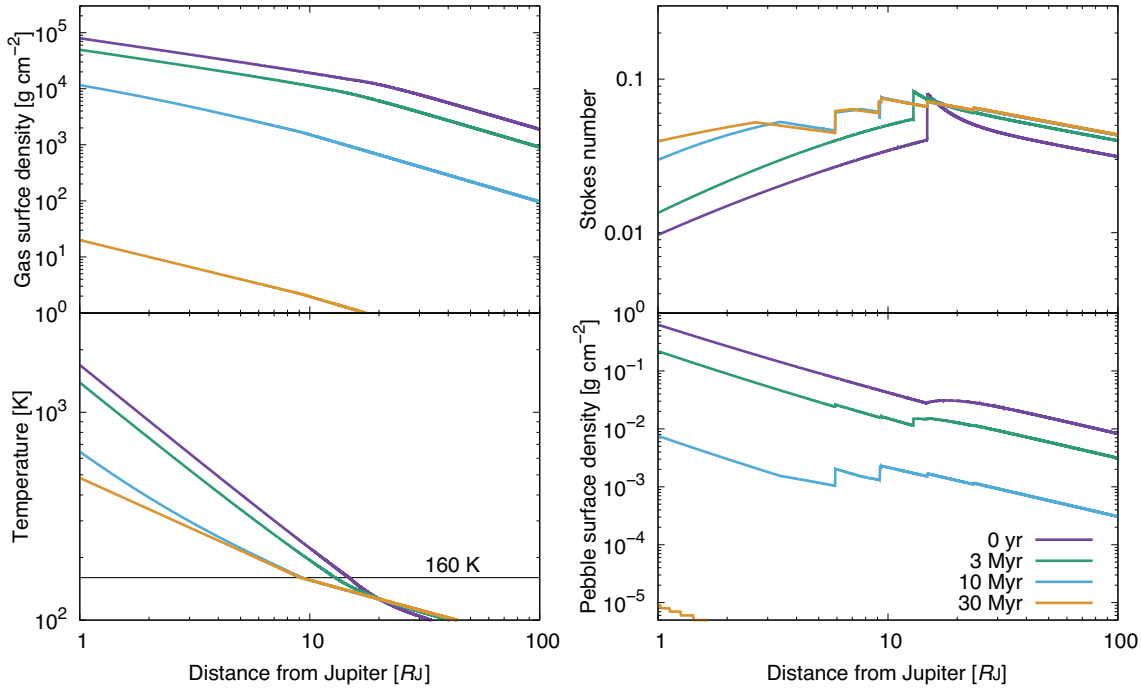

Figure 3.3: **Evolution of the circum-Jovian disk and the pebbles.** The left upper and lower panels represent the evolution of the gas surface density and the temperature of the mid-plane, respectively. The black horizontal line is the sublimation temperature of water ice, 160 K. The right upper and lower panels represent the evolution of the Stokes number of the drifting pebbles and the pebble surface density, respectively. The color variations of the both panels represent the time after the gap opens ($t - t_{\rm gap}$).

We assume that the CJD is viscously heated. The gas temperature in the midplane of the viscous accretion disk is given by (Nakamoto & Nakagawa, 1994)[2],

$$T_{\rm d} = \left(\frac{3GM_{\rm cp}\dot{M}_{\rm g}}{8\pi\sigma_{\rm SB}r^3} \right)^{1/4} g, \tag{3.5}$$

where $\sigma_{\rm SB}$ is the Stefan-Boltzmann constant and[3],

$$g = \left(\frac{3}{8}\tau + \frac{1}{4.8\tau} \right)^{1/4} \tag{3.6}$$

is a function of the Rosseland mean optical depth $\tau = \kappa\Sigma_{\rm g}$. In principle, the opacity κ depends on the size distribution of the smallest dust particles. However, the size distribution cannot be predicted from the simple dust evolution model as employed in this study. Therefore, we just assume $r_{\rm sdg}$, the ratio of the surface densities of the small grains that affect the temperature and the gas. Then, the opacity can be assumed as

$$\kappa = \begin{cases} 450 r_{\rm sdg} & T_{\rm d} \geq 160 \text{ K} \\ 450 \left(T_{\rm d}/160 \text{ K}\right)^2 r_{\rm sdg} & T_{\rm d} < 160 \text{ K}. \end{cases} \tag{3.7}$$

The lower left panel of Figure 3.3 represents the evolution of the temperature when $r_{\rm sdg} = 1.65 \times 10^{-7}$. We choose this value to get the thermal condition that the snowline is just inside current Ganymede's orbit. The slopes on curves change at the snowline where the temperature is 160 K. The Rosseland mean optical depth τ becomes the smallest (~ 1) slightly outside the snowline. The temperature decrease as the gas accretion rate reduces. The temperature depends on this ratio $r_{\rm sdg}$ and we discuss the effects by this dependency in Section 3.5.3 in detail.

3.2.3 Pebble Growth and Radial Drift

We calculate the distributions of the Stokes number and surface density of the drifting pebbles in the CJD. We only consider semi-steady conditions of pebbles because the evolution timescale of the pebbles is much shorter than those of the disk and satellites. In this case,

[2]The equation is the same with Eq. (2.3) in Section 2.2.1.
[3]The equation is the same with Eq. (2.4) in Section 2.2.1.

the pebble mass flux in the CJD $\dot{M}_{\rm p}$ does not depend on the distance from Jupiter r. It is also equal to the mass flux of dust particles supplied from the parent CSD to the CJD,

$$\dot{M}_{\rm p} = x\dot{M}_{\rm g}, \tag{3.8}$$

where x is the ratio of the dust-to-gas accretion rates. We treat this ratio as a parameter and assume that the ratio does not depend on time, for simplicity. However, the mass flux of pebbles drifting inside the snowline is smaller than that of outside because pebbles lose their H_2O ice inside the snowline. We assume that $\dot{M}_{\rm p}$ inside the snowline becomes half of that of outside. We also consider the filtering effect by outer satellites.

Under these assumptions, we first calculate the Stokes number of the pebbles. When the Stokes number is determined by radial drift, it can be calculated by the following equation (modified version of Eq. (2.15) in Section 2.3.1),

$$\begin{aligned} {\rm St_p} = 0.23 &\left(\frac{2}{3+2p+q}\right)^{4/5}\left(\frac{10}{18-39q}\right)^{2/5} \\ &\times\left(\frac{\dot{M}_{\rm p}/\dot{M}_{\rm g}}{0.003}\right)^{2/5}\left(\frac{\alpha}{10^{-4}}\right)^{1/5}\left(\frac{T_{\rm d}}{160\ {\rm K}}\right)^{-2/5}\left(\frac{M_{\rm cp}}{1\ M_{\rm J}}\right)^{2/5}\left(\frac{r}{10\ R_{\rm J}}\right)^{-2/5}, \end{aligned} \tag{3.9}$$

where p and q are the r exponents of the gas surface density and temperature (i.e. $\Sigma_{\rm g} \propto r^{-p}$ and $T_{\rm d} \propto r^{-q}$).

However, fragmentation occurs if the collision velocity, in other words, the pebble-to-pebble relative velocity is too fast. This relative velocity is[4],

$$v_{\rm pp} = \sqrt{(v_{\rm r}/2)^2 + v_{\rm t}^2}, \tag{3.10}$$

where $v_{\rm r}$ and $v_{\rm t}$ are the radial drift velocity of the pebbles and the relative velocity induced by turbulence, respectively. These two velocities are (Adachi et al., 1976; Weidenschilling, 1977; Ormel & Cuzzi, 2007)[5]

$$v_{\rm r} = -2\frac{{\rm St_p}}{{\rm St_p}^2+1}\eta v_{\rm K}, \tag{3.11}$$

[4]The equation can be derived from Eq. (2.13) by neglecting $\Delta v_{\rm B}^2$, Δv_ϕ^2, and $\Delta v_{\rm z}^2$ on the right-hand.

[5]The equation is the same with Eq. (2.11) in Section 2.2.2 except the subscript of St.

where $v_{\rm K} = r\Omega_{\rm K}$ is the Kepler velocity, and[6]

$$v_{\rm t} = \sqrt{3\alpha} c_{\rm s} {\rm St_p}^{1/2}. \tag{3.12}$$

If the Stokes number is determined by their fragmentation, it is

$${\rm St_p} = \frac{-3\alpha c_s^2 + \sqrt{9\alpha^2 c_s^4 + 4\eta^2 r^2 \Omega_K^2 v_{\rm cr}^2}}{2\eta^2 r^2 \Omega_K^2}, \tag{3.13}$$

where $v_{\rm cr}$ is the critical fragmentation speed (Okuzumi et al., 2016). This equation can be derived by substituting Eq. (3.11), (3.12), and $v_{\rm pp} = v_{\rm cr}$ for Eq. (3.10).

Finally, the pebble surface density can be calculated by the continuity equation,

$$\Sigma_{\rm p} = \frac{\dot{M}_{\rm p}}{2\pi r v_{\rm r}}. \tag{3.14}$$

The right panels of Figure 3.3 represent the evolution of the Stokes number and the surface density of the dust particles (i.e. pebbles). The stair around 10 $R_{\rm J}$ is consistent with the position of the snowline. The snowline migrates inward because the temperature becomes lower as the gas accretion rate decreases. We also find that the Stokes number inside the snowline is smaller than that outside. Outside the snowline, the Stokes number is determined by drift (Eq. (3.9)). While, inside the snowline, the Stokes number is determined by fragmentation (Eq. (3.13)) because rocky particles are more fragile than icy ones (Wada et al., 2009). We assume that the critical fragmentation speeds of rocky and icy pebbles are $v_{\rm cr} = 5$ and 50 m s^{-1}, respectively. In the right panels of Figure 3.3 the minor stairs reflect the accretion of pebbles by the planets. As time goes on and the satellites grow larger, the pebble accretion efficiency increases, resulting in larger jumps (see Section 3.2.4). Although we do not consider the inner cavity in this calculation, the rocky pebbles should flow onto the planet with the gas because they are small enough to couple to the magnetospheric accretion flow of gas. Their dynamical timescale should be about the free-fall timescale, and the stopping time of pebbles is much smaller than it because the upper panel of Figure 3.3 shows that the Stokes number is about 0.02 around the cavity (5.89 $R_{\rm J}$). Note that, however, there is a possibility that the settling of pebbles onto the midplane prevents them from flowing into the planet with the magnetospheric gas flow.

[6]The equation is the same with the middle line of Eq. (2.14) in Section 2.2.2 except the subscript of St.

3.2.4 Pebble Accretion Efficiency

According to recent N-body simulations, the pebble accretion efficiency is well-fitted by (Liu & Ormel, 2018)

$$P_{\rm eff} = \left\{ \left(0.31 \sqrt{\frac{\mu_s \Delta v / v_{\rm K}}{{\rm St_p}\eta^2}} \right)^{-2} + \left(0.39 \frac{\mu_{\rm s}}{\eta h_{\rm p}} \right)^{-2} \right\}^{-1/2}, \tag{3.15}$$

where $\mu_{\rm s} = M_{\rm s}/M_{\rm cp}$ and $h_{\rm p} = H_{\rm p}/r$ are the satellite-to-central planet mass ratio and the pebble aspect ratio, respectively. This equation combines two regimes of pebble accretion, 2-D (the first term) and 3-D (the second term) limits. If the pebble accretion radius is larger than the pebble scale height $H_{\rm p}$, the first term is dominant. The pebble scale height can be derived analytically from the balance of their vertical sedimentation and diffusion (Youdin & Lithwick, 2007)[7],

$$H_{\rm p} = H_{\rm g} \left(1 + \frac{{\rm St_p}}{\alpha} \frac{1 + 2{\rm St_p}}{1 + {\rm St_p}} \right)^{-1/2}, \tag{3.16}$$

where $H_{\rm g} = c_{\rm s}/\Omega_{\rm K}$ is the gas scale height. The expression in the 2-D limit depends on the approach velocity of the pebbles Δv, which is given by the Keplerian shear in the disk or else the disk head wind. The approach velocity is (Ormel & Liu, 2018)

$$\Delta v / v_{\rm K} = 0.52(\mu_{\rm s}{\rm St_p})^{1/3} + \eta \left\{ 1 + 5.6 \left(\frac{\mu_{\rm s}}{\eta^3/{\rm St_p}} \right) \right\}^{-1}. \tag{3.17}$$

The pebble mass flux within an orbit of the seed is smaller than without because a fraction of drifted pebbles are captured by the embryo,

$$\dot{M}_{\rm p,in} = (1 - P_{\rm eff}) \dot{M}_{\rm p,out}, \tag{3.18}$$

where $\dot{M}_{\rm p,in}$ and $\dot{M}_{\rm p,out}$ are the fluxes inside and outside the embryo, respectively. The upper panel of Figure 3.4 represents $P_{\rm eff}$ of Seeds1 to 4. All pebble accretion efficiencies of the satellites are smaller than $\sim 10\%$. The lower panel represents the growth timescale of the seeds, $t_{\rm grow} = M_{\rm s}/(dM_{\rm s}/dt)$.

In this work, we assume that all seeds are in the settling regime and they always accrete pebbles effectively. The effective pebble accretion occurs only if the mass becomes larger

[7]The equation is the same with Eq. (2.10) in Section 2.2.2 except the subscripts of H and St.

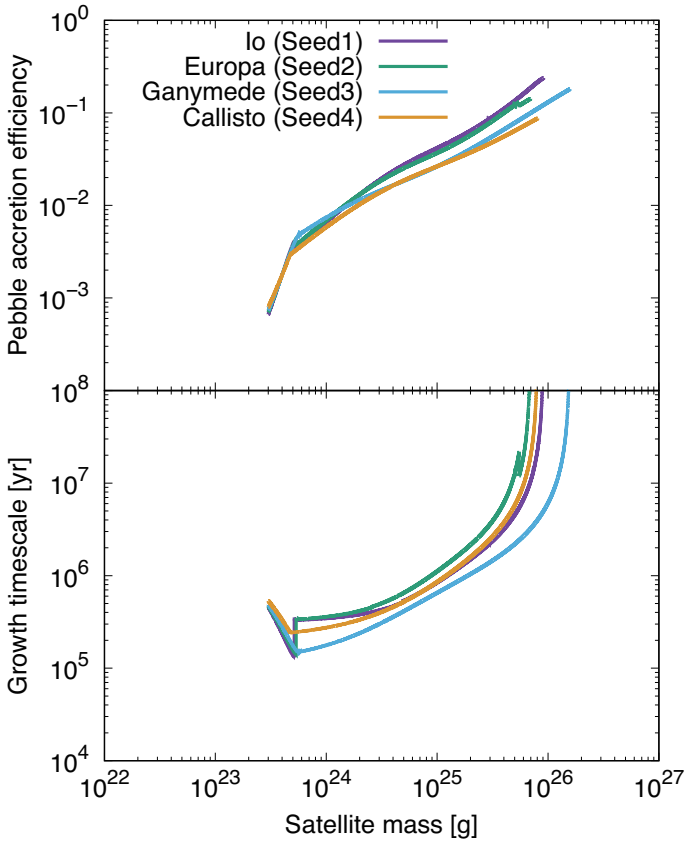

Figure 3.4: **Pebble accretion efficiency and growth timescale.** The purple, green, light blue, and orange curves in the upper panel represent the pebble accretion efficiencies of Seeds1 to 4, respectively. The lower panel is the growth timescale of the seeds.

than a critical mass (Ormel, 2017),

$$M_* = \frac{v_{\rm hw}^3 t_{\rm stop}}{8G} = \frac{1}{8}\eta^3 {\rm St_p} M_{\rm cp}. \tag{3.19}$$

In our CJD model, we found that the gas aspect ratio $h_{\rm g}$ is about 0.1 in the whole disk regions and the Stokes number of the pebbles is ${\rm St_p} = 0.1$ (See Figures 3.3). Then, the critical mass is $M_* \sim 10^{-8} M_{\rm cp}$, which is about 10 times smaller than the initial mass $M_{\rm ini} = 3 \times 10^{23}$g. On the other hand, pebble accretion stops if a gap structure forms around the seed. We ignore this effect because the critical mass (generally called the pebble isolation mass) $M_{\rm iso}$ is larger than the mass of the largest Galilean satellite Ganymede, $0.78 \times 10^{-4} M_{\rm J}$. The pebble isolation mass is (Ataiee et al., 2018)

$$M_{\rm iso} = h_{\rm g}^3 \sqrt{37.3\alpha + 0.01} \times \left\{ 1 + 0.2 \left(\frac{\sqrt{\alpha}}{h_{\rm g}} \sqrt{\frac{1}{{\rm St_p}^2} + 4} \right)^{0.7} \right\} M_{\rm cp}, \tag{3.20}$$

where $h_{\rm g} = H_{\rm g}/r$ is the gas aspect ratio. Then, the isolation mass in our disk model is $M_{\rm iso} \approx 1.4 \times 10^{-4}\ M_{\rm cp}$.

3.2.5 Satellite Internal Temperature

We estimate the internal temperature of satellites to discuss their differentiation. The surface temperature of satellites with radius $R_{\rm s}$, can be estimated by the following equation (Barr & Canup, 2008). The temperature $T_{\rm s}(R_{\rm s})$ is

$$\rho_{\rm s} C_{\rm p} (T_{\rm s}(R_{\rm s}) - T_{\rm d}) = \frac{1}{2} \frac{\dot{M}_{\rm s} u_{\rm i}^2}{4\pi R_{\rm s}^2} - \sigma_{\rm SB} (T_{\rm s}(R_{\rm s})^4 - T_{\rm d}^4). \tag{3.21}$$

This equation represents the balance of the energy in the thin layer of the pebbles accreted during the unit time on the surface of the satellites. The left-hand side is the energy necessary for heating the thin layer. The terms of the right-hand side are the collisional energy of the accreted pebbles and the emission form the surface. The pebble-satellite collision velocity $u_{\rm i}$ can be estimated by

$$u_{\rm i} = \min(\sqrt{v_{\rm esc}^2 + \Delta v^2}, v_{\rm set}), \tag{3.22}$$

where $v_{\rm esc} = \sqrt{2GM_{\rm s}/R_{\rm s}}$ and $v_{\rm set} = g_{\rm s} t_{\rm stop}$ are the escape and settling velocities, respectively. The gravitational field of satellite is $g_{\rm s} = GM_{\rm s}/R_{\rm s}^2$.

Heating by ^{26}Al is also very effective. The increase of the satellite internal temperature at R, distance from the center of the satellite, during the formation is

$$\begin{aligned}\Delta T_{\rm fin}(R) =& \frac{1}{C_{\rm p}} \int_{t_{\rm acc}}^{t_{\rm fin}} m_{\rm r} q_{26}(t) dt \\ =& \frac{m_{\rm r} q_{26,0}}{C_{\rm p} \lambda_{26}} \exp(-\lambda_{26} t_{\rm acc}),\end{aligned} \tag{3.23}$$

where $t_{\rm acc}$ and $t_{\rm fin}$ are the time when the satellite radius $R_{\rm s}$ was equal to R and the end of the formation (Barr & Canup, 2008). Here, we assume that all ^{26}Al heat has remained at the point until the end. Thermal diffusion can be ignored because it diffuses only $\sim$ 10 km in 10^7 years. Solid-state convection can also be ignored because it can start at $t \sim 10^8$ year (Barr & Canup, 2008). Latent heat is not included because the purpose of this estimation is to determine whether the satellites melt or not. The final (i.e. maximum) satellite internal temperature at R can be then estimated by the sum of the two heating sources, the accretion heating and the ^{26}Al heating,

$$T_{\rm fin}(R) = T_{\rm s}(R) + \Delta T_{\rm fin}(R). \tag{3.24}$$

Note that the ^{26}Al heating is dominant (see Section 3.5.1).

3.2.6 Satellite Migration

There are two main mechanisms that make satellites migrate in the disk, aerodynamic drag and Type I migration. We consider both two mechanisms at the same time to calculate the migration of satellites. The aerodynamic drag migration velocity can be obtained by substituting the Stokes number of satellites, $\mathrm{St_s}$, for $\mathrm{St_p}$ of Eq. (3.11),

$$v_{\rm gd} = -2 \frac{\mathrm{St_s}}{\mathrm{St_s}^2 + 1} \eta v_{\rm K}. \tag{3.25}$$

The Stokes number of satellites is[8]

$$\mathrm{St_s} = \frac{8}{3 C_{\rm D}} \frac{\rho_{\rm s} R_{\rm s}}{\rho_{\rm g} \eta v_{\rm K}} \Omega_{\rm K}. \tag{3.26}$$

[8]The equation is the same with Eq. (2.7) in Section 2.2.2 except the subscripts of St, ρ, and R.

Table 3.1: The capture coefficient $C_{\rm MMR}$ for 2:1 or 3:2 mean motion resonances

Mass ratio	2:1	3:2
$M_{\rm out}/M_{\rm in} \sim 1$	1×10^6	2×10^5
$M_{\rm out}/M_{\rm in} \lesssim 0.1$	1×10^7	5×10^5

The Type I migration velocity is,

$$v_{\rm t1} = b_{\rm t1} \left(\frac{M_{\rm s}}{M_{\rm cp}} \right) \left(\frac{\Sigma_{\rm g} r^2}{M_{\rm cp}} \right) \left(\frac{v_{\rm K}}{c_{\rm s}} \right)^2 v_{\rm K}, \tag{3.27}$$

where $b_{\rm t1}$ is the migration constant depends on the distribution of the temperature and gas surface density of the CJD (see Eq. (10) of Ogihara et al. (2015)). If $b_{\rm t1}$ is negative or positive, the satellite migrates inward or outward, respectively.

3.2.7 Capture into Mean Motion Resonances

According to a recent N-body simulation, the critical migration timescale for capture into mean motion resonances is (Ogihara & Kobayashi, 2013),

$$t_{\rm crit} = C_{\rm MMR} \left(\frac{M_{\rm in}}{M_\oplus} \right)^{-4/3} \left(\frac{M_{\rm cp}}{M_\odot} \right)^{4/3} T_{\rm in}, \tag{3.28}$$

where $M_{\rm in}$, $M_\oplus$, and $M_\odot$ are the mass of the inner satellite, Earth, and Sun, respectively, and $T_{\rm in}$ is the orbital period of the inner satellite. If the migration timescale $t_{\rm mig} = r/(v_{\rm gd} + v_{\rm mig})$ is longer than this critical timescale, the two bodies can be captured into the resonance. The capture coefficient $C_{\rm MMR}$ depends on the type of the resonance and the mass ratio of the two bodies. We summarize the values of $C_{\rm MMR}$ in Table 3.1 cited from Ogihara & Kobayashi (2013) which calculated numerical simulations (Ogihara & Kobayashi, 2013). Note that our 1-D model can not consider the eccentricity and inclination of the orbits.

3.2.8 Parameters and Constants in Chapter 3

We summarize the parameters and constants used in Chapter 3 in Table 3.2. We assume that the values of x, $r_{\rm sdg}$, and α do not depend on time. We also assume that the rock mass fraction outside the snowline is $m_{\rm r} = 0.5$. In this case, $q_{26,0}$, $C_{\rm p}$, and $\rho_{\rm s}$ can be assumed as the values in the table (Barr & Canup, 2008).

Table 3.2: Parameters and constants in Chapter 3

	Value*	Description
$t_{\rm gap}$	$0, \mathbf{1.0}, 2.0, 3.0$ Myr	Gap opening time
x	$0.0021, \mathbf{0.0026}$	Dust-to-gas accretion rate ratio
α	$10^{-5}, \mathbf{10^{-4}}$	Strength of the turbulence
$r_{\rm sdg}$	$1.7\times10^{-8}, \mathbf{1.7\times10^{-7}}, 1.7\times10^{-6}$	Small grain-to-gas surface densities ratio
$t_{\rm cap}$	$\mathbf{1.0}, \mathbf{1.25}, \mathbf{1.5}, \mathbf{2.0}$ Myr	Capture time
$M_{\rm s,start}$	$10^{23}, \mathbf{3\times10^{23}}$ g	Initial mass of satellites (seeds)
$\dot{M}_{\rm g,gap}$	$0.2\ M_{\rm J}$ Myr^{-1}	Initial gas accretion rate
$t_{\rm dep}$	3×10^6 yr	Gas depletion timescale
$M_{\rm cp,gap}$	$0.4\ M_{\rm J}$	Initial mass of the central planet
$r_{\rm s,start}$	$50\ R_{\rm J}$	Initial (captured) position of satellites (seeds)
$t_{\rm fin}$	3×10^7 yr	Time of the end of the formation
$m_{\rm g}$	3.9×10^{-24} cm^3 g s^{-2}	Mean molecular mass of gas
$C_{\rm D}$	0.5	Drag coefficient
$m_{\rm r}$	0.5	Rock mass fraction outside the snowline
$v_{\rm cr}$	$5, 50$ m s^{-1}	Critical fragmentation speed of rocky/icy pebbles
$C_{\rm MMR}$	Table 3.1	Capture coefficient
λ_{26}	9.68×10^{-7} yr^{-1}	Decay rate of ^{26}Al
$q_{26,0}$	1.82×10^{-7} W kg^{-1}	Initial heating rate by ^{26}Al
$C_{\rm p}$	1400 J kg^{-1} K^{-1}	Specific heat (for Ganymede and Callisto)
$\rho_{\rm s}$	1.9 g cm^{-3}	Satellite density (for Ganymede and Callisto)

* The boldface shows the fiducial case.

Table 3.3: Final properties of the satellites

Seeds	Capture time [Myr]	Final Mass [10^{25} g]	Final Position [R_J]	Final Ice Mass Fraction
Seed1 (Io)	1.0	9.14 (8.93)	5.89 (5.89)	0.0028 (0.00)
Seed2 (Europa)	1.25	6.98 (4.80)	9.35 (9.38)	0.11 (0.08)
Seed3 (Ganymede)	1.5	15.8 (14.8)	14.8 (15.0)	0.50 (0.45)
Seed4 (Callisto)	2.0	8.08 (10.8)	23.6 (26.3)	0.50 (0.56)

3.3 Results

We calculate the evolution of the mass and orbits of four planetesimals (Seeds1 to 4) captured by the CJD one by one (see Table 3.3). We assume the initial mass and positions of the seeds as $M_{\rm s,start} = 3 \times 10^{23}$ g and $r_{\rm s,start} = 50\ R_{\rm J}$, respectively. Figure 3.5 represents the evolution of the size and orbits of the seeds, and Table 3.3 lists the final mass and positions. Figure 3.5 and Table 3.3 show that the mass (sizes) of the Galilean satellites can be reproduced very well. The dichotomy of the size between the inner and outer two satellites is created by the assumption that the pebble mass flux inside the snow line is half of that of outside because icy pebbles evaporate inside the snowline. Note that their mass does not reach the pebble isolation mass and the filtering effect of pebbles by outer satellites are small enough (see Supplementary Section S1.3). Figure 3.5 also shows that all seeds migrate quickly ($< 3 \times 10^5$ year) by aerodynamic drag (not by Type I migration) and are captured into 2:1 resonances one by one from the inner ones. After the seeds are captured into the resonances, they grow by pebble accretion without migration and keep their orbits on the current ones. The position of Seed4 is, on the other hand, different from the real orbit of Callisto. Seed4 is also captured into a 2:1 resonance with Seed3.

Each Galilean satellite has different ice mass fraction and, in particular, the low ice mass fraction of Europa is very unique (Table 3.3). We calculate the ice mass fractions of the growing seeds and find that this low ice mass fraction of Europa ($\approx$ 8%) can be reproduced by the migration of the snowline at the final phase of the formation (Table 3.3). Figure 3.5 shows that Seed2 (Europa) accretes icy pebbles after 10 Myr. Although the ice mass fraction strongly depends on the distribution of the disk temperature, there is a disk condition which is suitable for reproducing the ice mass fractions of all the Galilean satellites. In our model ice sublimation occurs instantaneously at the snowline, in contrast

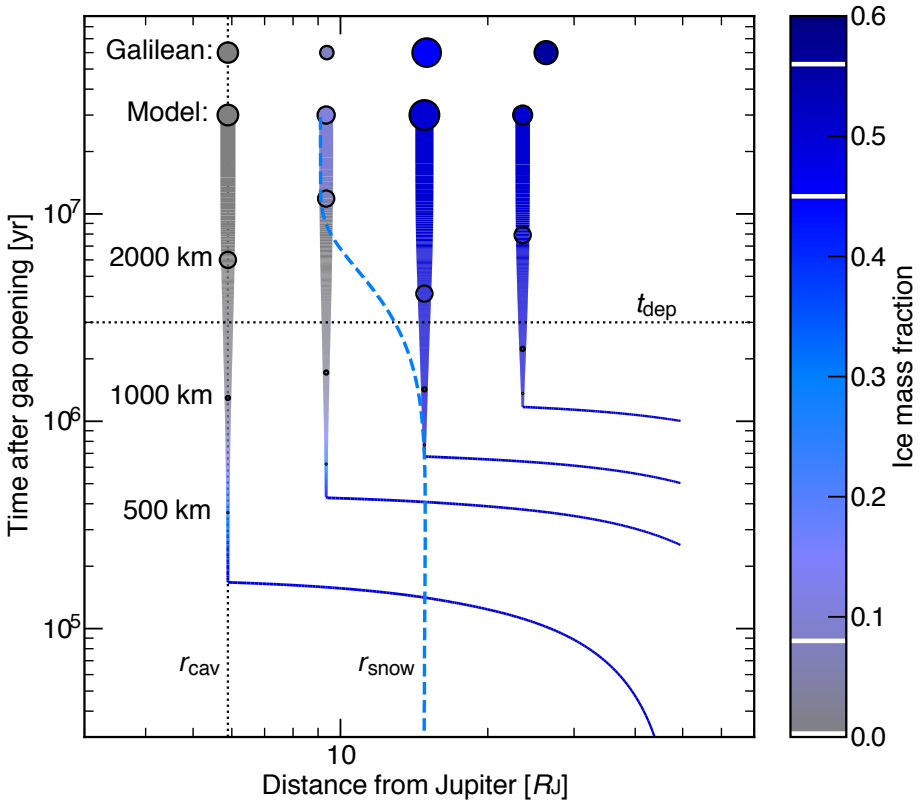

Figure 3.5: **Evolution of the four satellites.** The solid curves represent the positions of the evolving seeds at the time after the gap opens (i.e. $t - t_{\rm gap}$). The sizes of the circles represent the radii of the seeds and the current Galilean satellites. The color scales of the curves range from gray to dark blue for the increasing ice mass fractions of the seeds. The blue dashed curve represents the position of the snowline. The position of the edge of the inner cavity is fixed at the current orbit of Io (the vertical dotted line). The horizontal dotted line represents the gas depletion timescale of the CSD. The values of the initial and final mass, positions, and ice mass fractions are shown in Table 3.3.

to a previous one (Ronnet et al., 2017). Europa also naturally acquired an icy surface on top of a rocky interior, because the satellite accretes dry pebbles before accreting ice-rich pebbles.

We estimate the internal temperature of Seed3 and 4 and find that, in order to avoid differentiation of Callisto by ^{26}Al heat, its seed must be captured by the disk late enough. Figure 3.6 represents the internal temperature of Ganymede (Seed3, light blue) and Callisto (Seed4, orange). The first one is higher than the melting point of Callisto (black) and the second one is lower than it. This means that Callisto does not melt but Ganymede may melt by ^{26}Al heat. The dichotomy of their internal ice-rock differentiation can be created by the difference in their capture time, 0.5 Myr, because the half-life of ^{26}Al is 0.717 Myr. The long growth timescale ($\sim 10^7$ yr) is the reason why such different capture time is allowed. If the growth timescale is shorter and the difference in the capture time is the same, the final mass of Ganymede and Callisto would end up too large. Indeed, it is difficult to make the dichotomy between the internal structures of the two satellites by the classical Canup-Ward formation scenario where the growth timescale is $< 10^6$ yr (Barr & Canup, 2008). Note that once rock-metal cores form in Europa and Ganymede, they can also differentiate metallic cores by long-lived radiogenic heating (Spohn & Breuer, 1998), and Io can be differentiated completely by tidal heating after its formation with its current orbit (Peale et al., 1979).

3.4 Assessment

Our new slow-pebble-accretion scenario reproduces most of the important properties of the current Galilean satellites; mass, orbits, ice mass fractions, and internal structures. Although some key assumptions which determine each characteristics of the satellites are needed to reproduce them, most of the assumptions are supported by previous predictions or observations. We summarize these in Table 3.4 and discuss in the followings. The first column lists the key assumptions of our model and the second and third columns describe the motivations for them.

We consider a situation that the gas accretion rate decreases by the gap opening around

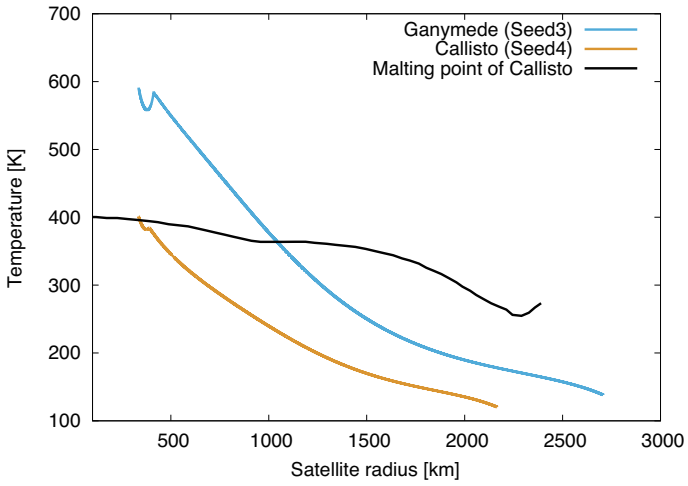

Figure 3.6: **Internal temperature of Ganymede and Callisto.** The light blue and orange curves represent the final ($t - t_{\rm gap} = 30$ Myr) internal temperature of Ganymede (Seed3) and Callisto (Seed4). The black curve is the melting point of Callisto cited by Figure 5 in Barr & Canup (2008).

Table 3.4: Summary of the key assumptions and their validity

Key assumptions	Reproduced characteristics	Supporting predictions or observations
$t_{\rm dep} = 3$ Myr	-	Lifetime of PPDs
$r_{\rm cav} = 5.89\ R_{\rm J}$	Position of Io	Stronger magnetic field of young Jupiter Larger radius of young Jupiter
$\alpha = 10^{-4}$	-	Inactivity of MRI in CPDs
$\tau \sim 1$ at Ganymede ($r_{\rm sdg} = 1.7 \times 10^{-7}$)	Ice mass fractions of all the satellites	Accretion energy dissipation at high altitude
Four seeds	Four large Jovian satellites	Low likelihood of planetesimal-capture
Circular orbits	Resonances of the inner three satellites	Long-lived prograde captured orbits
$M_{\rm s,start} = 3 \times 10^{23}$ g	Resonances of the inner three satellites	Long-lived prograde captured orbits Critical mass of pebble accretion's start
$x = 0.0026$	Mass of all the satellites	A small amount of dust-supply
$t_{\rm gap} = 1.0$ Myr	Melted/unmelted Ganymede & Callisto	Early formation of Jupiter
$t_{\rm cap} = 1.0, 1.25, 1.5, 2.0$ Myr	Melted/unmelted Ganymede & Callisto	-

the CJD so that the inner cavity also opens around Jupiter by its magnetic field (see Methods). The position of the edge of the cavity can be estimated from the balance of the gas accretion rate and magnetic stress by Jupiter's magnetic field (Takata & Stevenson, 1996; Liu et al., 2017). It is plausible that Jupiter's magnetic field was stronger than the current one, resulting in magnetospheric accretion and opening of a cavity (Stevenson et al., 1983; Sánchez-Lavega, 2004; Christensen et al., 2009). In our model, we fix the position of the cavity at Io's position ($r_{\rm cav} = 5.89\ R_{\rm J}$). This should move outward as the gas accretion rate decreases but stop at the corotation radius. It is considered that Jupiter was larger than today (Burrows et al., 1997; Fortney et al., 2011) and so the corotation radius was wider than the current, $r_{\rm co} = 2.25\ R_{\rm J}$. See also Section 3.5.2.

We also assume that the strength of turbulence of the viscous accretion disk is $\alpha = 10^{-4}$, consistent with the inability of the MRI to operate in the CJD (Fujii et al., 2014). From the assumptions of the strength of turbulence and the gas accretion rate, we calculate the gas surface density of the disk. The surface density affects many properties of the system, for example, the disk temperature, the pebble accretion rates, and the migration speeds.

To get the disk thermal condition suitable for reproducing the ice mass fractions of the satellites, we assume that $r_{\rm sdg}$, the ratio of the surface densities of the small dust particles which affect the temperature and the gas is $r_{\rm sdg} = 1.7 \times 10^{-7}$, which renders the Rosseland mean optical depth τ about unity at Ganymede's orbit, 15 $R_{\rm J}$. This value of $r_{\rm sdg}$ implies that there is only a tiny quantity of dust present. However, previous work argued that a laminar viscous accretion disk can keep the midplane temperature cold even if the optical depth is larger than unity because the accretion energy dissipates at the high altitude of the disk and is lost due to magnetically driven disk wind (Hirose et al., 2009; Mori et al., in prep.). Under these conditions, our model will also work with higher $r_{\rm sdg}$. See also Section 3.5.3.

One of the strong points compared with previous scenarios is that our slow-pebble-accretion scenario only needs a small amount of solid material (i.e. planetesimals and dust particles). Actually, only four planetesimals need to be captured by the CJD. This assumption is consistent with the following facts: after the gap opens in the CSD, such captures only appear for the planetesimals which have high eccentricities in the CSD (Fujita

et al., 2013); planetesimals can form at the gas pressure maximum of the gap and those that are scattered by a large body will have high eccentricities (Kobayashi et al., 2012; Ronnet et al., 2018). Moreover, our assumptions of a starting location of $r_{\rm s,start} = 50\ R_{\rm J}$ with zero eccentricity are plausible. According to a previous work, there are orbits that planetesimals are captured by multiple approaches to Jupiter and become circularized around $\approx 50\ R_{\rm J}$ (long-lived prograde captured orbits) (Suetsugu et al., 2016). We also fix the mass of the captured planetesimals as 3×10^{23}g (about 300 km), which is consistent for the properties of the captured orbits (Suetsugu et al., 2016). These planetesimals are large enough to start growing by efficient pebble accretion (i.e. in the settling regime) for the adopted disk properties (Ormel, 2017). Smaller planetesimals, on the other hand, will stay small and may be scattered or accreted by large ones. In the settling regime, any difference in the initial mass does not change the final mass because the growth timescale increase with mass. In addition, planetesimals smaller than the assumed value, are likely to end up in higher order resonances (i.e. 3:2 instead 2:1), by virtue of their faster migration. Therefore, the initial seed mass must be similar or larger than our standard value. See also Section 3.5.4 for further discussion.

Furthermore, the total amount of dust needed to drive the growth in the slow-pebble-accretion scenario is also modest. Our scenario can reproduce the mass of the current Galilean satellites even with the dust-to-gas accretion ratio is as low as $x = 0.0026$, which is smaller than the solar composition. by a factor of four. This is consistent with the fact that the gas flowing into the CJD is depleted in solids (Canup & Ward, 2002; Tanigawa et al., 2012). Because of the gap formation in the CJD caused by Jupiter, only small particles can overcome the ensuing gas pressure gradient to end up in the CJD (Zhu et al., 2012), In addition, the accreted gas should be supplied from high altitude where gravitational settling of larger particles limits the amounts of dust (Tanigawa et al., 2012).

In this scenario, Jupiter should have also grown so large that the gap structure opens and the pebbles can be trapped at the gas pressure maximum around Jupiter around 1 Myr after the formation of the calcium-aluminum-rich inclusions (CAIs) to make the dichotomy of the internal structures of Ganymede and Callisto by ^{26}Al heat. This is consistent with

a resent "early Jupiter formation" scenario showing that solid materials in the solar system were spatially separated by that time (Kruijer et al., 2017). Each capture time of the planetesimals $t_{\rm cap}$ are also assumed to make the dichotomy.

Callisto is captured into a 2:1 resonance with Ganymede and it is difficult to form Callisto without a capture in a resonance by our simple calculations. However, present-day Callisto is not in any resonance with Ganymede, requiring an escape from the resonance. More detailed studies of the orbital evolutions of the two satellites will be needed.

3.5 Discussions

3.5.1 Formation of Undifferentiated Callisto

Callisto is minimally or only modestly differentiated but the other Galilean satellites are fully differentiated. It is difficult to make the dichotomy between the internal structures of Ganymede and Callisto by the difference in the heat of accretion or ^{26}Al decay in the previous Canup-Ward formation scenario (Canup & Ward, 2006; Barr & Canup, 2008). In our slow-pebble-accretion scenario, we found that only Ganymede melted by ^{26}Al heat if its seed was captured by the disk later enough.

Figure 3.7 represents the internal temperature of Callisto where its seed is captured at different timing. We fix the position of Callisto at the current orbit in this calculation. Without the ^{26}Al heat, the surface of Callisto keeps its temperature the same as the surrounding gas disk. This means that the pebble accretion heating can not differentiate the satellite. The settling velocity is $\approx 3 \times 10^5$ ms^{-1} and this is faster than the escape velocity $\approx 1 \times 10^5$ m s^{-1} (see Section 3.2.5). This means that the aerobraking does not work on pebbles and the collisional speed of pebbles to the surface of Callisto is actually the escape velocity. In this case, the collisional velocities are the same in both the classical satellitesimal-accretion and our slow-pebble-accretion scenarios. The difference between the two scenarios is the formation timescale. The formation of the Galilean satellites takes about 10 Myr in our scenario and this is much longer than the melting critical accretion timescale, 0.6 Myr (Barr & Canup, 2008).

Only in the cases where ^{26}Al radiogenic heating is considered, the internal temperature

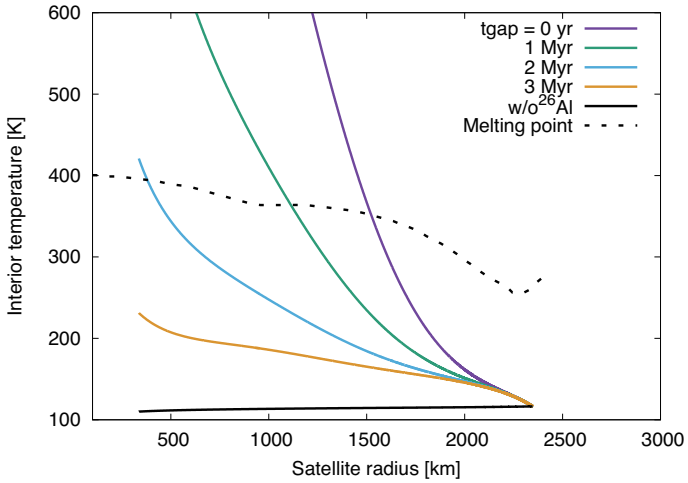

Figure 3.7: **Internal temperature of satellites.** The color variations represent the difference in the gap opening time, in other words, the time that the pebble accretion starts. The black solid curve represents the internal temperature without ^{26}Al heat (only accretion heat). The dotted black curve is the melting point of Callisto (Barr & Canup, 2008). We put seeds of satellites on 26.3 $R_{\rm J}$ (the current orbit of Callisto) at $t = 0, 1, 2, 3$ Myr with the initial mass of $M_{\rm s,start} = 3 \times 10^{23}$ g and fix their positions in this calculation. The dust-to-gas accretion ratio is $x = 0.0021$.

becomes larger than the melting point. Figure 3.7 shows that this condition is achieved if most of the ^{26}Al in the material of Callisto has decayed before its formation starts, in other words, $t_{\rm gap} (= t_{\rm cap}) > 2$ Myr. Also, if Ganymede starts to form by 1.5 Myr after the formation of CAIs and Callisto starts later than 2.0 Myr, the dichotomy between the two satellites should be explained.

3.5.2 Inner Cavity and Position of Io

In this work, we have fixed the position of the disk inner edge as the current orbit of Io, 5.89 $R_{\rm J}$, for simplicity. In this section, we actually explain that this assumption is plausible. However, Equation 3.3 shows the position is determined by the balance between the two stresses of Jupiter's dipole magnetic field and gas accretion. Therefore, as the gas accretion rate $\dot{M}_{\rm g}$ decreases, the inner edge moves outward and the innermost seed (Io) may also migrates together. The two-sided (i.e. normal Type I migration) torque that a satellites

receives is,

$$\Gamma_{2s} = \frac{1}{2} M_s v_K v_{t1}. \tag{3.29}$$

On the other hand, a satellite at the disk edge receives a strong one-sided positive corotation torque that pushes the satellite outward (Liu et al., 2017). The one-sided corotation and Lindblad torque is,

$$\Gamma_{1s,co} = 2.46 \left(\frac{\Sigma_g r^2}{M_{cp}} \right) \left(\frac{\mu_s}{h_g^3} \right)^{1/2} M_s (r\Omega_K)^2, \tag{3.30}$$

and

$$\Gamma_{1s,Lin} = -0.65 \left(\frac{\Sigma_g r^2}{M_{cp}} \right) \frac{\mu_s}{h_g^3} M_s (r\Omega_K)^2, \tag{3.31}$$

respectively (Liu et al., 2017). Figure 3.8 shows that the one-sided corotation torque Io (Seed1) receives is much larger than the negative one-sided Lindblad torque and the negative two-sided torque of that the other satellites (Seed2, 3, and 4) receive, respectively. Since the sum of the negative torque is smaller than the positive torque, even if the other satellites push Io through the chain of the resonance, Io keeps its position on the edge of the cavity. It is also argued that if the migration timescale of the edge (i.e. $3.5 t_{dep}$) is shorter than that of the migration of the satellite by the one-sided corotation torque, the disk edge leaves the satellite there (Liu et al., 2017). We found that, however, the timescale of Io's migration by the one-sided corotation torque is $\sim 10^3$ year and this is much shorter than the migration timescale of the edge, $\sim 10^6$ year. Therefore, Io may have moved much further than its current orbit with the disk inner edge moves outward.

However, this outward migration of the inner edge should stop at the corotation radius r_{co} where the Keplerian frequency of the disk equals to the spin frequency of Jupiter. When $r_{cav} > r_{co}$, there will be two possibilities; the angular momentum will be transferred from Jupiter to the disk and then the gas accretion will stop, or otherwise the corotation radius and the disk edge will move outward together and then the accretion will continue (Takata & Stevenson, 1996; Liu et al., 2017). Although the current corotation radius is $r_{co} \approx 2.25\ R_J$, it is considered that the radius of Jupiter was larger than that of today (Burrows et al., 1997; Fortney et al., 2011), and this means that the corotation radius was also

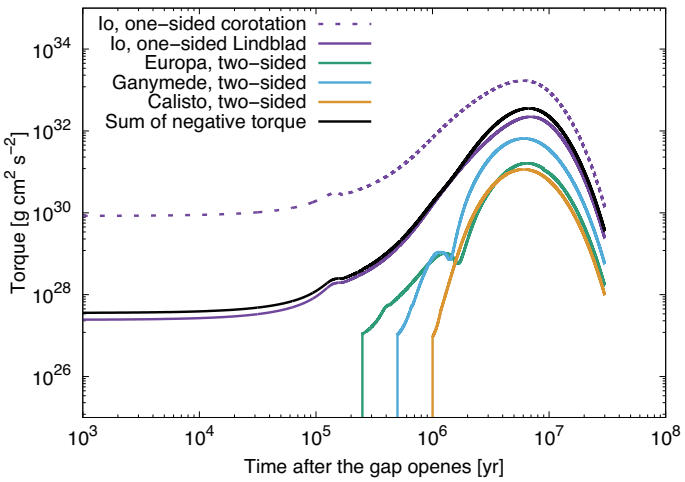

Figure 3.8: **Torque which the satellites receive.** The solid and dashed purple curves are the Lindblad and corotation one-sided torque that Io (Seed1) receives, respectively. The green, light blue, and orange solid curves are the two-sided torque of Europa, Ganymede, and Callisto, respectively. The black curve is the sum of the negative torque; the Lindblad one-sided torque of Io and the two-sided torque of the other three satellites.

larger than the current one if the conservation of the angular momentum of Jupiter is assumed. Considering the transport of the angular momentum from Jupiter to the disk, the angular momentum should have been conserved since the disk disappeared. According to a formation model of Jupiter, the radius of the planet was $\approx 1.75\ R_{\rm J}$ after its rapid gas accretion and it decreased little by little (Lissauer et al., 2009). When the radius of Jupiter is $1.75\ R_{\rm J}$, the corotation radius should be $r_{\rm co} \approx 4.7\ R_{\rm J}$. We have then considered two scenarios of Io formation. The first one is that Io formed around $r \approx 4.7\ R_{\rm J}$, slightly interior to the $r = 5.89\ R_{\rm J}$ of our fiducial model, and then moved outward after the disk dissipated. The satellites, especially the inner ones, could move outward by the tidal force from Jupiter (Yoder & Peale, 1981). The outer ones would be pushed by the inner ones and move outward with them because of the resonance. In this case, the position of the snowline should have been more inside than the fiducial case in this work but this thermal condition could easily be reproduced by another parameter set. The second possibility is that Io was not the innermost one. If a body was present at $r = 3.7\ R_{\rm J}$, Io would have been situated at $r = 5.7\ R_{\rm J}$ if they were trapped in a 2:1 resonance. This orbit is consistent

with that the corotation radius when the radius of Jupiter is $\approx 1.5\ R_{\rm J}$ and this radius can be achieved during the contraction of Jupiter. The innermost body may have been broken by the tidal force of Jupiter when it has entered inside the Roche limit. Current Io, trapped in the Laplace resonance, actually moves inward little by little because of the tidal dissipation and the innermost body may have also experienced such inward migration (Lainey et al., 2009).

The ionization degree of the disk inner region, $\chi_{\rm e} \equiv n_{\rm e}/n_{\rm n}$, where $n_{\rm e}$ and $n_{\rm n}$ are respectively number density of electron and neutral gas, is also important. Without enough ionization, the disk gas can not couple with the rotating magnetic field of Jupiter and the inner cavity does not open. The angular momentum transfer can be occurred if the magnetic Reynolds number[9] $R_{\rm m} \equiv VH_{\rm g}/\lambda > 1$, where V is the relative velocity between the rotating magnetic field and the disk gas, and λ is the magnetic diffusivity (Takata & Stevenson, 1996). If Jupiter and its magnetic field spin rigidly at the current speed, $V \approx 3\times10^4$ m s^{-1}, $H_{\rm g} \approx 1.1\times10^7$ m, and $\lambda \approx 0.74/\chi_{\rm e}$ at $r = 1\ R_{\rm J}$ with the disk temperature is $T = 1000$ K (Blaes & Balbus, 1994). The condition for angular momentum transport is then $\chi_{\rm e} \gtrsim 10^{-12} - 10^{-11}$. Takata & Stevenson (1996) estimated the ionization degree of the circum-Jovian disk including the effects of galactic cosmic rays and radioactive isotope decay and so on. They assumed the minimum mass disk model by Lunine & Stevenson (1982), whose gas surface density is 100 times larger than that of our model, and argued that the ionization degree is $\chi_{\rm e} \lesssim 10^{-16}$ at the midplane, $\chi_{\rm e} \sim 10^{-15}$ at the altitude of one scale height, and $\chi_{\rm e} \sim 10^{-13} - 10^{12}$ at three scale heights. If the ionization degree is inversely proportional to the gas surface density, although it is a very rough estimate, the ionization degree in our disk model should be $\chi_{\rm e} \lesssim 10^{-14}$ at the midplane, $\chi_{\rm e} \sim 10^{-13}$ at the altitude of one scale height, and $\chi_{\rm e} \sim 10^{-11} - 10^{-10}$ at three scale heights. Therefore, the condition for angular momentum transport will be achieved at the altitude higher than the scale height. A possible mechanism to curve the inner cavity of the gas disk is that the transport of angular momentum (i.e. the radial gas flow) is dominated in the upper region

[9]This magnetic Reynolds number is $\sim 10^3$ times larger than the Elsasser number, the critical number for the MRI activation.

and the quick vertical relaxation to hydrostatic conditions provides an accompanying vertical upward drift of gas (see Takata & Stevenson (1996)). However, this discussion is based on a very rough estimate, more detailed investigation of the disk inner region should be carried out in future.

3.5.3 Effects of the Thermal Condition of the Disk

We have assumed a thermal condition of the disk but actually the thermal condition can affect the formation of the satellites strongly. The disk temperature strongly depends on the quantities of small dust grains. Figure 3.9 represents the $r_{\rm sdg}$ dependences of the snowline, satellite mass, and ice fraction of satellites in the case of the fixed orbits. The top panel shows that when $r_{\rm sdg} = 1.7 \times 10^{-7}$, the assumption in this work, the snowline migrates inward from just inside Ganymede's orbit and stops just inside Europa's. This is because the first term is dominant in the opacity factor g in the first half of its evolution and then the second term becomes dominant as the gas surface density decreases (see Eq. (2.4)). If $r_{\rm sdg}$ is larger than this, the first term is dominant until the almost end, and vice versa. The middle panel shows that the mass distribution of the Galilean satellites can be reproduced only when $r_{\rm sdg} = 1.7 \times 10^{-7}$. However, if the gas accretion rate $\dot{M}_{\rm g}$ is smaller than this assumption and the dust-to-gas accretion rate ratio x is larger, the snowline will be at the Ganymede orbit and the mass distribution of the satellites will be reproduced. The bottom panel shows that the $r_{\rm sdg}$ dependence of the ice mass fraction is large. When $r_{\rm sdg}$ is larger than the most suitable case, the slope inside the first position of the snowline is gentler and the ice mass fraction of Europa is larger. On the other hand, when $r_{\rm sdg}$ is smaller, the slope is steeper and Europa can not get enough ice. These results can be understood by the top panel. Note that the gas opacity ($\sim 10^{-5}$ to 10^{-4} cm^2 g^{-1}) may be able to raise the disk temperature (Mizuno, 1980). On the other hand, previous work showed that if the midplane of the disk is laminar, the accretion energy dissipates at the high altitude of the disk and is lost due to magnetically driven disk wind. The midplane temperature determined by viscous heating can then be low even if the optical depth τ is larger than unity (Hirose et al., 2009; Mori et al., in prep.). It is argued that MRI does not occur in the CJD and there

is only a weak turbulence (Fujii et al., 2014) so the disk could be cold. This phenomenon is consistent with our assumption of the disk temperature.

3.5.4 Effects of the Initial Mass of the Seeds

We have assumed the initial mass of the seeds as 3×10^{23}g. In this section, we investigate the initial mass dependences. Basically, the final mass of satellites does not depend on the initial mass strongly because the growth timescale becomes larger as they grow (see the lower panel of Figure 3.4). Moreover, there are two effects that make the distribution of the initial mass narrow. First, the effective pebble accretion (in settling regime) only occurs when the seeds are heavier than $\sim 10^{23}$g around $r \approx 50\, R_{\rm J}$ (see Eq. (3.19)). Smaller captured planetesimals can not grow large and will be scattered or accreted by large ones. In addition, smaller planetesimals experience stronger aerodynamic drag, which allows them to cross 2:1 resonances (see Eq.(3.28) and Table 3.1). This is because the migration speed by aerodynamic drag is fast when the seeds are small (Eq. (3.25)). On the other hand, larger planetesimals are difficult to be captured–aerodynamic drag is not strong enough. These arguments limit the range in the initial seed mass, justifying our fiducial value of $M_{\rm s,start} = 3 \times 10^{23}$ g.

3.5.5 Subsequent Evolution of Ganymede's Internal Structure

We conclude that Ganymede's interior differentiates into the rocky core and the icy mantle because of the ^{26}Al heat in the accreted pebbles. However, strictly speaking, it can melt only the region of 1000 km from the center of Ganymede (see Figure 3.6). One possible heat source to melt the whole interior of the satellite is the potential energy released during the overturn of the pristine (undifferentiated) icy-rocky crust and the pure icy mantle by the Rayleigh-Taylor instability. Here, we consider a three-layered interior structure: (1) the pristine (undifferentiated) icy-rocky crust (0 – 1600 km deep), (2) the pure icy mantle (1600 – 2000 km deep), and (3) the rocky core (2000 – 2600 km deep), as the initial condition. We estimate the depth of the layers by assuming the density of the pure ice, rocky core, and pristine crust is $\rho_{\rm ice} = 1.4$ g cm^{-3}, $\rho_{\rm rock} = 3.0$ g cm^{-3} and $\rho_{\rm s} = 1.9$ g cm^{-3},

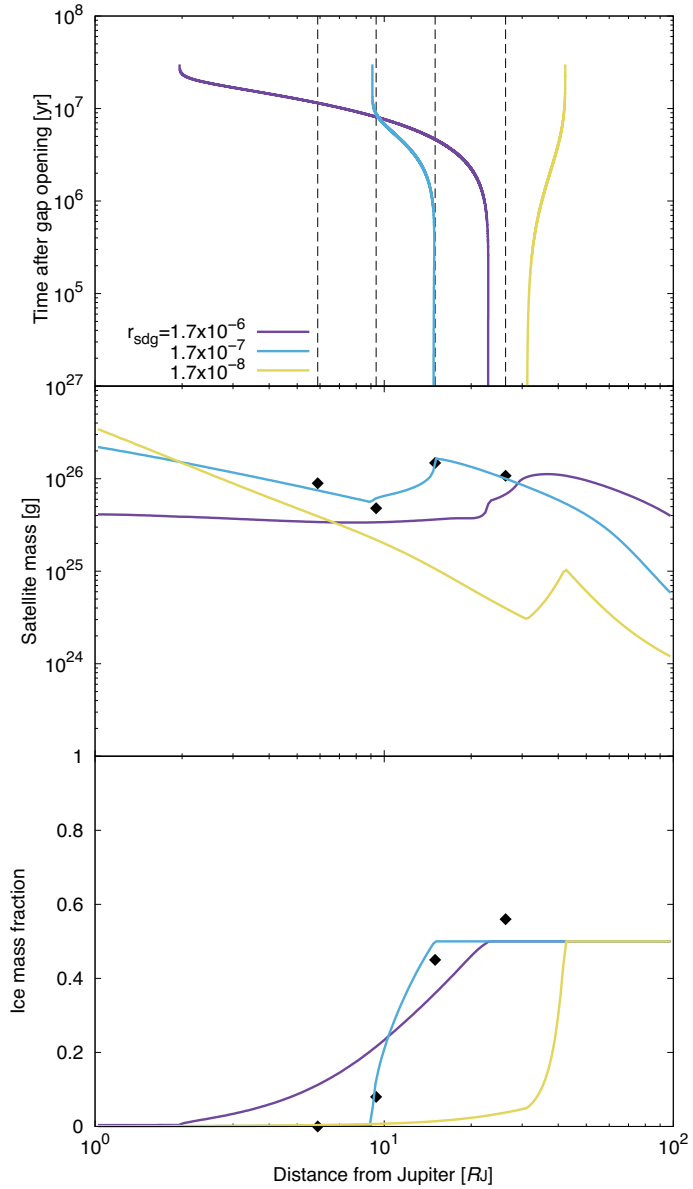

Figure 3.9: **Effects of the thermal condition of the disk.** The top, middle, and bottom panels represent the evolution of the snowline, the final satellite mass, and the final ice mass fractions of satellites, respectively. The color variations represent the difference in the small grain-to gas surface densities ratio. The black dashed lines and the black diamonds are the current properties of the Galilean satellites. We put seeds of satellites on 1 to 100 R_J with the initial mass of $M_{s,start} = 3 \times 10^{23}$ g and fix their positions in this calculation. The dust-to-gas accretion ratio is $x = 0.0021$.

respectively.

First, we check whether the Rayleigh-Taylor instability occurs or not. The condition depends on the viscosity of the upper layer, which is the pristine crust in this situation. if the viscosity is lower than the following critical value, the instability occurs with the timescale $t_{\rm RT}$ (Rubin et al., 2014),

$$\eta_{\rm crit} = \left[(n-1)^{1/n}\frac{C_{\rm L\Delta\rho}}{2n}\right]\left(\frac{Z_0}{L}\right)^{(n-1)/n}\Delta\rho g(R) L t_{\rm RT}, \tag{3.32}$$

where n, $C_{\rm L\Delta\rho}$, and Z_0 are the index of the stress related to the strain rate, a dimensionless quantity determined by the geometry and rheology, and the initial perturbation amplitude, respectively. We assume $n = 1.8$, $C_{\rm L\Delta\rho} = 0.76$, and $Z_0 = 1$ km (see Rubin et al. (2014)). The difference of the density is $\Delta\rho = \rho_{\rm s} - \rho_{\rm ice} = 500$ kg m^{-3} and $g_{\rm s}(R) = 0.54$ m s^{-1} is the gravitational field of satellite at R(= 1000 km), distance from the center. The lengthscale over which the viscosity varies significantly is

$$L = \frac{nRT_0}{E_{\rm a}}\frac{T_0}{|dT/dz|}, \tag{3.33}$$

where R, T_0, and $E_{\rm a}$ are the gas constant, the temperature of at the interface between the two layers, and the activation energy, respectively. We assume them as $T_0 = 370$ K and $E_{\rm a} = 49$ kJ mol^{-1} (see Figure 3.6 and Rubin et al. (2014)). According to Figure 3.6, the temperature gradient across the upper crust is $T_0/|dT/dz| = 0.14$ K km^{-1}. We can then calculate the critical viscosity, $\eta_{\rm crit} = 7.6\times10^{13}(t_{\rm RT}/{\rm year})$ [Pa s]. The viscosity of the upper layer should strongly depend on the temperature. According to the Arrhenius functions, the viscosity can be estimated by

$$\eta_{\rm ice} = \eta_{\rm ref}\exp\left[A\left(\frac{T_{\rm ref}}{T} - 1\right)\right], \tag{3.34}$$

where $\eta_{\rm ref}$, T, and $T_{\rm ref} = 273$ K are the reference viscosity, the temperature of the upper crust, and the reference temperature (melting point of pure ice), respectively. A constant coefficient A is about $20 - 25$ and the reference viscosity of pure ice I and pure ice V and VI, are $\eta_{\rm I} \sim 10^{14}$ [Pa s] and $\eta_{\rm V,VI} \sim 10^{16} - 10^{17}$ [Pa s] (Rubin et al., 2014; Shoji & Kurita, 2014). If the volume rate of rock is smaller than 75%, the viscosity of rock-mixed ice is

almost the same as that of pure ice (Durham et al., 2010). The minimum temperature of the upper crust is about 150 K (see Figure 3.6). If we substitute this temperature for Eq. (3.34), the timescale of the R-T instability is $10^9 - 10^{10}$ year for $A = 20$ and $10^{11} - 10^{12}$ year for $A = 25$. However, if we substitute $T = 170$ K, only 20 K larger, the timescale becomes $10 - 100$ times shorter. Therefore, if the upper crust was heated up 20 K by long-lived radiogenic heating or the released gravitational energy of halfway R-T instability itself (see next paragraph), R-T instability has been able to occur by today in the upper crust of Ganymede. One interesting observational fact of Ganymede is that there are two regions on the surface of the satellite: very primitive region ($\sim$ 4 Ga) and relatively newer region ($\sim$ 2 Ga). This characteristic is consistent with our estimate of the evolution of Ganymede's interior; the newer surface had been the inner pure icy mantle and was transported to the surface by the R-T instability around 2 Ga. On the other hand, Callisto's interior did not melt and the surface has been kept as a primitive crust.

Second, we estimate the heat released by the R-T instability and how much the internal temperature rises. If the pure ice mantle (consistent with the half mass of the differentiated region, $M_{\rm ice}(= M_{\rm rock}) = 4 \times 10^{21}$ kg) is lifted up to the surface of the satellite, the thickness of the pure ice crust will be $h_{\rm ice} = 120$ km. The mass of the pure ice (and rock) is much smaller than the whole mass of Ganymede ($M_{\rm G}$), the increase of the temperature of the undifferentiated pristine crust uniformly heated up by the released potential energy ($\Delta Q_{\rm RT}$) can be roughly estimated by the following equations,

$$\begin{aligned}\Delta T_{\rm RT} =& \frac{\Delta Q_{\rm RT}}{C_{\rm p} M_{\rm G}} \\ \approx& \frac{G M_{\rm ice}}{C_{\rm p}(R_{\rm G} - h_{\rm ice})} \left(\frac{\rho_{\rm s}}{\rho_{\rm ice}} - 1\right)\left(1 - \frac{R_{\rm rock}^2 \rho_{\rm rock}}{(R_{\rm G} - h_{\rm ice})^2 \rho_{\rm s}}\right) \\ \approx& 20 \text{ [K]},\end{aligned} \tag{3.35}$$

where $R_{\rm G}$ is the radius of Ganymede. This temperature increase is, unfortunately, not enough for the whole differentiation of the interior of the satellite. To melt the whole region, about 100 K increase of the temperature would be needed (see Figure 3.6). However, we neglect the two kinds of heat provided by (1) the released potential energy during the

Table 3.5: Variables in Chapter 3

	Equation	Description
t	-	Time after the formation of CAIs
r	-	Distance from Jupiter
$M_{\rm in}$	-	Mass of the inner satellite
$M_{\rm out}$	-	Mass of the outer satellite
$T_{\rm in}$	-	Orbital period of the inner satellite
$B_{\rm cp}$	-	Strength of the magnetic field of the central star
$\Omega_{\rm K}$	$\sqrt{GM_{\rm cp}/r^3}$	Kepler angular velocity (G: Gravitational constant)
$c_{\rm s}$	$\sqrt{k_{\rm B}T_{\rm d}/m_{\rm g}}$	Sound speed ($k_{\rm B}$: Boltzmann constant)
τ	$\kappa\Sigma_{\rm g}$	Rosseland mean optical depth
$v_{\rm K}$	$r\Omega_{\rm K}$	Kepler velocity
p	$\Sigma_{\rm g} \propto r^{-p}$	r exponent of the gas surface density
q	$T_{\rm d} \propto r^{-q}$	r exponent of the temperature
$\mu_{\rm s}$	$M_{\rm s}/M_{\rm cp}$	Satellite-to-central planet mass ratio
$h_{\rm p}$	$H_{\rm p}/r$	Pebble aspect ratio
$H_{\rm g}$	$c_{\rm s}/\Omega_{\rm K}$	Gas scale hight
$t_{\rm grow}$	$M_{\rm s}/(dM_{\rm s}/dt)$	Growth timescale
$h_{\rm g}$	$H_{\rm g}/r$	Gas aspect ratio
$v_{\rm esc}$	$\sqrt{2GM_{\rm s}/R_{\rm s}}$	Escape velocity
$v_{\rm set}$	$g_{\rm s}t_{\rm stop}$	Settling velocity, Terminal velocity
$g_{\rm s}$	$GM_{\rm s}/R_{\rm s}^2$	Gravitational field of satellite
$\rho_{\rm g}$	$\Sigma_{\rm g}/(\sqrt{2\pi}H_{\rm g})$	Local gas space density
$t_{\rm stop}$	$\mathrm{St}_{\rm p}/\Omega_{\rm K}$	Stopping time of pebbles
$t_{\rm mig}$	$r/\lvert v_{\rm gd} + v_{\rm t1}\rvert$	Migration timescale

differentiation of the region of 1000 km from the center and (2) the central captured planetesimal which has been heated up by ^{26}Al decay (Wakita & Sekiya, 2011). Such heat may be transported with the lifting up pure icy mantle and so be able to contribute to differentiate the region remaining unmelted.

3.6 Appendix

3.6.1 Variables in Chapter 3

We use many variables in Chapter 3. We then summarize them in Table 3.5 and 3.6.

Table 3.6: Variables in Chapter 3

	Equation	Description
$M_{\rm s}$	Eq. (3.1)	Satellite mass
$\dot{M}_{\rm g}$	Eq. (3.2)	Gas accretion rate
$r_{\rm cav}$	Eq. (3.3)	Size of the magnetospheric cavity
$\Sigma_{\rm g}$	Eq. (3.4)	Gas surface density
$T_{\rm d}$	Eq. (3.5)	Disk midplane temperature
g	Eq. (3.6)	Opacity factor
κ	Eq. (3.7)	Rosseland mean opacity
$\dot{M}_{\rm p}$	Eq. (3.8)	Pebble mass flux
${\rm St}_{\rm p}$	Eq. (3.9)	Stokes number of pebbles (determined by drift)
$v_{\rm pp}$	Eq. (3.10)	Pebble-to-pebble relative velocity
$v_{\rm r}$	Eq. (3.11)	Drift velocity of pebbles
$v_{\rm t}$	Eq. (3.12)	Relative velocity of pebbles driven by turbulence
${\rm St}_{\rm p}$	Eq. (3.13)	Stokes number of pebbles (determined by fragmentation)
$\dot{M}_{\rm p}$	Eq. (3.14)	Pebble mass flux
$P_{\rm eff}$	Eq. (3.15)	Pebble accretion efficiency
$H_{\rm p}$	Eq. (3.16)	Pebble scale height
Δv	Eq. (3.17)	Pebble-satellite relative velocity
$\dot{M}_{\rm p,in}$	Eq. (3.18)	Pebble mass flux inside a satellite
M_*	Eq. (3.19)	Satellite mass that the effective pebble accretion starts
$M_{\rm iso}$	Eq. (3.20)	Pebble isolation mass
$T_{\rm s}$	Eq. (3.21)	Temperature of the satellite surface
$u_{\rm i}$	Eq. (3.22)	Pebble-satellite collision velocity
$\Delta T_{\rm fin}$	Eq. (3.23)	The increase in the satellite internal temperature
$T_{\rm fin}$	Eq. (3.24)	The final satellite internal temperature
$v_{\rm gd}$	Eq. (3.25)	Aerodynamic drag migration velocity
${\rm St}_{\rm s}$	Eq. (3.26)	Stokes number of satellites
$v_{\rm mig}$	Eq. (3.27)	Type I migration velocity
$t_{\rm crit}$	Eq. (3.28)	Critical migration timescale for resonance capture
$b_{\rm t1}$	*	Migration constant
$\Gamma_{\rm 2s}$	Eq. (3.29)	Two-sided torque
$\Gamma_{\rm 1s,co}$	Eq. (3.30)	One-sided corotation torque
$\Gamma_{\rm 1s,Lin}$	Eq. (3.31)	One-sided Lindblad torque

* Eq. (10) of Ogihara et al. (2015)

Chapter 4 Conclusions

We have investigated the formation of the satellites around gas planets, in particular, Jupiter. In this thesis, we studied mainly two phases of satellite formation: (1) satellitesimal formation by collisional dust growth; and (2) the Galilean satellites formation by pebble accretion. Here, we summarize our work and conclude the thesis by showing the remaining issues and future work.

4.1 Difficulties in Formation of Satellitesimals

In Chapter 2, we investigated whether icy dust particles can form satellitesimals by their pairwise collisional growth in circumplanetary disks with various conditions. We have calculated the distributions of the surface density, radius and Stokes number (stopping time normalized by the Kepler-time) of the peak mass dust particles. Our model considered only steady conditions and assumed that the temperature of the circumplanetary disk is almost like a minimum estimate. We have changed the dust and gas inflow mass fluxes and the strength of turbulence in the disk so that we understood the effects of these factors to satellitesimal formation. We have also approximated the Stokes number analytically to understand these effects.

From the parameter studies, we have revealed the conditions for satellitesimal formation. The conditions are $\dot{M}_{\rm d}/\dot{M}_{\rm g} \geq 1$ and $10^{-4} \leq \alpha < 10^{-2}$ and the results do not depend on the gas accretion rate (Figure 2.6). The valance between the growth and drift timescale determines the evolution of the particles. The dust inflow mass flux is larger, the dust surface density in the disk is higher, increasing the collision rate and the making the growth timescale short. On the other hand, the gas mass flux is smaller, the gas surface density in the disk is lower, reducing the gas drag and making the drift timescale longer. Strong turbulence also reduces the gas surface density and makes the satellitesimals formation easy.

However, if the turbulence is too strong ($\alpha \geq 10^{-2}$), fragmentation occurs and satellitesimals do not form. The former condition, $\dot{M}_{\rm d}/\dot{M}_{\rm g} \geq 1$, would be difficult to achieve. This is because the dust particles must be prevented by the positive pressure bump at the outer edge of the gas gap structure to penetrate into the gap and the inflow gas from inside the gap will be dust depleted (See Sections 1.4.1 and 2.4.1). Our results also show that the porosity of dust particles does not affect the condition for satellitesimal formation (Section 2.4.2). The Stokes number does not depend on its internal density in Newton regime where the Stokes number takes the largest value (Equation (2.15)). Satellitesimal formation via streaming instability is also unfeasible because the dust-to-gas surface density ratio $\Sigma_{\rm d}/\Sigma_{\rm g}$ is much smaller than the critical value that the instability occurs (Section 2.4.3). On the other hand, there remains possibilities that satellitesimals form in CPDs by avoiding the vertical diffusion of the dust particles from the mid-plain and increasing the collision rate thanks to considering the difference between the α of diffusion (turbulence) and of disk accretion coefficient (Section 2.4.5). The photoevaporation may also contribute to satisfy the condition for satellitesimal formation by increasing the dust-to-gas ratio of the inflow gas in the final phase of planet formation (Section 2.4.1).

4.2 A New Scenario for the Origin of the Galilean Satellites

In Chapter 3, we built a new alternative formation scenario especially for the Galilean system using the pebbles not growing to satellitesimals but drifting toward Jupiter. As the seeds of the four satellites, we assume that four planetesimals are captured at given timing. We first calculate the evolution of the CJD, a gas accretion disk, which is determined by the given gas inflow mass flux reducing exponentially, and the fixed strength of turbulent viscosity. We then calculate 1-D (radial distribution) representative-size evolution of the pebbles including their collisional growth, aerodynamic drag, fragmentation and the distinction of icy/rocky pebbles by the position of snowline. Finally, the growth by accretion of the pebbles and 1-D radial orbital evolution of the seeds including aerodynamic drag, Type I migration, and simple checks of resonance capture are calculated. We simultaneously calculate their internal thermal evolution by pebble accretion and ^{26}Al decay heating,

and the pebble filtering effects by outer satellite seeds.

In contrast to the previous scenarios which only explain a part of the characteristics of the Galilean system or are inconsistent among the scenarios themselves in part, we found that our new scenario can reproduce the following characteristics simultaneously and consistently. First, it can reproduce the mass distribution of all the Galilean satellites even in the case of a very small amount of material supply to the CJD. Second, Io, Europa, and Ganymede are captured into 2:1 resonances one by one because the inner cavity opens by the strong magnetic field of Jupiter and halts the migration of Io at the edge of the cavity. Third, Europa accretes small quantities of icy particles in the final phase of its formation because the snowline moves inward as the gas accretion rate onto the CJD decreases. Therefore, Europa's rocky core and icy mantle are explained naturally. The ice mass fractions of the three other satellites are also reproduced because their orbits are inside, respectively outside, the snowline. Finally, our model explains why only Callisto stays undifferentiated and why the other satellites melt by radiogenic heating of ^{26}Al decay. The difference in the capture time of the planetesimals affects the total ^{26}Al heat they got and their internal structures but not their final mass because of their slow growth.

4.3 Satellitesimals or Pebbles?

In Chapter 2, we found that the dust particles do not grow to satellitesimals but drift toward Jupiter. However, we used smooth and steady disk models and neglected their detailed structures or evolution. Therefore, some special conditions may make satellitesimal formation possible, for example, a weak vertical diffusion and effective transport of gas angular momentum, an increase of dust-to-gas accretion rate in the final phase of planet formation, or gathering dust particles by gas outflow predicted by detailed hydrodynamical simulations (Drażkowska & Szulágyi, 2018). Moreover, the growth of Saturn may excite nearby planetesimals and make them be captured by the disk (Ronnet et al., 2018). Therefore, it can be considered that such special conditions raise episodic or local satellitesimal formation. In this case, not only pebble but also satellitesimal accretion can contribute to satellites formation unlike the discussion in Chapter 3. Moreover, satellitesimals originate from such

in-situ situations may also work as the seeds of the satellites, which subsequently accrete the drifting pebbles. This discussion is actually very similar to that of the recent scenarios for hybrid planetesimal-pebble accretion in planet formation (e.g. Alibert et al., 2018). The increase of solid material as planetesimals will help the growth of satellites but, on the other hand, it may become difficult to reproduce the properties of the Galilean system like the classical satellitesimal-accretion scenarios (see Section 1.3). In planet formation, the difference of the size of accreting solid material changes the planet's subsequent evolution, such as evolution of the gas envelope. It suggests that the difference of size also affects satellite formation such as Titan formation, which has a dense atmosphere. Moreover, it will affect the host gas planet formation itself (see also Section 4.5.3). Fortunately, we will be able to include satellitesimal accretion in our simulations. We should investigate the satellite formation with both satellitesimals and pebbles as a next step.

4.4 Suggestions for Exploration Missions

One possibility to find out which scenario is dominant, our new "slow-pebble-accretion" scenario or classical quick satellitesimal-accretion scenarios, is a measurement of D/H ratio in H_2O ice of Ganymede and Callisto. A new exploration mission for Jupiter and the Galilean satellites, JUICE (JUpiter ICy moons Explorer, ESA), will measure the D/H ratio of H_2O vapor in the thin atmospheres on the satellites by SWI (Submillimetre Wave Instrument). Here, we discuss the D/H ratio in H_2O ice of the satellites predicted by the two kinds of the scenarios.

In the case of our new scenario, the ratio should be $\sim 10^{-4} - 10^{-3}$, ten times or more larger than that of the protosolar value. This is because the icy material of the satellites never experiences evaporation after condensing in the outer region of the protoplanetary disk ($\gtrapprox 30$ au), where the predicted D/H ratio in H_2O ice is $\sim 10^{-4} - 10^{-3}$ and long-period comets with the similar value of D/H ratio form (e.g. Furuya et al., 2013; Altwegg et al., 2015). In our scenario, as we showed in Figure 1.5 in Section 1.4.1, the icy material originates in the outer region as icy pebbles and drifts to the Jovian orbit (e.g. Sato et al., 2016).

The pebbles then trap at the gas pressure maximum of the gas gap and form icy planetesimals and fragments Kobayashi et al. (2012); Taki et al. (2016). Some of the fragments coupled with gas can penetrate into the gap and flow into the circum-Jovian disk (Zhu et al., 2012). They form icy pebbles again and are finally accreted by the captured planetesimals and constitute the satellites. Even during the icy material accumulation, the surface temperature of the satellites should not be high enough to cause evaporation of water and so the D/H ratio of the material should be kept (see also Section 3.5.5).

On the other hand, in the classical scenarios, the D/H ratio should be lower than that in the "slow-pebble-accretion" scenario. The surface of the satellites, especially Ganymede should be melted by accretion heating and ocean would form (Barr & Canup, 2008). If the water vapor from the ocean stays around the surface, in other words, if the satellites can have their atmospheres, the deuterium exchange between the hydrogen gas and the water vapor may be able to increase the D/H ratio of the ocean about two times larger than that of the original accreted icy material (Genda & Ikoma, 2008). If mass fractionation during atmospheric hydrogen loss occurs, the ratio increases several times more. However, such an increase of the D/H ratio can occur only if the most amount of the water is exchanged with the vapor atmosphere. Moreover, if the atmosphere is continuously recycled with the CJD gas, the D/H ratio of the ocean should be only two times larger than that of the hydrogen of the CJD gas with the plotosolar D/H value at most (Horner et al., 2008). We note that if the icy material condenses at the jovian orbit or inside the CJD, the D/H ratio should be about $4 - 5$ times larger than that of the plotosolar value or the same with it, respectively, in the cases that the atmospheres do not form (Horner et al., 2008). Therefore, the D/H ratio may be kept lower than that in the "slow-pebble-accretion" scenario. Further studies of the primordial atmospheres (and the current thin atmospheres) of the satellites including the relations to the surfaces is necessary for more detail discussion.

Comparison of the D/H ratios between Ganymede and Callisto may also contribute to make sure which scenario is correct. In the case of the "slow-pebble-accretion" scenario, the D/H ratio of the two satellites should be the same because both of the ratios keep their original value. On the other hand, in the classical scenarios, if the dichotomy of the interiors

(differentiated/undifferentiated) of Ganymede and Callisto is from the accretion heating, the surface of Ganymede melts but that of Callisto does not. Therefore, the exchange of deuterium only occur on the surface of Ganymede and it should make some difference between the D/H ratios of the two satellites.

4.5 Future Work

We have already mentioned the importance of the studies which consider pebble- and satellitesimal- accretion simultaneously in the above section. Here, we show the other important future work in satellite formation research.

4.5.1 Orbital Calculations of Satellites

We are working on a 2-D orbital calculation of the satellites using a simulation code including MERCURY (Chambers, 1999) to check whether they are actually captured into resonance or not. In particular, the reason why current Callisto is not in any resonance is still unclear. We have already succeeded in developing a code by applying one of the latest simulation codes developed for planet formation (Brügger et al., 2018) to satellite formation. First, we modeled the circum-Jovian gas disk which is different from circum-stellar disks because of Jupiter's negligible radiation and a continuous supply of gas and solid materials. We then developed a code calculating the growth and drift of small solid particles in the disk (see Figure 4.1). This is the almost same with the simulations carried out in the previous sections but the size of the particles inside snowline is fixed as 0.1 cm. Finally, we calculated the growth of the satellites accreting the drifting solid particles and the 2-D orbital evolution of the satellites with the mutual gravitational interaction by modifying a previous N-body simulation code for planet systems. We have incorporated the above calculations into our new code and checked that the code works well. Figure 4.2 represents one of the test results of the orbital evolution of two satellites in the CJD. The satellites migrate toward Jupiter by gravitational interaction with the gas disk as they grow larger. They also interact with each other and are captured into 2:1 mean motion resonance like the actual orbits of Jovian satellites. We will use this code for future full-scale calculations

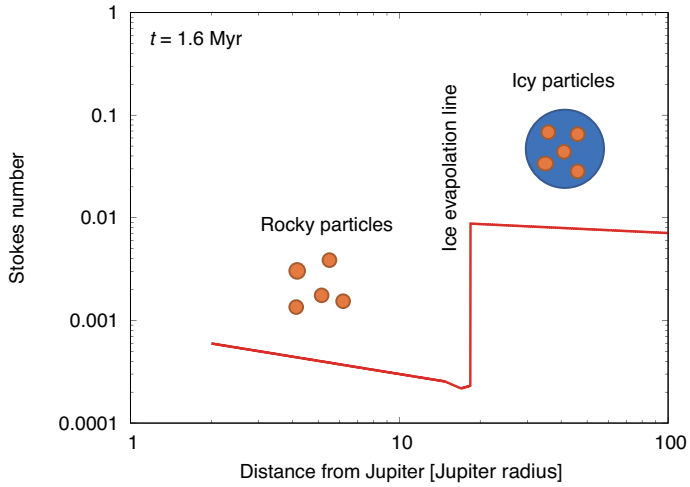

Figure 4.1: **Evolution of drifting solid particles.** The red solid curve is the Stokes number of the representative particles at each distance from Jupiter at $t = 1.6$ Myr. There is an evaporation line of icy particles around 15 Jupiter radius (R_J) and the size of the rocky particles inside the line is much smaller than outside. Schematic pictures of the rocky/icy particles are also shown.

that can reveal how the satellites form and get their current orbits. However, there remains two problems. First, the satellites migrate inward with $\sim$ 100 km size, which is about 10 times smaller than the real large satellites. Satellitesimals may be able to contribute to solve this problem (see the previous subsection). Second, it takes a long time to calculate the simulations because of the short orbital periods of the satellites (see Section 1.5). We will have to find a way to reduce the calculation time.

4.5.2 Saturnian Satellites Formation

Titan is considered to have formed in a CPD around Saturn and Iapetus may also have formed in the disk (Mosqueira & Estrada, 2003a; Canup & Ward, 2006; Sasaki et al., 2010). This is because the formation scenario where Saturnian satellites formed from ancient rings and migrated by tidal effects of Saturn can explain the origin of the mid-sized satellites nearby the planet but Titan and Iapetus are too far (Crida & Charnoz, 2012). However, the "slow-pebble-accretion" scenario where we built in Chapter 3 for the formation of the Jovian satellites will not be able to apply to the formation of the Saturnian satellites directly. In our scenario, the growth of satellites takes a long time but do not fall into the

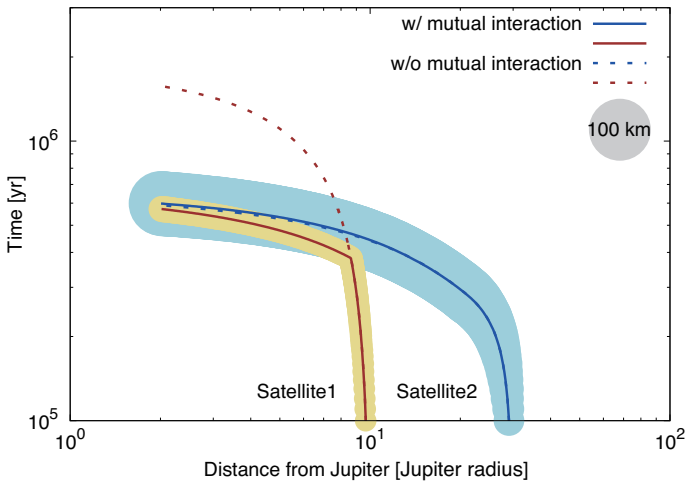

Figure 4.2: **Evolution of satellites in 2-D calculations.** The solid and dashed curves are the orbital evolution of the satellites with/without mutual gravitational interaction, respectively. The circles are the size of the satellites. Satellite2 grows faster than Satellite1 because there is an ice evaporation line between them and Satellite2 accretes not only rocky but also icy particles. Satellite2 then migrates faster and catches Satellite1 up. They are captured into 2:1 mean motion resonance because of the mutual gravitational interaction and Satellite2, heavier than Satellite1, pushes it toward Jupiter.

planet because the inner cavity stops their migration. In the case of Saturnian system, first, their current positions are too far from the central planet even for our scenario. On the other hand, Titan is considered to be incomplete differentiated (Iess et al., 2010), requiring that the satellite formed so slowly that accretion heating did not melt the interior. This is consistent with the "slow-pebble-accretion" scenario. The ways to achieve avoiding Titan's inward migration until the end of its long-timescale formation should be reducing the gas surface density of the disk (i.e. reducing the migration speed) and/or increasing the pebble mass flux (i.e. enhancing the accretion speed). Orbital expansion by outward Type I migration (see Eq. (3.27) in Section 3.2.6 and Eq. (10) of Ogihara et al. (2015)) or the outward migration of the inner edge of the gas disk (see Eq.(3.3) in Section 3.2.2) may be alternative ways to explain the current orbits of Titan and Iapetus.

On the other hand, discussion in Chapter 2 will be able to be applied to Saturnian satellites formation. We found that the most important factor dominating the evolution of dust particles is the dust-to-gas accretion rates ratio into CPDs, $\dot{M}_{\rm d}/\dot{M}_{\rm g}$. In other words, any

satellite system's formation could be discussed by changing this factor. In the case of Saturnian system, the gas gap around the CPD may be shallower than that of Jupiter because the planet mass is lighter. Therefore, the filtering effect by the pressure bump is weaker and so the dust-to-gas accretion ratio could be higher than that of Jupiter, suggesting satellitesimal formation easier. However, it should be noted that the dependency of aerodynamical drag changes within lower density gas (see Sections 2.2.2 and 2.5.1).

4.5.3 Formation of General Satellites and Gas Planets

It will also be important to investigate general satellite formation, in other words, exomoon formation in CPDs. We consider that it should be based on the recent understanding of gas planet formation. On the contrary, it will also be able to constrain gas planet formation from the characteristics of the satellites in our solar system and future observations of exomoons. One of the key points associating satellite formation with gas planet formation is supply of solid material to the planet's envelope through the satellite formation regions. As we showed in the previous sections, satellite formation in CPDs strongly depends on the amount of solid material in the disks because the more solids there are, the faster satellites grow. The size of the solid material also affects satellite formation processes of satellitesimal/pebble-accretion. At the same time, the amount of solid supply to the central planet's envelope strongly affects their gas accretion and evolution because the kinetic energy released from the accreted bodies supports the envelope (e.g. Ikoma et al., 2006). The size of the bodies is also important because small bodies like pebbles easily evaporate and enrich the envelope, accelerating the gas contraction (Venturini & Helled, 2017). Satellite formation processes (i.e. growth of material around planets) should also change the size and mass flux of the solids being accreted to the planets. Therefore, constraining how much and what kind of solid material are supplied to the envelope through the satellite formation regions is fundamentally important for both satellite and planet formation.

One strong reason why we should work on this research now is that recent studies have commenced to constrain the solid mass flux into gas planets during their formation. The formation of gas giants consists of three stages: core accretion ($M_{\rm p} \lessapprox 15\ M_{\oplus}$); slow gas

accretion($M_{\rm p} \lessapprox 50\ M_\oplus$); and rapid gas accretion. If their envelopes gravitationally collapse against the support by supply of solid material, the growth of planets will be accelerated and the stage will move from 2 to 3. If Stage 2 continues long, the planets migrate inward (Type I) during the stage and become Super-Earths, or otherwise the protoplanetary gas disk dissipates before the migration and Neptune analogs form Venturini & Helled (2017). In the case of Jupiter, Stage 2 should have continued 2 Myr (Kruijer et al., 2017) and a rate of at least $\sim 1\ M_\oplus\ {\rm yr}^{-1}$ in planetesimal accretion is required (Alibert et al., 2018). On the other hand, in Sage 3, Hot-Jupiters form after their migration (Type II) or Jupiter analogs form if the disk disappears before the migration. In the case of Jupiter, up to $\approx 25\ M_\oplus$ of solid material were accreted in Stage 3 (Alibert et al., 2018). We should investigate the satellite formation in both Stage 2 and 3 but, in particular, the latter will be challenging. This is because, in generally, CPDs do not form and envelopes maintain their forms during Stage 2, and satellite formation in pressure-supported envelops should be tough because the bodies will quickly fall into the cores in such gas structures. On the other hand, if the envelope is cold enough, the gas disk may form and satellites will grow in the disk (Wang et al., 2014; Szulágyi et al., 2018).

We should also try to predict the characteristics of the satellites formed around the planets plotted in a (distance from the central star) – $M_{\rm p}$ (planet mass) space (Figure 4.3). Population synthesis has been one of the effective ways to understand the evolution of planets and compare planet formation models with observations (e.g. Ida & Lin, 2004). In particular, one of the population synthesis models called "Bern model", can calculate the internal structures of the planets (e.g. Alibert et al., 2004). Therefore, we should use the model with satellite formation process that changes the size and mass flux of solid material supplied into the gas planets (Figure 4.3).

Finally, we should tray to predict the characteristics of the exomoons observed in future, in particular those of the planet-satellite systems at around 1 – 10au, by using a modified population synthesis model including the formation and loss of satellites (Figure 4.3). The telescopes CHEOPS and TESS (and PLATO), may be able to observe exomoons (Cabrera et al., 2018). The systems rotating around M type stars may be other suitable targets for the

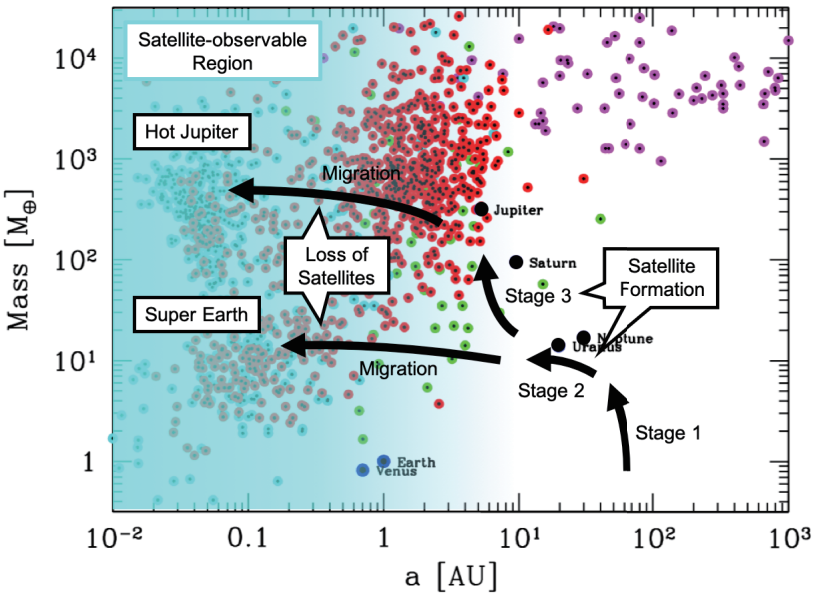

Figure 4.3: **Evolution tracks of gas planets and their satellites on the $a - M_{\rm p}$ diagram of confirmed exoplanets.** The red, cyan, magenta, and green points indicate planets detected by the radial velocity, transits, direct imaging, and microlensing, respectively. The planets of the solar system are also shown. The black arrows show the evolution tracks of gas planets. The cyan shaded region roughly shows the orbits of observable planet-satellite systems. This figure is modified from Fig. 1 of Mordasini (2018).

comparison between my theoretical predictions and future observations.

Bibliography

Adachi, I., Hayashi, C., & Nakazawa, K. 1976, Progress of Theoretical Physics, 56, 1756

Agnor, C. B., & Hamilton, D. P. 2006, Nature, 441, 192

Alexander, R. D., Clarke, C. J., & Pringle, J. E. 2006a, Monthly Notices of the Royal Astronomical Society, 369, 216

—. 2006b, Monthly Notices of the Royal Astronomical Society, 369, 229

Alibert, Y., Mordasini, C., & Benz, W. 2004, Astronomy & Astrophysics, 417, L25

Alibert, Y., Mousis, O., & Benz, W. 2005, Astronomy & Astrophysics, 439, 1205

Alibert, Y., Venturini, J., Helled, R., et al. 2018, Nature Astronomy, 2, 873

Altwegg, K., Balsiger, H., Bar-Nun, A., et al. 2015, Science, 347, 1261952

Ataiee, S., Baruteau, C., Alibert, Y., & Benz, W. 2018, Astronomy & Astrophysics, 615, A110

Ayliffe, B. A., & Bate, M. R. 2009, Monthly Notices of the Royal Astronomical Society, 393, 49

Bai, X.-N. 2015, The Astrophysical Journal, 798, 84

Balbus, S. A., & Hawley, J. F. 1991, The Astrophysical Journal, 376, 214

—. 1998, Reviews of Modern Physics, 70, 1

Barr, A. C., & Canup, R. M. 2008, Icarus, 198, 163

—. 2010, Nature Geoscience, 3, 164

Blaes, O. M., & Balbus, S. A. 1994, The Astrophysical Journal, 421, 163

Blum, J., & Wurm, G. 2008, Annu. Rev. Astron. Astrophys., 46, 21

Brügger, N., Alibert, Y., Ataiee, S., & Benz, W. 2018, Astronomy & Astrophysics, 619, A174

Burrows, A., Marley, M., Hubbard, W. B., et al. 1997, The Astrophysical Journal, 491, 856

Cabrera, J., Jimenez, M. F., Munoz, A. G., & Schneider, J. 2018, arXiv preprint arXiv:1806.10032

Canup, R. M., & Ward, W. R. 2002, The Astronomical Journal, 124, 3404

—. 2006, Nature, 441, 834

—. 2009, Europa, University of Arizona Press in collaboration with Lunar and Planetary Institute, Tucson, 59

Carrera, D., Johansen, A., & Davies, M. B. 2015, Astronomy & Astrophysics, 579, A43

Chambers, J. E. 1999, Monthly Notices of the Royal Astronomical Society, 304, 793

Christensen, U. R., Holzwarth, V., & Reiners, A. 2009, Nature, 457, 167

Cilibrasi, M., Szulágyi, J., Mayer, L., et al. 2018, Monthly Notices of the Royal Astronomical Society, 480, 4355

Connerney, J. 1993, Journal of Geophysical Research: Planets, 98, 18659

Crida, A., & Charnoz, S. 2012, Science, 338, 1196

D'Angelo, G., Henning, T., & Kley, W. 2002, Astronomy & Astrophysics, 385, 647

D'Angelo, G., & Podolak, M. 2015, The Astrophysical Journal, 806, 203

Drażkowska, Joanna, J., & Szulágyi, J. 2018, The Astrophysical Journal, 866, 142

Durham, W., Prieto-Ballesteros, O., Goldsby, D., & Kargel, J. 2010, Space Science Reviews, 153, 273

Dwyer, C., Nimmo, F., Ogihara, M., & Ida, S. 2013, Icarus, 225, 390

Estrada, P. R., Mosqueira, I., Lissauer, J., D'Angelo, G., & Cruikshank, D. 2009, Europa, edited by RT Pappalardo, WB McKinnon, and K. Khurana, University of Arizona Press, Tucson, 27

Fortney, J. J., Demory, B.-O., Désert, J.-M., et al. 2011, The Astrophysical Journal Supplement Series, 197, 9

Fujii, Y. I., Kobayashi, H., Takahashi, S. Z., & Gressel, O. 2017, The Astronomical Journal, 153, 194

Fujii, Y. I., Okuzumi, S., Tanigawa, T., & ichiro Inutsuka, S. 2014, The Astrophysical Journal, 785, 101

Fujita, T., Ohtsuki, K., Tanigawa, T., & Suetsugu, R. 2013, The Astronomical Journal, 146, 140

Fung, J., & Chiang, E. 2016, The Astrophysical Journal, 832, 105

Furuya, K., Aikawa, Y., Nomura, H., Hersant, F., & Wakelam, V. 2013, The Astrophysical Journal, 779, 11

Genda, H., & Ikoma, M. 2008, Icarus, 194, 42

Gressel, O., Nelson, R. P., Turner, N. J., & Ziegler, U. 2013, The Astrophysical Journal, 779, 59

Gundlach, B., & Blum, J. 2015, The Astrophysical Journal, 798, 34

Hayashi, C. 1981, Progress of Theoretical Physics Supplement, 70, 35

Hayashi, C., Nakazawa, K., & Adachi, I. 1977, Publications of the Astronomical Society of Japan, 29, 163

Heller, R., Williams, D., Kipping, D., et al. 2014, Astrobiology, 14, 798

Hirose, S., Krolik, J. H., & Blaes, O. 2009, The Astrophysical Journal, 691, 16

Horner, J., Mousis, O., Alibert, Y., Lunine, J. I., & Blanc, M. 2008, Planetary and Space Science, 56, 1585

Hwang, K.-H., Udalski, A., Bond, I., et al. 2018, The Astronomical Journal, 155, 259

Ida, S., & Guillot, T. 2016, Astronomy & Astrophysics, 596, L3

Ida, S., Guillot, T., & Morbidelli, A. 2016, Astronomy & Astrophysics, 591, A72

Ida, S., & Lin, D. N. C. 2004, The Astrophysical Journal, 604, 388

Iess, L., Rappaport, N. J., Jacobson, R. A., et al. 2010, Science, 327, 1367

Ikoma, M., Guillot, T., Genda, H., Tanigawa, T., & Ida, S. 2006, The Astrophysical Journal, 650, 1150

Johansen, A., & Klahr, H. 2005, The Astrophysical Journal, 634, 1353

Johansen, A., Klahr, H., & Mee, A. J. 2006, Monthly Notices of the Royal Astronomical Society, 370, L71

Kanagawa, K. D., Muto, T., Okuzumi, S., et al. 2018, The Astrophysical Journal, 868, 48

Kanagawa, K. D., Muto, T., Tanaka, H., et al. 2015, The Astrophysical Journal Letters, 806, L15

Keith, S. L., & Wardle, M. 2014, Monthly Notices of the Royal Astronomical Society, 440, 89

Kivelson, M., Khurana, K., Russell, C., et al. 1996, Nature, 384, 537

Kobayashi, H., Ormel, C. W., & Ida, S. 2012, The Astrophysical Journal, 756, 70

Krijt, S., Ormel, C. W., Dominik, C., & Tielens, A. G. 2016, Astronomy & Astrophysics, 586, A20

Kruijer, T. S., Burkhardt, C., Budde, G., & Kleine, T. 2017, Proceedings of the National Academy of Sciences, 201704461

Lainey, V., Arlot, J.-E., Karatekin, Ö., & Van Hoolst, T. 2009, Nature, 459, 957

Lambrechts, M., & Johansen, A. 2012, Astronomy & Astrophysics, 544, A32

Liebig, C., & Wambsganss, J. 2010, Astronomy & Astrophysics, 520, A68

Lissauer, J. J., Hubickyj, O., D'Angelo, G., & Bodenheimer, P. 2009, Icarus, 199, 338

Liu, B., & Ormel, C. W. 2018, Astronomy & Astrophysics

Liu, B., Ormel, C. W., & Lin, D. N. 2017, Astronomy & Astrophysics, 601, A15

Lovelace, R. V. E., Covey, K. R., & Lloyd, J. P. 2011, The Astronomical Journal, 141, 51

Lubow, S. H., Seibert, M., & Artymowicz, P. 1999, The Astrophysical Journal, 526, 1001

Lunine, J. I., & Stevenson, D. J. 1982, Icarus, 52, 14

Machida, M. N., Kokubo, E., Inutsuka, S.-i., & Matsumoto, T. 2008, The Astrophysical Journal, 685, 1220

Miguel, Y., & Ida, S. 2016, Icarus, 266, 1

Mizuno, H. 1980, Progress of Theoretical Physics, 64, 544

Mordasini, C. 2018, Handbook of Exoplanets, 1

Mori, S., Bai, X.-n., & Okuzumi, S. in prep., The Astrophysical Journal

Mosqueira, I., Estrada, P., & Turrini, D. 2010, Space Science Reviews, 153, 431

Mosqueira, I., & Estrada, P. R. 2003a, Icarus, 163, 198

—. 2003b, Icarus, 163, 232

Nakamoto, T., & Nakagawa, Y. 1994, The Astrophysical Journal, 421, 640

Namouni, F. 2010, The Astrophysical Journal Letters, 719, L145

Ogihara, M., & Ida, S. 2012, The Astrophysical Journal, 753, 60

Ogihara, M., & Kobayashi, H. 2013, The Astrophysical Journal, 775, 34

Ogihara, M., Kobayashi, H., Inutsuka, S.-i., & Suzuki, T. K. 2015, Astronomy & Astrophysics, 579, A65

Okuzumi, S., & Hirose, S. 2011, The Astrophysical Journal, 742, 65

Okuzumi, S., Momose, M., iti Sirono, S., Kobayashi, H., & Tanaka, H. 2016, The Astrophysical Journal, 821, 82

Okuzumi, S., Tanaka, H., Kobayashi, H., & Wada, K. 2012, The Astrophysical Journal, 752, 106

Ormel, C., & Cuzzi, J. 2007, Astronomy & Astrophysics, 466, 413

Ormel, C. W. 2017, in Formation, Evolution, and Dynamics of Young Solar Systems (Springer), 197–228

Ormel, C. W., & Liu, B. 2018, Astronomy & Astrophysics

Paardekooper, S.-J., Baruteau, C., & Kley, W. 2011, Monthly Notices of the Royal Astronomical Society, 410, 293

Peale, S., & Lee, M. H. 2002, Science, 298, 593

Peale, S. J., Cassen, P., & Reynolds, R. T. 1979, Science, 203, 892

Perets, H. B., & Murray-Clay, R. A. 2011, The Astrophysical Journal, 733, 56

Ronnet, T., Mousis, O., & Vernazza, P. 2017, The Astrophysical Journal, 845, 92

Ronnet, T., Mousis, O., Vernazza, P., Lunine, J. I., & Crida, A. 2018, arXiv preprint arXiv:1804.02892

Ros, K., & Johansen, A. 2013, Astronomy & Astrophysics, 552, A137

Roth, L., Saur, J., Retherford, K. D., et al. 2014, Science, 343, 171

Rubin, M. E., Desch, S. J., & Neveu, M. 2014, Icarus, 236, 122

Saito, E., & Sirono, S. 2011, The Astrophysical Journal, 728, 20

Sánchez-Lavega, A. 2004, The Astrophysical Journal Letters, 609, L87

Sasaki, T., Stewart, G. R., & Ida, S. 2010, The Astrophysical Journal, 714, 1052

Sato, T., Okuzumi, S., & Ida, S. 2016, Astronomy & Astrophysics, 589, A15

Schoonenberg, D., & Ormel, C. W. 2017, Astronomy & Astrophysics, 602, A21

Schubert, G., Anderson, J., Spohn, T., & McKinnon, W. 2004, Jupiter: The planet, satellites and magnetosphere, 1, 281

Shakura, N. I., & Sunyaev, R. A. 1973, Astronomy & Astrophysics, 24, 337

Shibaike, Y., Okuzumi, S., Sasaki, T., & Ida, S. 2017, The Astrophysical Journal, 846, 10pp

Shibaike, Y., Ormel, C. W., Ida, S., Okuzumi, S., & Sasaki, T. submitted, Nature Astronomy

Shoji, D., & Kurita, K. 2014, Journal of Geophysical Research: Planets, 119, 2457

Sohl, F., Spohn, T., Breuer, D., & Nagel, K. 2002, Icarus, 157, 104

Spalding, C., Batygin, K., & Adams, F. C. 2016, The Astrophysical Journal, 817, 18

Spohn, T., & Breuer, D. 1998, in Planetary Systems: The long view, J. T. T. V. L., 135

Stevenson, D. J. 1984, in NASA Conference Publication, Vol. 2330, NASA Conference Publication, ed. J. T. Bergstralh

Stevenson, D. J., Spohn, T., & Schubert, G. 1983, Icarus, 54, 466

Suetsugu, R., & Ohtsuki, K. 2017, The Astrophysical Journal, 839, 66

Suetsugu, R., Ohtsuki, K., & Fujita, T. 2016, The Astronomical Journal, 151, 140

Szulágyi, J. 2017, The Astrophysical Journal, 842, 103

Szulágyi, J., Cilibrasi, M., & Mayer, L. 2018, The Astrophysical Journal Letters, 868, L13

Szulágyi, J., Masset, F., Lega, E., et al. 2016, Monthly Notices of the Royal Astronomical Society, 460, 2853

Szulágyi, J., Mayer, L., & Quinn, T. 2017, Monthly Notices of the Royal Astronomical Society, 464, 3158

Szulágyi, J., Morbidelli, A., Crida, A., & Masset, F. 2014, The Astrophysical Journal, 782, 65

Takata, T., & Stevenson, D. J. 1996, Icarus, 123, 404

Taki, T., Fujimoto, M., & Ida, S. 2016, Astronomy & Astrophysics, 591, A86

Tanigawa, T., & Ikoma, M. 2007, The Astrophysical Journal, 667, 557

Tanigawa, T., Maruta, A., & Machida, M. N. 2014, The Astrophysical Journal, 784, 109

Tanigawa, T., Ohtsuki, K., & Machida, M. N. 2012, The Astrophysical Journal, 747, 47

Tanigawa, T., & Tanaka, H. 2016, The Astrophysical Journal, 823, 48

Teachey, A., & Kipping, D. M. 2018, Science advances, 4, eaav1784

Teachey, A., Kipping, D. M., & Schmitt, A. R. 2017, The Astronomical Journal, 155, 36

Tsukamoto, Y., Okuzumi, S., & Kataoka, A. 2017, The Astrophysical Journal, 838, 151

Turner, N. J., Lee, M. H., & Sano, T. 2014, The Astrophysical Journal, 783, 14

Venturini, J., & Helled, R. 2017, The Astrophysical Journal, 848, 95

Wada, K., Tanaka, H., Suyama, T., Kimura, H., & Yamamoto, T. 2009, The Astrophysical Journal, 702, 1490

Wakita, S., & Sekiya, M. 2011, Earth, planets and space, 63, 1193

Wang, H.-H., Bu, D., Shang, H., & Gu, P.-G. 2014, The Astrophysical Journal, 790, 32

Ward, W. R., & Canup, R. M. 2010, The Astronomical Journal, 140, 1168

Weidenschilling, S. 1977, Icarus, 44, 172

Whipple, F. 1972, From plasma to planet, ed. A. Elvius (London: Wiley)

Yoder, C. F. 1979, Nature, 279, 767

Yoder, C. F., & Peale, S. J. 1981, Icarus, 47, 1

Youdin, A. N., & Goodman, J. 2005, The Astrophysical Journal, 620, 459

Youdin, A. N., & Lithwick, Y. 2007, Icarus, 192, 588

Zhu, Z., Ju, W., & Stone, J. M. 2016, The Astrophysical Journal, 832, 193

Zhu, Z., Nelson, R. P., Dong, R., Espaillat, C., & Hartmann, L. 2012, The Astrophysical Journal, 755, 6